Solid-State NMR Studies of Alkali Fullerides and Long-Chain Alkanes

By

GIUSEPPE GRASSO

Thesis submitted to the University of Nottingham for the degree of Doctor of Philosophy, November 2003

Table of Contents

Abstract

The main focus of this thesis is the investigation of structure and motion of different materials by applying different solid-state NMR techniques.

In the first section (1) some of the bases of NMR are described both in a Classical (1.1) and Quantum Mechanical (1.2) approach, while the next two sections deal with the experimental part of the work.

In section 2 solid-state NMR studies of CsC_{60} are described and an unambiguous assignment of the ^{13}C NMR spectrum of the polymer phase of CsC_{60}, which is based solely on our experimental data, is presented. In contrast to previous work, the assignment does not rely on the knowledge of the electronic structure of this material and our results support a fully three-dimensional electronic structure as opposed to a quasi one-dimensional one. This is achieved using a two-dimensional ^{13}C MAS NMR correlation experiment, which identifies nuclei coupled via a through-bond scalar interaction, the Refocused INADEQUATE.

In section 3 solid-state NMR experiments performed on polyethylene and long-chain *n*-alkanes corresponding to the formula $C_{246}H_{494}$ are described. Particular attention is given to some specific issues such as chain folding and a detailed study of the saturation-recovery curves (T_1) obtained is carried out for different materials. The model elaborated is able to simulate all the data recorded and the presence of an interphase between the crystalline and the amorphous parts of the samples is proposed.

To help the understanding of the structure and the motion of long-chain *n*-alkanes in section 3 some deuterated samples such as $C_{216}H_{434}$-d_{24} and $C_{12}H_{25}(CH_2)_{192}CHDC_{11}D_{23}$+$C_{162}H_{326}$ ("the mixture") are also studied. Deuterium NMR is widely used and we fit all the experimental line shape of the different samples at different temperatures. Diverse models for the structure and motion of such materials are given, which take into account all the experimental results obtained.

1 Fundamentals

1.1 The Classical Approach

1.1.1 The Bloch Vector Model

The classical description of magnetic resonance has close analogies with the behaviour of the quantum system and the physical picture provided can be of great benefit[1]. Consider the behaviour of a magnetic moment, $\boldsymbol{\mu}$, in the presence of a magnetic field $\mathbf{B_0}$; the former will experience a torque $\boldsymbol{\mu} \times \mathbf{B_0}$. The magnetic moment associated with the nucleus also possesses angular momentum and the equation of motion of $\boldsymbol{\mu}$ may be obtained by equating the rate of change of angular momentum (**P**) with the torque experienced by $\boldsymbol{\mu}$ in the magnetic field,

$$\frac{\mathrm{d}\mathbf{P}}{\mathrm{d}t} = \boldsymbol{\mu} \times \mathbf{B}_0 \qquad \textbf{(1.1)}$$

Usually, nuclear magnetic moments are described in terms of magnetic ratios γ. The value of γ is defined by the equation **(1.2)**:

$$\boldsymbol{\mu} = \gamma \mathbf{P} \qquad \textbf{(1.2)}$$

Combining **(1.1)** and **(1.2)** we obtain:

$$\frac{\mathrm{d}\,\boldsymbol{\mu}}{\mathrm{d}\,t} = \gamma \boldsymbol{\mu} \times \mathbf{B}_0 \qquad \textbf{(1.3)}$$

If the magnetic field is independent of time and directed along the z-axis so that

$\mathbf{B_0} = B_z\mathbf{k}$

Then equation **(1.3)** becomes

$$\frac{\mathrm{d}\mu_x}{dt} = \gamma\mu_y B_z\,;\ \frac{\mathrm{d}\mu_y}{dt} = -\gamma\mu_x B_z\,;\ \frac{\mathrm{d}\mu_z}{dt} = 0$$

The solutions to these are given by

$\mu_x(t) = \mu_x(t)\cos\gamma B_z t + \mu_y(t)\sin\gamma B_z t$

$\mu_y(t) = -\mu_x(t)\sin\gamma B_z t + \mu_y(t)\cos\gamma B_z t$

$\mu_z(t) = \mu_z(0)$

The motion of the magnetic moment described by the above is one of precession. $\boldsymbol{\mu}$ experiences a torque that is perpendicular to both $\boldsymbol{\mu}$ and $\mathbf{B_0}$. The angle between $\boldsymbol{\mu}$ and $\mathbf{B_0}$ does not change and so the tip of the vector $\boldsymbol{\mu}$ undergoes precession about the magnetic field axis and traces out a cone as a function of time. The angular frequency of precession is given by $\omega_L = \gamma B_z$ and we can define $\nu_L = \omega_L/2\pi = \gamma B_z/2\pi$, the Larmor precession frequency that is identical to the photon frequency required to drive transitions between the states of the spin system.

So far, only the behaviour of individual nuclear spins has been considered. However, a macroscopic sample contains an ensemble of many such spins, which will be distributed at random around many precessional cones. If the sample consists of many identical molecules, each with one magnetic nucleus of spin $I = \frac{1}{2}$, the population of the two states is:

$n_\alpha - n_\beta = \Delta n_0 = N\,\Delta U/2kT$ **(1.4)**

where N is the total number of nuclei in the relevant sample, $\Delta U = \gamma \hbar \mathbf{B_0}$ is the energy difference between the states and Δn_0 refers to the equilibrium situation. The total magnetic moment of the sample (**M**) is the resultant of the individual magnetic moments $\boldsymbol{\mu}$. At equilibrium **M** is along the +z direction and has a magnitude:

$M_0 = n_\alpha \mu_{z\alpha} + n_\beta \mu_{z\beta} = \Delta n_0 \mu_{z\alpha} = \frac{1}{2}\gamma \hbar\, \Delta n_0$

since $\mu_{z\beta} = -\mu_{z\alpha}$. Substitution for Δn_0 gives expression:

$$M_0 = \frac{1}{4} N\gamma\hbar\,\Delta U/kT = \frac{1}{4} N(\gamma\hbar)^2 \mathbf{B_0}/kT \qquad \textbf{(1.5)}$$

which is analogous to the Curie expression.

Let us apply radio-frequency (rf) radiation to a sample in the presence of a static field $\mathbf{B_0}$. The important component of the rf radiation is the oscillating B-field, $\mathbf{B_1}(t)$, this is commonly applied perpendicular to $\mathbf{B_0}$,

$\mathbf{B_0} = \mathbf{k}B_z$

$\mathbf{B_1}(t) = \mathbf{i}2\,B_1 \cos\omega_{rf}t$

$\mathbf{B_1}(t)$ is linearly polarized along the x-axis, it may be resolved into two components

$\mathbf{B_a}(t) = B_1(\mathbf{i}\cos\omega_{rf}t + \mathbf{j}\sin\omega_{rf}t)$

$\mathbf{B_c}(t) = B_1(\mathbf{i}\cos\omega_{rf}t - \mathbf{j}\sin\omega_{rf}t)$

Only the field, which rotates in the same direction as the magnetisation, has an appreciable effect. The solution to the torque equation is made possible by a transformation to a co-ordinate system rotating at the transmitter frequency, ω_{rf}, in the same sense as the Larmor precession. In this frame, a time-independent effective field, $\mathbf{B}_{eff}$, can be defined as:

$$\mathbf{B}_{eff} = B_1\mathbf{j} - \frac{\Omega}{\gamma}\mathbf{k} \qquad \textbf{(1.6)}$$

Where Ω is the offset of the Larmor frequency from the transmitter:

$\Omega = \omega_L - \omega_{rf}$

The resonant nature of the NMR phenomenon is made clear from this treatment since only an applied field with ω_{rf} in the vicinity of the Larmor frequency will cause the effective field to tilt appreciably away from the z-axis.

If the new axis system is designated (x',y',z), the application of $\mathbf{B}_1$ has the effect of rotating the sample magnetisation, **M**, about the x'-axis at the angular frequency $\omega_L' = -\gamma\mathbf{B_1}$ (the Larmor frequency in the rotating frame). This is illustrated in Figure 1.

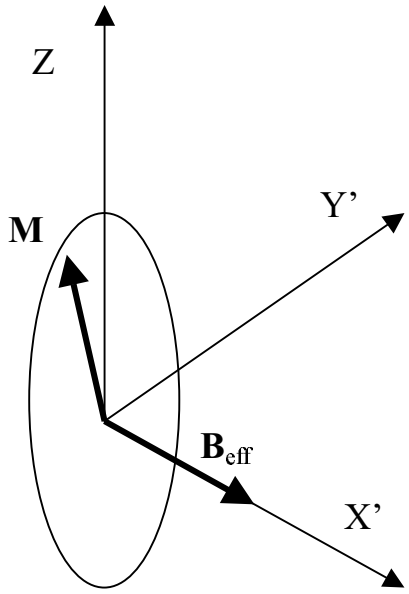

Figure 1: vector representation of the magnetization in the rotating frame.

In a time t_w, **M** rotates through the angle

$\theta = \gamma B_1 t_w$

This analysis indicates how a magnetic resonance experiment may be performed. If an rf pulse of duration t_w and frequency ω_L is applied to the system polarised in a plane perpendicular to the applied static magnetic field, then **M** will be tipped through an angle θ. Once the B_1 field is switched off, the magnetisation precesses about the static field, inducing a voltage in the receiver coil. It is this voltage that is detected as the NMR signal.

1.1.2 The Bloch model of Relaxation

In order to express the return of the transverse magnetisation produced to its equilibrium value, the vector model can be extended in the following fashion. This is based on the observation that, after pulsed excitation, the z-component of magnetisation, M_z, eventually regains its equilibrium value, M_{eq}, and the transverse components, M_x and M_y, decay away to zero. In the Bloch model[2], these two processes are assumed to be first order with different time constants such that (Eq. **(1.7)**):

$$\frac{dM_z}{dt} = \frac{(M_{eq} - M_z)}{T_1};$$

$$\frac{dM_x}{dt} = -\frac{M_x}{T_2};$$

$$\frac{dM_y}{dt} = -\frac{M_y}{T_2};$$

Since M_z arises from the population difference between energy levels, the first process, with time constant T_1, represents the return of these to their equilibrium values. This involves exchange of energy between the spins and their surroundings and is traditionally known as "spin-lattice" or "longitudinal" relaxation. The second process represents a reduction in the bulk transverse magnetisation due to a loss of phase coherence between individual spins. This is known as "spin-spin" or "transverse" relaxation. The way the two time constants are defined means that any process that causes T_1 relaxation must necessarily cause T_2 relaxation also.

1.1.3 Form of the NMR signal

Let the system be in thermal equilibrium initially, then apply a $(\theta)_x$-pulse on resonance, as it was shown at the end of section 1.1.1. The state of the system immediately after the pulse is

$M_z = 0;$

$M_y = M_0 \sin\theta;$

$M_x = M_0 \cos\theta;$

The solutions of the Bloch equations **(1.7)**, subjected to these initial conditions are:

$M_x(t) = M_0 \sin\theta \sin(\omega_0 t) \exp(-t/T_2);$

$M_y(t) = M_0 \sin\theta \cos(\omega_0 t) \exp(-t/T_2)$

This can be expressed as a complex signal M^+:

$M^+(t) = M_x(t) + iM_y(t) = M_0 \sin\theta \exp(i\omega_0 t) \exp(-t/T_2)$

The above equations are given for the laboratory frame but the NMR signal is generally mixed with a reference signal prior to digitisation so that the frequencies actually observed are offsets from this reference, so any deviation from resonance is manifested as a modulation of the FID. If the reference frequency is identical to the transmitter frequency, this is equivalent to detection in the rotating frame. The complex signal in this frame, M^+', has a reduced Larmor precession and is given by:

$M^+'(t) = M_0 \sin\theta \exp(i\Omega t) \exp(-t/T_2)$

1.1.4 The Nuclear Overhauser Effect

The nOe (Nuclear Overhauser Effect) is a change of intensity of an NMR resonance when the transitions of another one are perturbed (usually saturated)[3]. The nOe is then a manifestation of the attempt of the total system to stay at thermal equilibrium; we have forcibly changed the population differences of part of it, so other parts change in compensation. Suppose the normal intensity of a resonance is I_0. Then if the intensity observed while saturating some other relating resonance (and waiting for the new equilibrium to be established) is I, we define the nOe as:

$\eta_i(s) = (I - I_0)/I_0$

This expression is also often multiplied by 100 to make the percentage. Note that, from this definition, the nOe will be positive if the new intensity is greater than the unperturbed intensity and negative if it is less. $\eta_i(s)$ indicates that this is the nOe at nucleus *i* when nucleus *s* is saturated.

1.2 Quantum Mechanical Treatment of NMR

While a vector description of the motion of a macroscopic magnetisation can provide some useful insight, a full explanation of the behaviour of interacting spins requires a quantum mechanical treatment[4]. In addition, the statistical properties of an ensemble of such spins must also be considered in order to account for the bulk nature of the NMR phenomenon. Hence, density matrix theory which incorporates both statistical and quantum mechanical ideas proves a suitable framework in which to work[5]. Before a description of this theory, the solution state NMR Hamiltonian and the quantum mechanical view of angular momentum will be summarized.

1.2.1 Spin Angular Momentum Operators

The Cartesian components of angular momentum are defined by the commutation relations of their associated operators:

$$[j_\alpha, j_\beta] = \mathrm{i}h\, j_\gamma / 2\pi \qquad \textbf{(1.8)}$$

where α, β, γ are x, y, z and cyclic permutations of these. For simplicity, the circumflex is omitted in the symbols representing operators. Many quantum mechanical observables are associated with operators that obey these commutation rules and are treated as angular momenta even though their origins have little to do with the familiar classical quantity. From only the commutation relations of Eq. **(1.8)** and the Hermiticity of operators corresponding to observables, it is possible to derive the eigenvalues and eigenfunctions of angular momentum. These are given by the equations:

$j^2 \,|j,m_j\rangle = (h/2\pi)^2 j(j+1)\,|j,m_j\rangle$ **(1.9)**

with j = 0,1/2,1,….and:

$j_z \,|j,m_j\rangle = (h/2\pi) m_j\,|j,m_j\rangle$ **(1.10)**

with m_j = j, j-1,…..,-j. The eigenfunctions $|j,m_j\rangle$ are a set of spherical harmonics. Only the total magnitude and one of the components, traditionally that parallel to the z-axis, are specified at any given time in order to avoid contradiction of the Uncertainty Principle. Raising and lowering operators are defined as follows:

$j^+ = j_x + \mathrm{i}\, j_y$

$j^- = j_x - \mathrm{i}\, j_y$

These cause the z-component of the angular momentum to increase or decrease by a single unit:

$j^\pm \,|j,m_j\rangle = (h/2\pi)\{j(j+1) - m_j(m_j \pm 1)\}\,|j,m_j \pm 1\rangle$

The definitions given here apply to all quantum mechanical quantities that behave as angular momenta, including nuclear spin. Successive application of the raising or lowering operators establishes that, for spin –1/2 particles, the two states $|1/2,1/2\rangle$ and $|1/2, -1/2\rangle$ form the complete set of spin angular momentum eigenfunctions. For convenience, these are represented as $|\alpha\rangle$ and $|\beta\rangle$ respectively. The properties of the various spin-1/2 operators may be summarized using the Pauli spin matrices. With the states $|\alpha\rangle$ and $|\beta\rangle$ as a basis, these are:

$$I_x = \frac{1}{2}\begin{pmatrix} 0 & 1 \\ 1 & 0 \end{pmatrix},\ I_y = \frac{1}{2i}\begin{pmatrix} 0 & -1 \\ 1 & 0 \end{pmatrix},\ I_z = \frac{1}{2}\begin{pmatrix} -1 & 0 \\ 0 & 1 \end{pmatrix} \quad \textbf{(1.11)}$$

$$I^2 = \frac{3}{4}\begin{pmatrix}1 & 0\\ 0 & 1\end{pmatrix},\ I^+ = \begin{pmatrix}0 & 0\\ 1 & 0\end{pmatrix},\ I^- = \begin{pmatrix}0 & 1\\ 0 & 0\end{pmatrix} \qquad \textbf{(1.12)}$$

In treatments of magnetic resonance, quantities are normally written in terms of these matrices or the corresponding operators and a factor of $\hbar$ is dropped. This procedure has been adopted in the following sections.

In analogy with angular momentum operators that generate rotations or co-ordinate transformations in physical space, the spin operators produce rotations in spin space. The rotation of a wave function, ψ, through an angle φ about the α-axis of such a space can be represented as:

$$\Psi \xrightarrow{R_\alpha(\varphi)} \exp\left(-i\varphi I_\alpha\right)\Psi$$

The corresponding result for an operator, Q, is the unitary transformation:

$$Q \xrightarrow{R_\alpha(\varphi)} \exp\left(-i\varphi I_\alpha\right) Q \exp\left(i\varphi I_\alpha\right)$$

The exponential operators in these expressions are known as propagators and can be obtained explicitly by an expansion:

$$\exp(-\mathrm{i}\varphi I_\alpha) = E - \mathrm{i} I_\alpha \varphi - \frac{1}{2!} I_\alpha^2 \varphi^2 + \frac{\mathrm{i}}{3!} I_\alpha^3 \varphi^3 + \ldots = E\cos\frac{1}{2}\varphi - \mathrm{i} I_\alpha \sin\frac{1}{2}\varphi$$

(1.13)

Where E is the identity operator. The result of co-ordinate transformations in spin space can be established from the matrices of Eq. **(1.11)** or the commutation relations of Eq. **(1.8)**.

1.2.2 The Nuclear spin Hamiltonian operator

The energy of a system is observable, and the corresponding operator H is known as the Hamiltonian operator. It plays an important role in quantum mechanics, as its eigenfunctions describe the stationary states of the system.

The complete Hamiltonian for a molecule contains terms describing the kinetic energy of each particle, the potential energy of interactions between particles, and interactions of the particles with any external electric or magnetic fields. It can be divided approximately into terms representing electronic, vibrational, rotational and nuclear spin contributions to the energy, and the wave function can be written as a product of electronic, vibrational, rotational and nuclear spin functions, each of which is an eigenfunction of its own effective Hamiltonian. The full nuclear spin Hamiltonian contains terms which represent several interactions, including direct and indirect spin coupling, shielding by the surrounding electrons and the interactions with the external static field and the applied radio frequency field. The relevant spin Hamiltonians (expressed in frequency units $\frac{E}{\hbar}$), used to interpret nuclear resonance spectra obtained from solid samples, are:

1. The Zeeman Hamiltonian H_Z

A large static magnetic field $\mathbf{B_0}$ = (0, 0, B_0) defining the z- axis in the LAB frame polarises the magnetization of the sample. The Zeeman Hamiltonian is:

$$H_Z = \sum_i \omega_0^i I_{iz}$$

The sum runs over all nuclei of the sample.

2. The Radio Frequency Hamiltonian H_{rf}

The r.f. field is applied perpendicular to the static field. To be consistent with the classical description we choose it to be parallel to the x-axis.

$$H_{rf} = -2B_1(t)\cos(\omega t)\sum_i \gamma^i I_{ix}$$

H_Z and H_{rf} may be referred to as external Hamiltonians because they depend essentially only on external parameters.

3. The Chemical Shift Hamiltonian H_{CS}

The chemical shift Hamiltonian arises from the modification by the electrons of the local magnetic field at the nucleus and, therefore, depends on the nature of chemical environment of the atom in question[6]. The perturbation of the Zeeman energy levels caused by the electronic contribution to the magnetic field is very small and is normally expressed in ppm. For protons, the normal range of shifts is about 10 ppm. For molecules executing rapid and random rotation in liquids, this local magnetic field **B'**, proportional to the external field $\mathbf{B_0}$, is written

$\mathbf{B'} = -\sigma\mathbf{B_0}$

where σ is the chemical shielding parameter.

In solids, it may be necessary to write this

$\mathbf{B'} = -\boldsymbol{\sigma}\cdot\mathbf{B_0}$,

where $\boldsymbol{\sigma}$ is now a second rank tensor. That is, the local chemical shift field may differ according to the direction of $\mathbf{B_0}$. If we take $\mathbf{B_0}$ to be in the z-direction, and neglect terms including I_x and I_y since they do not commute with the Zeeman Hamiltonian (secular approximation), we obtain

$$H_{CS} = -\sum_i \gamma^i \boldsymbol{\sigma}_{izz} I_{iz} \mathbf{B} \qquad \textbf{(1.14)}$$

for the chemical shift Hamiltonian; the subscript *i* refers to a particular nucleus. If the symmetric part of the tensor $\boldsymbol{\sigma}_i$ has principal values σ_{i1}, σ_{i2} and σ_{i3} along its principal axes and if θ_{i1}, θ_{i2} and θ_{i3} are the three angles made between each of these axes and the direction of $\mathbf{B_0}$, then

$\boldsymbol{\sigma}_{izz} = \sigma_{i1} \cos^2\theta_{i1} + \sigma_{i2} \cos^2\theta_{i2} + \sigma_{i3} \cos^2\theta_{i3}$. **(1.15)**

Now for rapid and random rotation, each angle in Eq. **(1.15)** varies randomly, so the time average of $\boldsymbol{\sigma}_{izz}$ is given by

$\boldsymbol{\sigma}_{izz} = (1/3)(\sigma_{i1} + \sigma_{i2} + \sigma_{i3}) = (1/3)\,\mathrm{Tr}\,\boldsymbol{\sigma}_i = \boldsymbol{\sigma}_i$, **(1.16)**

since $\overline{\cos^2\theta} = \frac{1}{3}$ and we have an isotropic chemical shielding parameter.

In a solid sample, however, differing nuclear sites will have, in general, different values for the angles appearing in Eq. **(1.15)**, so there will be a distribution of local fields and hence, a broadened line. If, however, the solid sample is rotated at an angular frequency ω_r about an axis making an angle β with respect to the magnetic field $\mathbf{B_0}$ and angles χ_{i1}, χ_{i2} and χ_{i3} with respect to the principal axes of the sample we have

$\cos\theta_{ip} = \cos\beta\cos\chi_{ip} + \sin\beta\sin\chi_{ip}\cos(\omega_r t + \psi_{ip})$ **(1.17)**

for the πth principal axis; ψ_{ip} is the initial azimuthal angle.

Using Eqs. **(1.15)** and **(1.17)**, we obtain

$$\overline{\sigma_{izz}} = \frac{1}{2}(\sin^2\beta)(\sigma_{i1} + \sigma_{i2} + \sigma_{i3}) + \frac{1}{2}(3\cos^2\beta - 1)\sum_p \sigma_{ip}\cos^2\chi_{ip}. \quad \textbf{(1.18)}$$

If $\beta = \beta_M$, the magic angle spinning (MAS) described in a next paragraph, then Eq. **(1.18)** reduces to Eq. **(1.16)**, and the MAS solid case reduces to the liquid case.

4. The Dipolar Hamiltonian H_D

The physical origins of the line broadening due to the dipole-dipole interaction is a local field at the site of the nucleus due to each of the neighbouring nuclei, which will cause the Zeeman energy levels to shift slightly, corresponding to a slight shift in NMR frequency. This local field will vary from point to point

around the sample, as more or fewer neighbouring nuclei have spin up or spin down. This effect can be treated in a formal theoretical fashion by using time-independent perturbation theory, in which the dipole-dipole Hamiltonian shifts the Zeeman levels of the nuclear spin in the external magnetic field.

We have, for the dipolar Hamiltonian for two nuclei, the expression:

$$H_D = \sum_{i<j} (\hbar/2)\gamma_i\gamma_j r_{ij}^{-3}\left(3\cos^2\theta_{ij} - 1\right)\left(I_i \cdot I_j - 3I_{iz}I_{jz}\right) \quad \textbf{(1.19)}$$

In an isotropic liquid, $\cos^2\theta_{ij}$ takes on its random time average value 1/3, so H_D averages to zero due to rapid and random molecular rotation, with the result that the dipolar broadening of the NMR line vanishes.

Squaring Eq. **(1.17)** and taking an average over time leads to (See Figure 2, section 1.2.4):

$$\overline{\cos^2\theta_{ij}} = \frac{1}{6}(3\cos^2\beta - 1)(3\cos^2\chi_{ij} - 1) + \frac{1}{3} \quad \textbf{(1.20)}$$

Combining this with Eq. **(1.19)** leads to the following expression for the time-averaged value of the truncated dipolar Hamiltonian:

$$\overline{H}_D = \frac{\hbar}{4}\left(3\cos^2\beta - 1\right)\sum_{i<j}\gamma_i\gamma_j r_{ij}^{-3}\left(3\cos^2\chi_{ij} - 1\right)\left(I_i \cdot I_j - 3I_{iz}I_{jz}\right) \quad \textbf{(1.21)}$$

It is clear that by choosing β so that $3\cos^2\beta - 1 = 0$, we have $\overline{H}_D = 0$, so the dipolar broadening vanishes. That is, if one rotates a solid sample about an axis making an angle β = 54.7 degrees, as explained in section 1.2.4, then the dipolar broadening of the NMR line disappears and one obtains the same resolution as for the liquid samples.

5. The Scalar or J Hamiltonian H_J

An electron with non-zero density at the sites of two nuclei can interact with both through the Fermi contact hyperfine interaction, and thus provide an

intermediary way through which the nuclei can interact with one another; this interaction is usually called spin-spin coupling, or J coupling. The form of the interaction is written

$$H_J = 2\pi \sum_{i<j} I_i \mathbf{J}_{ij} I_j$$

where the sum is over all pairs of nuclei i and j; the interaction tensor $\boldsymbol{J_{ij}}$ is usually expressed in Hertz.

6. The Electric Quadrupole Hamiltonian H_Q

If the nuclear spin is greater than ½, the electric quadrupole moment of the nucleus interacts strongly with the electric field gradients generated by the surrounding electron clouds. In this case the total Hamiltonian takes the form of the sum of two terms, the Zeeman term and the quadrupolar term:

$$\hbar H(^2H) = \hbar H_Z + \hbar H_Q$$

The deuterium quadrupolar Hamiltonian is:

$$H_Q = \frac{eQ}{4}\left[V_{zz}\left(3I_z^2 - I^2\right) + \left(V_{xx} - V_{yy}\right)\left(I_x^2 - I_y^2\right)\right] \quad \textbf{(1.22)}$$

Where Q is the quadrupolar frequency. Only two parameters are necessary to characterize the gradients of the potential: the field gradient, eq, and the asymmetry parameter, η, defined as:

eq = V_{zz}

$$\eta = \frac{\left|V_{xx} - V_{yy}\right|}{V_{zz}}$$

The asymmetry parameter measures the departure from cylindrical symmetry of the nuclear charge distribution. For axial symmetry ($V_{xx} = V_{yy}$)

$$H_Q = \frac{e^2 Qq}{4}\left[3I_z^2 - I^2\right]$$

and the coupling energies are

$$E(^2H) = \left\langle H_Q \right\rangle = \frac{e^2 qQ}{4}\left[3m^2 - 2\right]$$

where m is the eigenvalues of I_z, I (I+ 1) = 2 is the eigenvalues of I^2, and e^2qQ = $\chi\eta$ is called the quadrupole coupling constant.

1.2.3 *Kνiγ ηt Sηift*

NMR can detect motional processes if they change the nuclear spin Hamiltonian. The nature of these motional effects depends on the type of motion and their timescale. Motion on the spectral timescale causes the NMR line shapes to change. An interesting example of rapid asymmetric exchange is encountered in the NMR of metals where nuclear spins are coupled to unpaired conduction electrons causing the so-called Knight shift. This is due to the hyperfine coupling of the nucleus to the conduction electrons, which are polarized by the magnetic field. For electrons, the Zeeman splitting is three orders of magnitude larger than for nuclei and the Boltzmann population differential of the energy level in the magnetic field leads to an asymmetric two-sites exchange case for a nucleus coupled to an electron. Very often electrons have a very short T_1 and so the NMR spectrum of a coupled nucleus collapses to a single peak. The position of the peak depends on the relative populations of the electronic states and is therefore shifted, since these states are not equally populated: this is called Knight shift and is widely used to probe the electronic structure of metals.

Furthermore, the Knight shift provides a very convenient way to predict spin-lattice relaxation times by using the so-called Korringa equation[7]

$$T_1 K^2 = \beta \frac{\hbar}{4\pi k T} \frac{\gamma_e^2}{\gamma_n^2}$$

Where T_1 is the nuclear spin-lattice relaxation time, ***K*** the Knight shift, γ_e (γ_n) >0 is the electronic (^{13}C-nuclear) gyromagnetic ratio and T the temperature. A deviation of β from unity is a sign of the importance of electron-electron interaction (electronic correlation) and for ^{13}C nucleus the Korringa constant

$S = \left(\frac{\gamma_e^2}{\gamma_n^2}\right)^2 \left(\frac{\hbar}{4\pi k}\right)$ is 4.165×10^{-6} (s K).

1.2.4 *Magic-angle rotation and spinning sidebands*

As shown in a previous paragraph, isolated molecules in definite rotational and vibrational states (as a molecular beam) and molecules in solids have complex spin Hamiltonians. For normal fluids, all terms in the spin Hamiltonian which depend on the relative orientations of the molecule and the applied field average to zero. The spin Hamiltonian for a solid contains orientation-dependent terms, and, in addition, includes interactions between molecules[8]. The terms in the Hamiltonians that cause NMR line broadening for solids involve the geometric factor ($3\cos^2 q$ - 1). It has already been said that rapid isotropic molecular tumbling, such as occurs in non-viscous solutions, averages this geometric factor to zero, thus explaining the very narrow NMR lines observed for such solutions. Therefore it is important to ask if an experiment that simulates such motion can be devised for solids.

Consider then, coherent rotation of a solid sample about an axis at angle β to $\mathbf{B_0}$ (see Figure 2).

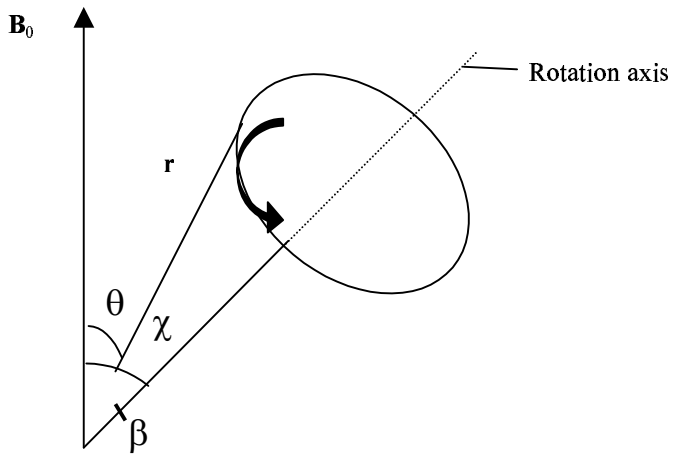

Figure 2: Rotation of the sample at an angle β

The average of $(3\cos^2 q\text{-}1)$ about the conical path indicated for the internuclear vector, **r**, is[9]:

$$\langle 3\cos^2 q\text{-}1\rangle = \frac{1}{2}(3\cos^2\beta\text{-}1)(3\cos^2 \boldsymbol{c}\text{-}1)$$

The parameter $\boldsymbol{c}$ is fixed for a rigid solid, though (like q) it takes all possible values if the material is a powder. The term $\frac{1}{2}(3\cos^2\beta\text{-}1)$ therefore acts as a scaling factor on a dipolar powder pattern. Fortunately the angle β is under the control of the experimentalist. If β = 0 (i.e. rotation about $\mathbf{B}_0$), $\frac{1}{2}(3\cos^2\beta\text{-}1)$ = 1, so there is not net effect on the spectrum. The case of most interest is that when β= 54.7°, since the $\cos\beta = 1/\sqrt{3}$ and $\frac{1}{2}(3\cos^2\beta\text{-}1) = 0$, so that $\langle 3\cos^2\theta\text{-}1\rangle$ = 0 for all orientations (i.e. all values of χ). Thus, just as for isotropic tumbling, the dipolar interaction is averaged to zero, and so dipolar

broadening is eliminated, giving much higher resolution. This situation is referred to as magic-angle spinning (MAS) and 54.7^{o} is called the magic angle. If the spinning frequency ω_R is much larger than the spread in Larmor frequencies caused by chemical-shift anisotropy (CSA) (see the next paragraph), the spectra contain only peaks at the isotropic shift frequencies of the different chemical sites. The resolution and sensitivity then approach that of NMR in isotropic liquids. However, if the spinning speed must be moderated, for example, for mechanical reasons, spinning sidebands appear in the spectrum[10]. These spinning sidebands are due to the modulation of the Larmor frequency as the sample rotates, according to the chemical-shift anisotropy.

Spinning sidebands present both problems and opportunities[11]. They produce degradation in sensitivity because intensity is borrowed from the peaks at the isotropic shifts. They also crowd the spectrum and complicate the assignments. Nevertheless they do contain valuable information as to the shielding anisotropies of the individual sites. In a powder spectrum, their amplitude may be analysed to obtain the principal values of the shielding tensors[12,13], as it is mentioned in the next paragraph 1.2.5.

1.2.5 Sideband Intensities

In the last paragraph we considered the time average part of the perturbing Hamiltonians, and showed how MAS can greatly reduce the line widths for solid samples due to those interactions. We now explore how the system develops as a function of time.

We begin by writing the CSA interaction (See Eq. **1.14**) as a function of time arising because of sample rotation:

$$H_{CS} = \sum_i \sum_{p=1}^{3} I_{iz} B \sigma_{ip} \left[\cos^2 \beta \cos^2 \chi_{ip} + 2 \cos\beta \sin\beta \cos\chi_{ip} \right.$$
$$\left. \sin\chi_{ip} \cos\left(\omega_r t + \psi_{ip}\right) + \sin^2 \beta \sin^2 \chi_{ip} \cos^2\left(\omega_r t + \psi_{ip}\right) \right]$$

where we used Eqs. **(1.14)** and **(1.17)**.

Notice that the interaction contains terms that are periodic with frequency $f_r = \omega_r/2\pi$. It can be shown that this time-dependence gives rise in the FID to a series of echoes separated by a time interval $2\pi/\omega_r = f_r^{-1}$. When the FID is Fourier transformed to obtain the spectrum, these echoes give rise to spinning sidebands separated from the central isotropic spectral line at frequency intervals equal to the spinning frequency f_r.

It has been shown that the sideband intensities are related to the principal values of the CSA tensor[14].

1.3 Deuterium NMR in Solids

As mentioned before (section 1.2.2), for nuclei with spin I = 1 such as ^{2}H in an applied magnetic field, the NMR spectra are dominated by the quadrupole interaction of the I = 1 spin with the electric field gradient tensor at the deuteron site. For aliphatic deuterons the field gradient is found to be approximately axially symmetric about the C-D bond direction. ^{2}H NMR thus monitors the directions of the C-D bonds in the sample. The general form of the Hamiltonian is just the sum of the Zeeman and the quadrupolar terms. This comes from the fact that although the magnitude of the ^{2}H quadrupolar moment is small (2.8 x 10^{-27}cm^2) compared with other quadrupolar nuclei, the quadrupolar energy term dominates in the solid state, and the other contributions can be neglected in the ^{2}H spin Hamiltonian (in liquids this is not the case since isotropic reorientation causes $\hat{H}_Q$ to vanish).

A ^{2}H nucleus, due to its nuclear spin I = 1, has three energy states denoted by m = -1, 0, +1. In an external magnetic field in the absence of perturbations the allowed transitions between the Zeeman levels E_{m+1}, E_{m0}, E_{m-1} lead to degenerate frequencies $\hbar\omega_+ = \hbar\omega_-$. The quadrupolar term $\hbar\hat{H}_Q$ is given by equation **(1.22)**, which becomes, in the presence of a large external magnetic field[15],

$$H_Q = \frac{\chi h}{8}\left[\left(3\cos^2\theta - 1\right) + \eta \sin^2\theta \cos 2\phi\right]$$

where θ and ϕ are the polar and azimuthal angles relating the principal axis system of the electric field gradient to the external field. For axial symmetry (η = 0), the total energies are described by:

$$E_m = -\gamma\hbar H_0 m + \frac{\chi h}{8}\left(3\cos^2\theta - 1\right)\left[3m^2 - 2\right] \quad \textbf{(1.23)}$$

The effect of the anisotropic quadrupolar interaction is to remove the degeneracy of the Zeeman levels in the solid state. The two allowed transitions result in a pair of frequencies for each chemically inequivalent deuteron and the separation of the resonance frequencies depends on the angle between the external magnetic field and the z axis of the electric field gradient tensor. From Eq. **(1.23)**,

$$\Delta\upsilon_q = 3\chi(3\cos^2\theta - 1)/4$$

Single crystal studies of deuterated molecules have been used to determine quadrupolar-coupling constants and relate them to molecular structure[16]. However the dynamic information obtained from single crystals is limited, and therefore the study of ^{2}H NMR powder patterns of polycrystalline and amorphous solids has been more widely used.

1.3.1 Static line shape

A ^{2}H NMR spectrum of a single crystal will show two discrete resonances where the separation in frequency is related to the angle between the principal axis of the quadrupolar tensor and the laboratory frame. In a polycrystalline or amorphous solid, a random distribution of orientation of crystallites occurs where each orientation has equal probability. For deuterium in solids one can describe the distribution by an equation relating the angular-dependent frequency to principal axis systems of the quadrupolar interaction and the laboratory frame[17]:

$$\omega_{zz} = \omega_{11}\cos^2\alpha\sin^2\beta + \omega_{22}\sin^2\alpha\sin^2\beta + \omega_{33}\cos^2\beta \qquad \textbf{(1.24)}$$

For axial symmetry Eq. **(1.24)** becomes

$$\omega_{zz} = (\omega_{\parallel} - \omega_{\perp})\cos^2\beta + \omega_{\perp}$$

β is the angle between the z axis of the laboratory frame and the z axis of the quadrupolar tensor. $\omega_{\perp}$ is the NMR frequency of those crystallites where the C-D bond axis (and the z-axis of the electric field gradient) is perpendicular to the external magnetic field. Similarly, $\omega_{\parallel}$ corresponds to the frequency where the C-D bond is parallel to the external field.

In a polycrystalline sample the resonance line shape will be the sum of all the discrete lines and will account for all possible orientations. In order to determine the line shape it is necessary to calculate the intensity of the resonance lines at each orientation.

It is very difficult to derive the NMR signal analytically so it is common practice to calculate it numerically. The numerical simulation must incorporate a "powder average" over all possible molecular orientations. Since the computation of the NMR signal for each orientation is often time-consuming, it is highly desirable that a reasonable numerical approximation to a full powder average be obtained using a minimum number of orientational samples[18]. The orientational average of a function f corresponds to the integral:

$$\overline{f} = N^{(3)} \int_{V^{(3)}} f(\Omega)\mathrm{d}\Omega \ ,$$

where the volume of integration $V^{(3)}$ represents the ranges of the three Euler angles,

$V^{(3)} = \{0 \le \alpha < 2\pi,\ 0 \le \beta \le \pi,\ 0 \le \gamma < 2\pi\}$

$\mathrm{d}\Omega = \sin\beta\, \mathrm{d}\alpha\, \mathrm{d}\beta\, \mathrm{d}\gamma,$

and the normalization constant is

$N^{(3)} = (8\pi^2)^{-1}$.

In numerical calculations, this integral is approximated by summing the function over a set of N^S different orientations and weights $\boldsymbol{S} = \{\omega_j^S, \Omega_j^S\}$,

$$\overline{f}^S = \sum_{j=1}^{N^S} \omega_j^S f(\Omega_j^S),$$

where the weights are normalized so that their sum equals unity. $\overline{\boldsymbol{f}}^S$ is the estimate of the powder average $\overline{\boldsymbol{f}}$, using the sampling scheme $\boldsymbol{S}$.

In this thesis the ZCW method has been used to simulate the ^{2}H static spectra as it is explained in Ref. 18.

1.3.2 Motional Averaging of the ^{2}H Powder Line shape

In the previous paragraph it was explained how to generate static ^{2}H spectra in solids where the molecular motion is neglected. This sort of approximation rarely occurs in real samples where molecules are undergoing reorientation on a timescale of the order of the quadrupole interaction or faster, so that the observed frequencies will be averaged and the resulting line shape can be analysed to determine the type and the rate of motion[19].

A particularly simple situation arises if the motion is rapid on a timescale defined by the inverse width of the spectrum in absence of motion δ^{-1}. In this rapid exchange limit, which in ^{2}H NMR is reached for correlation times $\tau_c < 10^{-7}$ s, the motion leads to a partially average quadrupole coupling and valuable information about the type of motion can directly be inferred from analysis of the resulting line shapes. The NMR frequency is given by:

$$\omega = \omega_0 \pm \frac{\bar{\chi}}{2}\left(3\cos^2\vartheta - 1 - \bar{\eta}\sin^2\vartheta\cos 2\phi\right) = \omega_0 \pm \overline{\omega_Q} \quad \textbf{(1.25)}$$

where $\bar{\chi}$ and $\bar{\eta}$ are respectively the quadrupolar coupling constant and the asymmetry parameter of the averaged field gradient tensor $\overline{FGT}$ and the polar and azimuthal angles, respectively ϑ and ϕ, specify the orientation of B_0 with respect to the principal axes system of $\overline{FGT}$. It is important to realize that $\bar{\eta}$ may differ substantially from 0 even if $\eta = 0$.

1.4 The Density Matrix

In order to define the density operator ρ of the entire quantum mechanical system and to derive its equation of motion, we start with the time-dependent Schrödinger equation for the evolution of a state function $|\psi(t)\rangle$,

$$\frac{d}{dt}\left|\Psi(t)\right\rangle = -iH(t)\left|\Psi(t)\right\rangle \quad \textbf{(1.26)}$$

H(t) is the Hamiltonian or total energy operator of the system, which may itself be time-dependent.

We may expand the state function ψ(t) in terms of a complete orthonormal base $\{|i\rangle, i = 1,2,...n\}$

$$\left|\Psi(t)\right\rangle = \sum_{i=1}^{n} c_i(t)\left|i\right\rangle$$

where the time-dependence of $|\Psi(t)\rangle$ is expressed by the time-dependent coefficients $c_i(t)$ and n is the dimension of the vector space of all admissible state functions, called Hilbert space.

The expectation value of an observable corresponding to an operator Q, is given by:

$$\langle Q\rangle = \sum_{i,j}\left\langle i\right|Q\left|j\right\rangle c_i^*(t)c_j(t)$$

In an idealised pure state, all spin systems of the ensemble are in the same state and can be described by the same normalized state function $|\psi(t)\rangle$ with $\langle\psi(t)|\psi(t)\rangle = 1$. The corresponding density operator ρ is defined by the product of the ket $|\psi(t)\rangle$ and the bra $\langle\psi(t)|$,

$$\rho(t) = \left|\psi(t)\right\rangle\left\langle\psi(t)\right| = \sum_i\sum_j c_i(t)c_j^*(t)\left|i\right\rangle\left\langle j\right| \quad \textbf{(1.27)}$$

Since the calculation of any observable for this system always entails the use of the same products of the coefficients, c_i, it is convenient to write them as a matrix called the density matrix. This can be thought of as representation in the basis $|i\rangle$ of the density operator defined as in Eq. **(1.27)**.

The situation is different for an ensemble in a mixed state, e.g. for an ensemble in thermal equilibrium. Here we can only indicate probabilities p_k that a spin system of the ensemble is one of several possible states $|\psi_k(t)\rangle$. Therefore, the equation for the expectation value of the observable must be modified to take account of the weighting, p_k, of pure state, ψ_k, in the mixture:

$$\langle Q\rangle = \sum_{i,j,k} p_k \langle i|Q|j\rangle c_{ik}^*(t) c_{jk}(t)$$

A statistical description of such a mixed state is a necessity and it is just such a description that the density operator is introduced to provide. Eq. **(1.27)** becomes:

$$\rho(t) = \sum_{i,j,k} p_k c_{ik}(t) c_{jk}(t) |i\rangle\langle j| = \sum_i \sum_j \overline{c_i(t) c_j^*(t)} |i\rangle\langle j|$$

which represents an ensemble average of the pure state density operator over the possible states $\psi_k(t)$, where $\sum_k p_k = 1$, and the bar denotes the ensemble average.

It follows that the expectation value of any observable is given by:

$$\langle Q\rangle = \mathrm{Tr}\{Q\ \rho(t)\} \qquad \textbf{(1.28)}$$

so that the density operator can be seen to contain all the physically significant information about the system, as the expectation value is found by evaluating the trace of the product of the observable operator and the density operator. The trace can be calculated from the product of the matrix representations of

Q and $\rho(t)$ in an arbitrary base $\{|r\rangle\}$ or via an expansion of the two operators Q and $\rho(t)$ in terms of orthogonal base operators.

The above discussion leads to a number of properties of the density operator and to its physical interpretation. Firstly, the condition that the expectation value of an observable must be real and the form of Eq. **(1.28)** require the density matrix to be Hermitian. More importantly, the probability of finding the system in a particular basis state $|i\rangle$ is given by the diagonal element:

$$\rho_{ii} = \sum_k p_k |c_{ik}|^2$$

In the eigenbase of the Zeeman Hamiltonian, the diagonal elements represents the populations in the states $|\alpha\rangle$ and $|\beta\rangle$. An off-diagonal element of the density matrix, however, indicates some coherent superposition of the relevant basis functions. For a mixed state, this implies that the phases of the wavefunctions, $\psi_k(t)$, are no longer completely random. The element ρ_{ij} can be associated with the transition between states $|i\rangle$ and $|j\rangle$. Where the transition satisfies the relevant selection rule, it is the oscillation of these elements at frequencies given by the difference in energies of the states i and j which are observed in NMR spectroscopy. In general, if each eigenstate of the nuclear spin Hamiltonian has an associated magnetic quantum number, M_i, each coherent superposition (or, simply, "coherence") can be described in terms of a coherence order:

$P_{ij} = M_i - M_j$

The time evolution of the density operator under the Hamiltonian $\hat{H}(t)$ is given by the Liouville-von Neumann equation:

$$\frac{d\rho(t)}{dt} = i[\rho(t), H(t)]$$

For a time-independent Hamiltonian the solution to this equation is:

$\rho(t)$ = exp(-i H t)ρ(0)exp(i H t) **(1.29)**

Density matrix calculations usually involve diagonalizing the matrix form of the Hamiltonian so that the propagators in Eq. **(1.13)** can be easily found. The solution of the Liouville-von Neumann equation for a time-dependent Hamiltonian is normally achieved by the application of suitable coordinate transformations that removes this dependence within a series of finite time segments. The evolution of the density operator can be then expressed in terms of a sequence of propagators associated with the time-independent Hamiltonians, H_1, H_2:

ρ (t_1+t_2) = exp(-i H_2 t_2)exp(-i H_1 t_1) ρ (0)exp(i H_1 t_1)exp(i H_2 t_2)

with the propagators exp{-i H_k τ_k}. This equation applies to any sequence of intervals τ_k in which time-independent average Hamiltonians $\overline{H}_k$ can be defined.

The density operator in thermal equilibrium at temperature T is given by

$$\rho_0 = \frac{1}{Z}\exp\{-H\hbar / kT\}$$

where

Z = tr{exp{- H ħ /kT}}

is the partition function of the system. By evaluating ρ_0 in the eigenbase $\{|r\rangle\}$ of the Hamiltonian, one easily verifies that probability distribution of the eigenstates $|r\rangle$, $P_r = \rho_{rr}$ correctly describes a Boltzmann distribution

$P_r = \frac{1}{Z}\exp\{-E_r\hbar /kT\}$.

1.4.1 Product of Cartesian spin operators

Numerous choices are possible for the expansion of the density operator in terms of a complete set of orthogonal base operators. An arbitrary density operator can be expanded in terms of a set of products of operators corresponding to the Cartesian components of angular momentum, I_{ix}, I_{iy} and I_{iz} which obey the usual cyclic commutation rules of Eq. **1.8**. A useful set of base operators $\{B_s\}$ that retains the clearest physical insight into the spin engineering and which employs relatively simple algebra is then:

$$B_s = 2^{(q-1)} \prod_{k=1}^{n} (I_{kv})^{a_{sk}}$$

Here n is the total number of spins in the spin system under consideration, k is an index for the spin, and ν represents the x, y or z-axis. We simply multiply the spin operators together q at a time ($0 \leq q \leq n$). The exponent a_{sk} is simply a device to define the spins involved in a given product operator; it is unity for the q spins that are involved in the product operator, but zero for the remaining n-q spins. Thus for an *IS* system where n = 2, we consider q = 0,1 and 2. For q = 0, the operator is $\frac{1}{2}E$ where E is the unit operator. For q=1 we have the single-spin operators

$I_x\ I_y\ I_z\ S_x\ S_y\ S_z$

While for q =2 there are nine two-spin operators:

$2I_xS_x\ 2I_xS_y\ 2I_xS_z$

$2I_yS_x\ 2I_yS_y\ 2I_yS_z$

$2I_zS_x\ 2I_zS_y\ 2I_zS_z$

For a three-spin system there will be terms of the form: $4I_xS_xR_x$.

A description of the physical interpretation of each of the operators is as follows. The operators I_{iz} is the equilibrium condition for spin i representing equal population differences across all its transitions. The terms I_{ix} and I_{iy} describe the transverse components of magnetisation of spin *i* which are observable as the expected absorptive and dispersive parts of the in-phase multiplet. The operator $2I_{ix}I_{jz}$ represents anti-phase coherence of spin *i* with respect to the scalar coupling with spin *j*. Because this evolves into in-phase transverse magnetization under the free precession Hamiltonian, it is observable as a multiplet on spin i in which the components separated by the coupling constant J_{ij} have opposing signs. Terms such as $2I_{ix}I_{jx}$ describe a mixture of double- and zero-quantum coherence which cannot be observed directly. Finally, the term $2I_{iz}I_{jz}$ represents a non equilibrium population distribution with no net coherence.

1.4.2 Evolution of Product Operators and Coherence Transfer

The effects of free precession and pulses can be described in terms of a sequence of transformations of the type:

$$\exp(-i\varphi B_\alpha)\, B_\beta \exp(i\varphi B_\alpha) = B_\beta \cos\varphi + B_\gamma \sin\varphi$$

which correspond to rotations in operator spaces (B_α,B_β,B_γ). The form of φ and the operators, which are linked by such a rotation, are derived from the Hamiltonian under consideration and the commutation rules of the product operators themselves.

The evolution of a weakly coupled spin system under the effects of pulses and chemical shifts precession can be described by a series of rotations in the operator space (I_x, I_y, I_z). For example, the effect of an on-resonance pulse

along the x-axis of flip angle β on equilibrium spin *i* magnetisation can be written as:

$$I_{iz} \xrightarrow{\beta I_{ix}} I_{iz}\cos\beta - I_{iy}\sin\beta$$

Similarly, evolution under the *i*-spin chemical shift can be expressed as:

$$I_{ix} \xrightarrow{\Omega_i t I_{iz}} I_{ix}\cos\Omega_i t - I_{iy}\sin\Omega_i t$$

A pulse or evolution under chemical shift always conserves the number of spin operators in the expansion of the density matrix. This restriction forms the basis of a set of coherence transfer selection rules which determine the type of transfer which can be effected by a single non-selective pulse in a weakly coupled system. Scalar coupling terms, on the other hand, produce rotations within operator subspaces of the form (I_{ix}, $2I_{iy}I_{jz}$, $2I_{iz}I_{jz}$). For example, coupling between spins *i* and *j* causes anti-phase coherence to evolve from in-phase spin *i* transverse magnetisation:

$$I_{ix} \xrightarrow{\pi J_{ij} t 2I_{iz}I_{jz}} I_{ix}\cos\pi \mathrm{J}_{ij} t + 2I_{iy}I_{jz}\sin\pi \mathrm{J}_{ij} t$$

In normal circumstances, a period of evolution under such a Hamiltonian is always necessary if coherence transfer between coupled spins or into multiple-quantum transitions is to occur. The anti-phase coherence of spin i can be transferred into corresponding transitions on spin *j* by a π/2 rad pulse:

$$2I_{iy}I_{jz} \xrightarrow{(\pi/2)(I_{ix}+I_{jx})} -2I_{iz}I_{jy}$$

Therefore, the transfer of coherence between a pair of weakly coupled spins can only be observed if the scalar coupling between them is resolved.

1.5 Two-Dimensional NMR Spectroscopy

One may distinguish two general classes of 2D-NMR spectra[20]:

(a) Resolved spectra, which spread the peaks of a single spectrum into two dimensions characterised by different NMR parameters; and (b) Correlated spectra, which correlate pairs of spins related by virtue of some interaction or dynamic process and it is this kind of 2D experiment which will be used in this work.

Two-dimensional time-domain NMR spectroscopy involves two independent evolution periods. The first of these, usually denoted as t_1, is an incremental delay inserted in the pulse sequence whilst the second, called t_2, is the normal detection period. A series of free induction decays, recorded during t_2, is obtained for increasing values of t_1. Observation of the signal only occurs during t_2, the t_1 evolution being monitored indirectly through the modulation of phase or amplitude, which is imposed on the magnetisation present at the beginning of the detection period. Two-dimensional Fourier transformation of the recorded data matrix, $S(t_1, t_2)$, results in a spectrum, $S(\omega_1, \omega_2)$, which is a function of two frequency coordinates.

It is customary to refer to four time periods in the description of correlation experiments. These are as follows:

1. The preparation period. A suitable sequence of pulses is used to create the coherence that will evolve in t_1. For many experiments, transverse magnetisation evolves during t_1 and a single non-selective pulse is sufficient. However, more complicated preparation sequences that, for example, excite multiple-quantum coherence or transfer proton polarization to low frequency heteronuclei are also used.

2. The evolution period. The rate at which the delay t_1 is incremented determines the spectral width in the ω_1 dimension just as the sampling rate during t_2 determines the spectral width in ω_2. During t_1, each coherence detected indirectly in t_1 may be associated with ordinarily unobservable multiple-quantum transitions so the ω_1 coordinates of the peaks in the final spectrum are not necessarily those corresponding to the one-dimensional spectrum.
3. The mixing period. The coherence, which evolves in t_1, is transferred into observable magnetisation during the mixing period, the nature of which, therefore, determines the type of correlation information produced by the experiment.
4. The detection period. The frequency of the single-quantum coherence that is finally observed determines the ω_2 coordinates of the resulting peaks so these are never anything other than those observed in the corresponding one-dimensional spectrum.

1.5.1 Selection of Coherence Transfer Pathways

Phase cycling is used to select a particular sequence of events caused by the various radio-frequency pulses in a NMR sequence[21]. If the experiment uses several pulses there are very many possible sequences of events that lead to an observable signal, and phase cycling to discriminate between these is essential if a readily interpretable spectrum is to be obtained. By using two phase detectors, the spectrometer detects both the x and y components of the transverse magnetisation in the rotating frame. As the magnetisation vector precesses in the rotating frame, oscillating signals are produced by the two-

phase detectors, and these, once digitised, become the familiar free induction decay (FID). The position of the vector at the start of the FID gives the phase of the corresponding line in the spectrum. Normally, one axis at the start of the FID gives an absorption mode signal while alignment at other positions gives different phases. Changing the pulse phase by 90^0 causes the pulse to rotate the equilibrium magnetisation about a different axis and hence the vector appears in a different position in a transverse plane. This different position corresponds to a different phase for the line in the spectrum. The central idea is that wanted signal is shifted in phase by changing the phase of a pulse and, if the signal is to add up in the course of time averaging, the receiver phase must be altered so as to follow the phase change caused by the pulse. Likewise an unwanted signal can be cancelled by shifting its phase and keeping the receiver phase fixed.

The term coherence is a generalisation of the idea of transverse magnetisation. NMR experiments observe this magnetisation, and since the selection rule for normal NMR is $\Delta m = \pm 1$, transverse magnetisation is termed single quantum coherence. The single refers to the fact that only single spin flips are associated with the coherence.

Other coherences involving more than one spin flip can exist. For example, double quantum coherences correspond to transitions with $\Delta m = \pm 2$, triple to those with $\Delta m = \pm 3$ and so on. Note the only single quantum coherence gives rise to a directly observable signal.

At any stage in an experiment, it is possible to classify the coherences present into the various orders, that is zero, single, double etc. Each order is said to correspond to a different coherence level. In formal terms the density operator,

σ, can be expanded into components, σ_p, corresponding to different coherence levels, p:

$$\sigma = \sum_{-p_{max}}^{p_{max}} \sigma_p \qquad \textbf{(1.30)}$$

A rf pulse may cause coherences to be transferred from one order to another; in contrast, free precession preserves the order of coherence. If the density operator is expanded in terms of product operators then the various orders can be associated with particular products of raising and lowering operators: for example, the operator I^+ corresponds to single quantum coherence on spin *I*, whereas the operator I^+S^+ corresponds to double quantum coherence between spin *I* and *S*.

During each delay or period of a given pulse sequence it is usually the case that the intention is to have only one order of coherence present. Thus, in double quantum spectroscopy the intention is to have double quantum coherence present during the evolution time t_1. The desired coherence level at any point in the sequence can be selected by an appropriate phase cycling and it is called coherence transfer pathway. Two further points should be noted: (1) the pathway must start at coherence level 0, as this corresponds to equilibrium longitudinal magnetisation, (2) the pathway must end at level –1, as it is only this level that corresponds to observable magnetisation.

1.5.2 Phase Cycling

The basis of all phase cycling procedures is the transformation of p-quantum coherence under a rotation about the z-axis:

$$\exp(-i\phi I_z)\, \sigma_p \exp(i\phi I_z) = \sigma_p \exp(-ip\phi) \qquad \textbf{(1.31)}$$

where σ_p has the same meaning as in Eq. **(1.30)**. A pulse, represented by a propagator U, can cause a transfer of coherence of order p into all possible orders p' limited only by the extent of the spin system so that:

$$U\sigma_p(-)U_{-1} = \sum_{p'} \sigma_{p'}(+)$$

where $\sigma(-)$ and $\sigma(+)$ are the density operators before and after the pulse. The effect of phase shifting the pulse is seen by applying Eq. **(1.31)**:

$$U(\phi)\sigma_p(-)U(\phi)^{-1} = \sum_{p'} \sigma_{p'}(+)\exp(-i\Delta p\phi) \qquad \textbf{(1.32)}$$

with $\Delta p = p' - p$. Hence, the phase shift imposed on the coherence by the phase shifted pulse $U(\phi)$ depends on the change in coherence order, Δp, produced. This property allows the separation of different coherence orders since the phase shifts imposed in this way are carried over into the detected signal.

Phase cycling involves repetition of the pulse sequence N_i times with addition of the resulting signals whilst incrementing the phase of the i^{th} pulse by an angle:

$\phi_i = 2\pi n_i/N_i$

where $n_i = 0, 1, 2, \ldots, N_i - 1$. Each of the N_i observed signals arises from all possible coherence transfer pathways. Their sum can be restricted to contributions from pathways involving a given change of coherence order at the i^{th} pulse by acquisition of the N_i^{th} signal with a concerted receiver reference phase shift. The appropriate shift corresponds to that imposed on the required coherence by the i^{th} pulse due to Eq. **(1.31)** and is thus:

$\phi_{ref} = -\Delta p_i \phi_i$

It should be noted here that the sign of ϕ_{ref} changes when the observable magnetisation is defined as I^- and all pathways end with p = -1 order coherence.

Implicit in the above discussion is the fact that, if the phase of the i^{th} pulse is shifted through an angle ϕ_i for N_i successive experiments, the change in coherence order, Δp_i, selected by the appropriate receiver phase shift, ϕ_{ref}, is not unique. Indeed, an infinite set of coherence transfer pathways will be selected with changes in coherence order at the i^{th} pulse of:

$\Delta p_i = \Delta p_i(\text{required}) \pm kN_i$

with k = 0, 1, 2,….It should be noted that the smaller the phase shift, ϕ_i, and the larger the number of experiments, N_i, the more unique a selection can be performed.

Shifting the receiver phase is by no means the only way in which the sum of set of N_i experiments can be restricted to a given coherence pathway. Phase shifting all pulses in the sequence through an angle of opposite sign and addition with constant receiver phase will ensure that the same effect is produced. This method of phase cycling is often necessary if the receiver is limited to phase shifts of $\pi/2$ radians.

1.5.3 Separation of Phase in Two-Dimensional Spectra

The preceding sections have described how the evolution of the spin system during the t_1 period of a two-dimensional NMR experiment is not directly observed but detected by virtue of the modulation it imposes on the initial amplitude of the signal acquired in t_2. Consequently, there is no simple equivalent of conventional ω_2 quadrature detection for determining the signs

of the ω_1 frequencies. An important strategy has been proposed that allow determination of the signs of the ω_1 frequency whilst still producing correlation spectra with pure phase two-dimensional line shapes[22]. In normal quadrature data acquisition a pair of data points, one from each quadrature channel, is taken at intervals of $1/f_s$, where f_s is the spectral width. These two data values are regarded as a complex time-domain point and the spectrum is obtained from such data by a complex Fourier transformation. In the Redfield modification[23] single data points are taken at twice this rate and the phase of the receiver reference oscillator is advanced by $\pi/2$ radians after each data point is taken (for this reason this method is often referred to as time-proportional phase incrementation or TPPI). The spectrum is then obtained by applying a real Fourier transformation. The overall effect of the procedure is to add frequency of $f_s/2$ to each point in the spectrum. Peaks, which have offsets between $-f_s/2$ and 0 appear between 0 and $f_s/2$, and those with offsets between 0 and $f_s/2$ appear between $f_s/2$ and f_s. Thus, for peaks in the range $\pm f_s/2$ aliasing about zero frequency is prevented and effective quadrature detection is achieved.

The same procedure can be used to achieve frequency discrimination in the ω_1 dimension of a two-dimensional NMR spectrum. The time t_1 is advanced in intervals of $1/(2f_1)$, where f_1 is the required spectral width in ω_1. Each time t_1 is incremented, the phase of the desired coherence evolving during t_1 is shifted by $\pi/2$ radians.

Consider the time-domain signal $A_2\cos(\Omega_1 t_1)$: the phase incrementation gives an extra modulation so it becomes

$$S(t_1,\omega_2) = A_2\cos(\Omega_1 t_1 + \pi t_1/2\delta), \qquad \textbf{(1.33)}$$

where δ is the sampling interval in the t_1 dimension and is $1/(2f_1)$. Eq. **(1.33)** can be written

$S(t_1,\omega_2) = A_2\cos(\Omega_1 t_1 + \Omega_c t_1)$

Where $\Omega_c = \frac{1}{2}(2\pi f_1)$; in other words, half the spectral width has been added to the frequency of each line. As was explained above this avoids aliasing of signals in the range $\pm f_1/2$. An absorption-mode line shape is retained.

2 Alkali Fulleride

2.1 Introduction

The vast majority of research on the fullerene-based solids has been done on C_{60}. In this molecule the carbon nuclei reside on a sphere of about 7 Å diameter, with the electronic wave functions extending inside and outside by about 1.5 Å. The diameter of the molecule is approximately 10 Å, and there is a 4 Å diameter cavity inside. The atoms are actually positioned at the 60 vertices of a truncated icosahedron (or "soccerball") structure, with 90 edges, 12 pentagons and 20 hexagons. The two different C-C bond lengths in C_{60} (1.40 Å and 1.46 Å), indicate that the π electrons are not delocalised evenly over all bonds[24]. (For comparison, the sp^3 bond in diamond is 1.544 Å, the C-C distance in graphite is 1.42 Å, and a typical double bond distance is about 1.35 Å). The 30 short bonds are on the edges that are shared by two hexagons; the bond length at the 60 edges shared by a hexagon and a pentagon are longer.

The C_{60} molecule is highly symmetric as symmetry elements of C_{60} include inversion symmetry, mirror plane, rotations by 72^o or 144^o around axes piercing the centres of two opposing pentagons, etc. At room temperature the C_{60} molecules undergo free molecular rotation and in time average the molecules look like spheres and all of the molecular sites are equivalent. The well defined molecular centres and the nearly free molecular rotation are not unique properties of the fullerene molecule, but are characteristic of many organic solids, where the binding is due to van der Waals forces, and the molecule is highly symmetrical[25]. The centres of the C_{60} molecules make a *fcc*

lattice, with a nearest-neighbour C_{60}- C_{60} distance that corresponds to the diameter of the molecule. At room temperature the size of the cubic unit cell is 14.17 Å, and the nearest-neighbour distance is 10.02 Å[26]. A schematic representation of the C_{60} solid is shown in Figure 3.

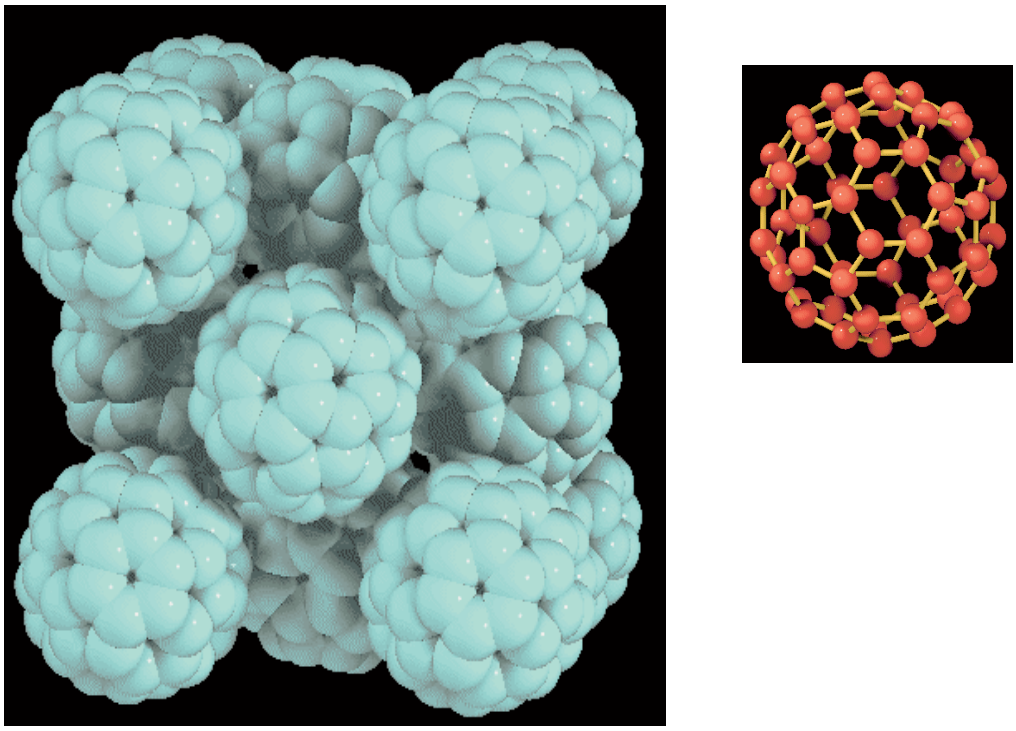

Figure 3: Structure for C_{60}: on the left hand the *fcc* structure is showed while on the right a single C_{60} molecule is represented.

The dimensions of a fullerene molecule are ten times larger then a typical atom. Even in a close-packed structure, large empty spaces between the molecules are available for intercalation by smaller atoms, ions or molecules. Due to the unsaturated character of the C-C bonds on the fullerene (C_{60} is an insulator as the conduction band is empty), there are plenty of electronic states to accept electrons from appropriate donors. The combination of alkali and alkaline-earth elements with fullerenes results in an unusual variety of AC_{60}

compounds with A = K, Rb, Na, Ca, Sr, Ba and Cs. Organic and inorganic molecules are also used to produce charge transfer salts with fullerenes. The term "doped fullerene" is often used to describe the product. In the close-packed *fcc* structure the interstitial sites have either octahedral or tetrahedral symmetry. The tetrahedral sites are smaller, and there are twice as many of them as octahedral sites. Up to now, the existence of different stable phases of A_xC_{60} with x = 0-4, 6, 10 is well established (see Figure 4). The x = 3 phase is the most widely studied since superconductivity has been observed up to temperatures exceeding the maximum critical temperatures of organic as well as regular inorganic superconductors[27]. The conduction band of these materials derives from the LUMO of the C_{60} molecule that is a three-fold degenerate t_{1u} electronic level of the molecule with icosahedral symmetry. The insulating character of phases x = 0 and 6 is easy to understand as it corresponds to the t_{1u} level being either completely empty or filled. The compound AC_{60}[28,29] where A represents Rb or Cs is also a remarkable system since it forms a variety of phases with interesting electronic and magnetic properties related to the low density of valence electrons. A comparison of AC_{60} and A_3C_{60} may be helpful in deciding questions like how important are intramolecular correlations for the occurrence of superconductivity[30]. Above approximately 350-400 K these compounds have similar face centered cubic (*fcc*) structures with only the octahedral sites occupied[31] by alkaline ions in AC_{60} and both octahedral and tetrahedral sites occupied in A_3C_{60}[32]. In AC_{60} this phase shows paramagnetism[33], suggesting a large degree of localization of the electrons on the fullerene molecules.

The first of the AC_{60} compounds was discovered by Winter and Kuzmany[28] who carried out Raman measurements on KC_{60} at high temperatures. At the time it was believed that the composition was not stable at lower temperatures[34] and it separated into K_3C_{60} and C_{60}. Chauvet *et al.*[35] have shown that RbC_{60} is in fact stable upon cooling, but there is a structural change in the 350-400 K temperature range. Later, a very pronounced first-order phase transition was found by optical, electrical transport, ESR and direct thermodynamic measurements. The surprising feature of the low-temperature structure is that the nearest neighbour C_{60}-C_{60} distance is only 9.1 Å, less than the diameter of a single C_{60} molecule. The symmetry of the *fcc* structure is lost and the distance between C_{60} molecules seems to be shortened along one of the axes (the a axis). In view of the short nearest-neighbour distance Pekker *et al.*[36] suggested that in this direction the C_{60} ions are covalently bound, and the lower temperature phase consists of a conductive linear polymer.

The $(AC_{60})_n$ polymers are formed spontaneously below 400 K from the monomer AC_{60} salts. The crystal structure of the polymer suggests a strongly anisotropic electronic structure. Powder X-ray diffraction studies[37] confirmed that this unusually short distance is indicative of the formation of linkages between fullerene molecules formed by a [2+2] cycloaddition[36] resulting in polymeric chains along the a-axis (Figure 5).

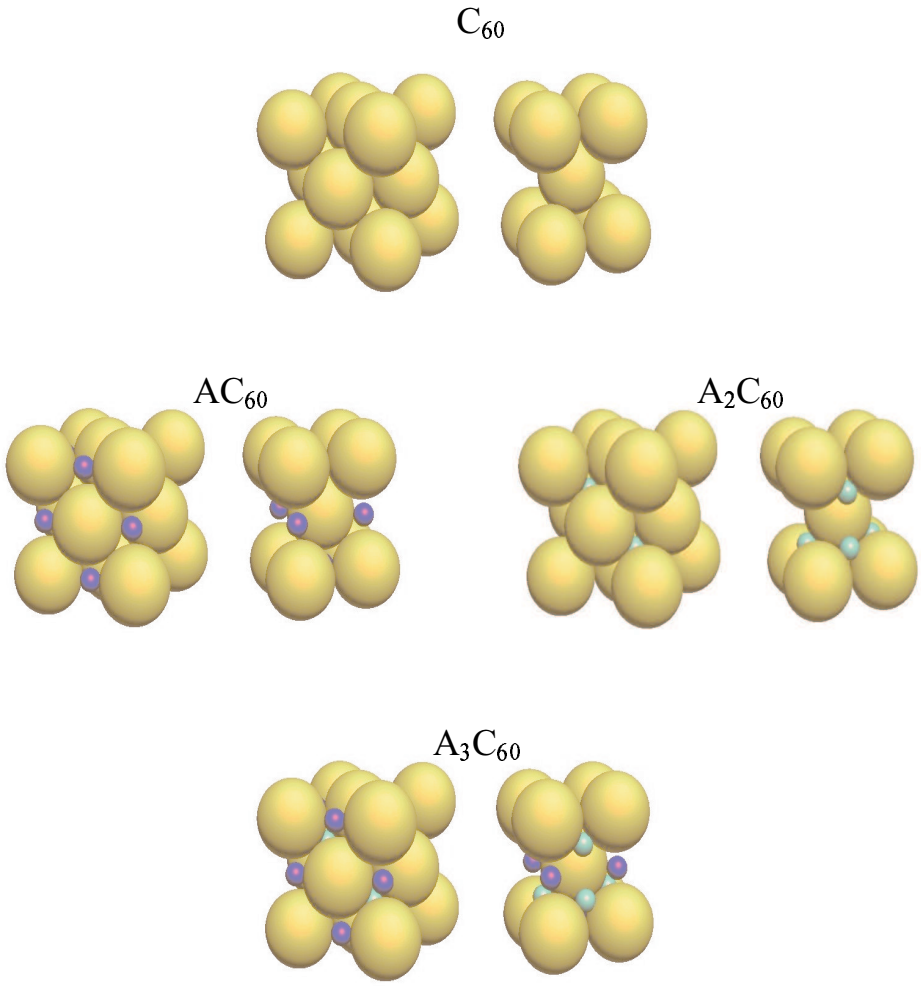

Figure 4: Two different representations of the C_{60} structure are shown to highlight the octahedral (on the left) and tetrahedral holes of the fcc structure. It is possible to fill the holes with alkaline atoms in order to obtain new compounds that have different structures and properties from the C_{60}. While C_{60} is an insulator A_3C_{60} is a superconductor.

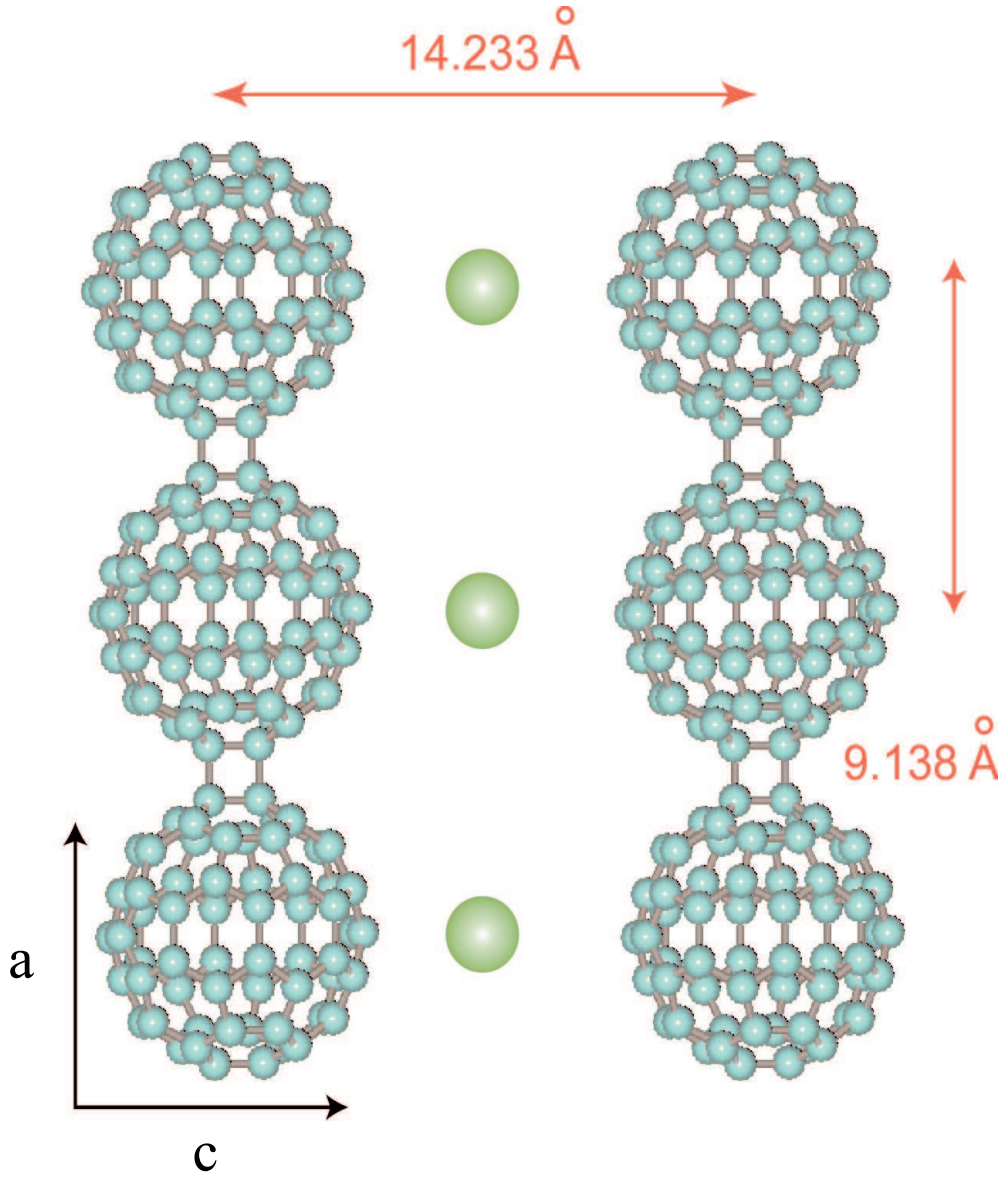

Figure 5: Below 350 K AC_{60} shows a phase transition that has been interpreted as a polymerisation along the a axis.

Raman[38], neutron diffraction[39] and inelastic scattering[40] data largely support this model, although several structural details such as the deformation of the fullerene molecules[41] and the rotational orientation of the polymer chains[42] remain uncertain. Magnetic spin susceptibility and frequency-dependent conductivity measurements[43] suggest that the polymeric phase is a quasi one-dimensional metallic conductor with a phase transition to a magnetically ordered insulator occurring at temperatures below approximately 50 K.

Solid-state NMR spectroscopy has made several important contributions to the study of RbC_{60} and CsC_{60}. The variation with temperature of the ^{13}C, ^{87}Rb and ^{133}Cs resonance frequencies and spin-lattice relaxation times[33] provide evidence for a phase transition at 350 K associated with a qualitative change in electronic properties. NMR data showed that the high-temperature phases (HT) are paramagnets. Unpaired electrons are principally localized on individual C_{60}^{-} ions, with an exchange coupling of roughly 2 cm^{-1} between the localized electron spins. Thus electron-electron interactions dominate the electronic dynamics. This is in obvious contrast to the A_3C_{60} compounds, in which NMR and other data can be explained by a Fermi-liquid model in which electron-electron interactions play a relatively minor role[44].

^{13}C magic angle spinning (MAS) measurements at rates up to 18 kHz[45,46] provide sufficient spectral resolution to separate resonances from inequivalent sites on the fullerene molecule with resonance frequencies determined by the sum of Knight shift and chemical shift contributions. Spectral intensities give an indication of the number of carbon atoms associated with each resolved resonance, and measurements of the shift anisotropy suggest that the carbon atoms comprising the inter fullerene linkage are sp^3 hybridized. The hyperfine

interaction for each resonance is extracted from the temperature variation of the Knight shift. These NMR data confirm theoretical band structure calculations[47] which predict that the fullerene molecules are connected by insulating contacts and that electron transport is dominated by interchain hopping, suggesting a full three-dimensional character to the electronic structure. These results contradict the magnetic spin susceptibility and frequency-dependent conductivity measurements according to which the polymeric phase is a quasi one-dimensional metallic conductor[43].

At this stage it seems clear that to fully test models for the electronic structure by NMR the resonances must be assigned to the different carbon sites in the fullerene molecule. This step is significant since it yields a map of the hyperfine coupling constant around the fullerene, against which models of the band structure can be tested. Furthermore, such an assignment is a prerequisite to any more detailed NMR study of internuclear distances, which might resolve the structural questions. Only a fully and self-consistent reliable assignment of the 1D-^{13}C spectrum can affirm in a unique and unequivocal way which of the two models mentioned above is correct (see Figure 6).

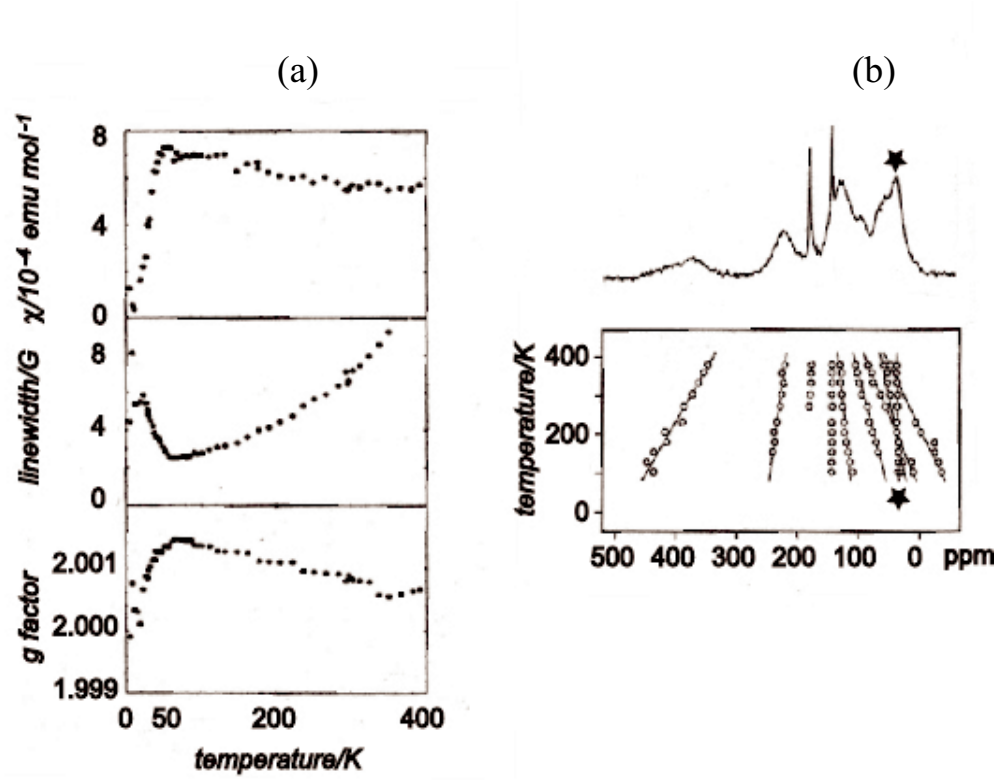

Figure 6: Two different electronic models have been proposed for AC_{60}. In (a) the ESR measurements are shown for RbC_{60} and a Quasi 1D model was proposed with an overlap of the electronic wave functions in the intermolecular regions along a[35]. In (b) some ^{13}C-MAS NMR data on RbC_{60} are shown where all but one ^{13}C shift varies with temperature. According to the authors[45] this temperature-independent resonance corresponds to an sp^3 hybridized interfullerene link and a full 3D band structure was proposed. In order to decide which of these models is correct more NMR measurements are required.

In a recent paper[48], T. M. de Swiet *et al.* used a two-dimensional ^{13}C MAS NMR correlation spectrum, as well as double resonance ^{13}C, ^{133}Cs MAS NMR measurements, to make a partial assignment of the ^{13}C MAS spectrum of the polymer phase of CsC_{60}. The pulse sequence used in that case is shown in Figure 7, together with the spectrum obtained. In order to identify pairs of bonded ^{13}C sites they performed ^{13}C MAS dipolar correlation spectroscopy[49]. The ^{13}C spins were allowed to precess freely for a time t_1. Next, the ^{13}C–^{13}C dipole-dipole interaction, normally removed by MAS, was recoupled using the POST-C7 pulse sequence[50], for a mixing time equal to four MAS periods. This allowed spin polarization to be transferred between ^{13}C nuclei that were sufficiently close in space. After the mixing time the signal was recorded as a function of t_2. Double Fourier transformation of the data revealed a plot with peaks along the diagonal, $\omega_1 = \omega_2$, resulting from polarization which was not transferred during the mixing period, and cross peaks resulting from polarization transfer between directly bonded carbon sites.

Although some useful information could be extrapolated, a problem with this study was that an unambiguous assignment of the resonances was not possible. First of all for each pair of nuclei bonded in the molecule a pair of cross peaks appeared together with the diagonal peaks and as a consequence the ^{13}C 2D spectrum obtained was very crowded (Figure 7). Furthermore, the pulse sequence used was very long and contained many pulses, so that a simpler pulse sequence is highly desirable. Finally, in the variant of the experiment[51] used in Ref. 48, the peaks in the spectrum identified interactions via through-space dipolar couplings and this can make the assignment very difficult and ambiguous. In order to choose between two different assignments, density

functional calculations (DFT) on a C_{60} trimer, which forms a piece of the polymer chain, were carried out. The trimer was terminated at each end with cycloaddition to CH_2-CH_2 groups. Only one of the two possible assignments was consistent with the hyperfine couplings calculated[45] from models[47,52] of the electronic structure. The assignment was based on a calculation that was required to distinguish between two possibilities.

In this thesis one of our aims was trying to obtain an unambiguous assignment of the ^{13}C NMR spectrum of the polymer phase of CsC_{60}, which was based solely on experimental data and was independent of any model for the electronic structure.

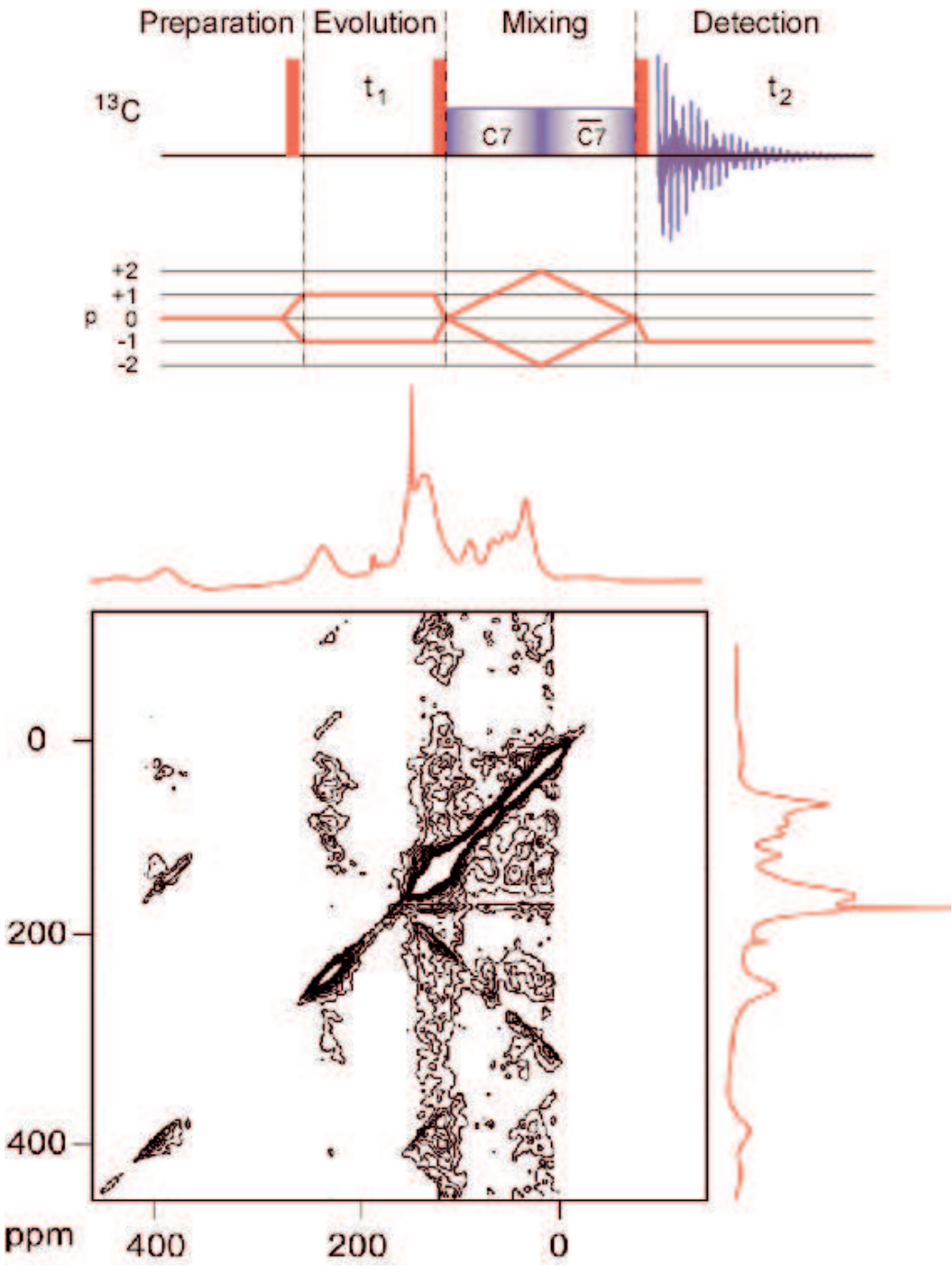

Figure 7: Previous studies on CsC_{60}: using the pulse sequence sketched above the dipolar coupling Hamiltonian is reintroduced during the mixing period and the spectrum obtained is shown.

2.2 Materials and Methods

In order to obtain sufficient sensitivity, samples of CsC_{60} were synthesized using ^{13}C-enriched fullerenes. These were prepared by packing and sintering ^{13}C-enriched amorphous carbon into graphite tubes to create ^{13}C-enriched rods. The fullerenes were subsequently produced by arcing a 60 A, 25V dc current between an ordinary graphite electrode and a ^{13}C enriched rod under a ~3 psi He atmosphere. Percent enrichment was verified by mass spectroscopy. The C_{60} was isolated from the soot via filtration and flash chromatography. Stoichiometric amounts of the enriched fullerenes and caesium were mixed, heated for one week at 350^{o}C, and then cooled to room temperatures over two days. A 50% ^{13}C-enriched CsC_{60} was so prepared.

Through-bond connectivities in disordered solids represents a challenge to NMR since the interaction driving the coherence transfer may be over an order of magnitude smaller than the line width. In the literature[53], the feasibility of obtaining carbon-carbon through-bond correlations in solids exhibiting line widths of several hundreds of hertz using an experiment named INADEQUATE (Incredible Natural Abundance Double Quantum Transfer Experiment) is reported.

The pulse sequences for refocused INADEQUATE (Carbon only) is shown in Figure 8. The phase cycling required to reject undesired single-quantum coherence may be derived from the coherence transfer pathways shown.

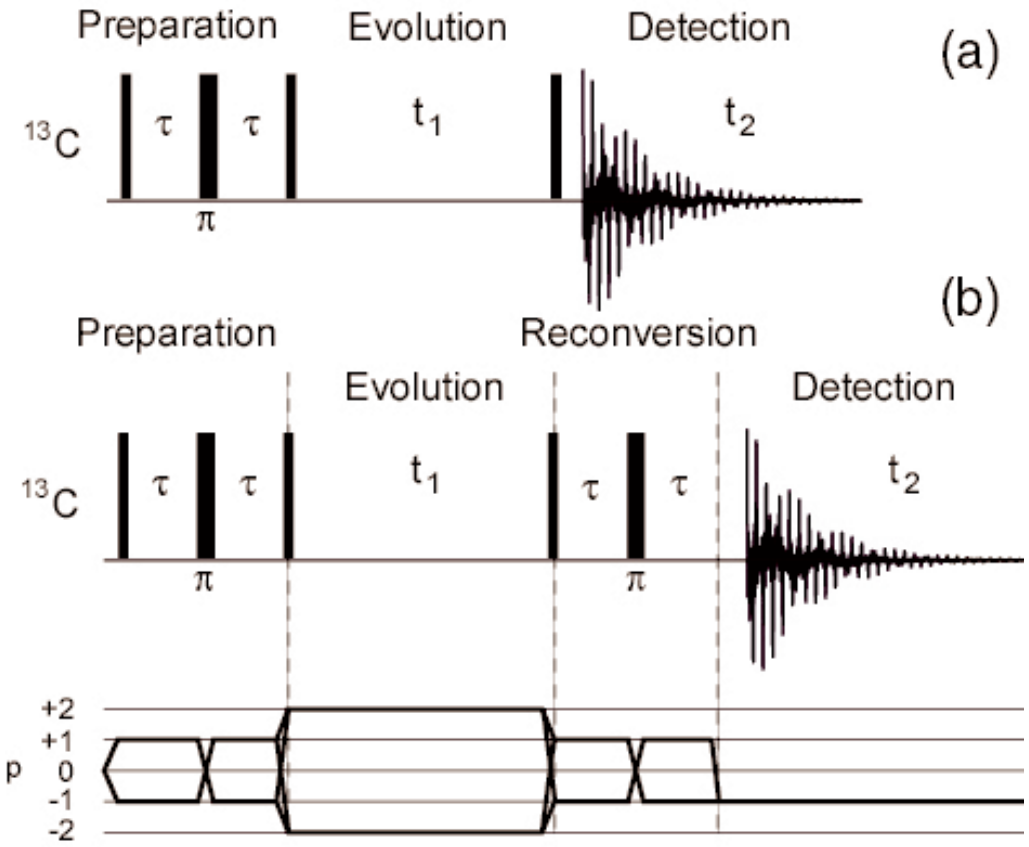

Figure 8: Ordinary (a) and Refocused (b) INADEQUATE pulse sequences. In this work only (b) was used for reasons explained in the text. The narrow vertical bars represent pulses with a flip angle of $\pi/2$, while the wide ones indicate a flip angle of π. The coherence transfer pathway for (b) is also shown.

The experiments are completely analogous to liquid-state versions[54]. ^{13}C magnetization generated by the first $\pi/2$ pulse evolves solely under the isotropic scalar coupling Hamiltonian for the preparation delay 2τ. This is because ^{13}C dipolar couplings and shift anisotropies are averaged by the fast magic angle spinning, and the π pulse in the middle of the preparation delay refocuses evolution due to the isotropic shift. In scalar-coupled spin systems the second $\pi/2$ pulse creates multiple-quantum coherences associated with normally forbidden transitions, and the phase of the second $\pi/2$ pulse is cycled to restrict these to double-quantum contributions. The generation of double-quantum coherence can be optimized under ideal conditions by choosing $\tau = 1/(4J_{CC})$ where J_{CC} is the ^{13}C scalar coupling constant. This coherence evolves during t_1 at the sum frequency of the coupled spins i and j

$$\omega_{DQ}^{ij} = \omega_{SQ}^{i} + \omega_{SQ}^{j} \qquad \textbf{(2.1)}$$

where ω_{SQ} is the normal shift frequency. In this refocused variant of the experiment double-quantum coherence is converted back to observable magnetization by the third $\pi/2$ pulse followed by a reconversion delay identical in duration to the preparation period. Magnetization is detected as normal in t_2, and a two-dimensional Fourier transformation of the resulting signal $S(t_1,t_2)$ gives a two-dimensional spectrum $S(\omega_1,\omega_2)$. Scalar-coupled pairs of nuclei can be identified by the appearance of two peaks in the spectrum at co-ordinates $\left(\omega_{DQ}^{ij}, \omega_{SQ}^{i}\right)$ and $\left(\omega_{DQ}^{ij}, \omega_{SQ}^{j}\right)$.

Let us analyse the effect of the basic sequence for the 1D version of INADEQUATE, in which the t_1 time between the third and the fourth pulse is

so short that we can neglect evolution during this time. The system consists of two spins called *I* and *S*, and its Hamiltonian is:

$H = \Omega_I I_z + \Omega_S S_z + 2\pi J I_z S_z$

Starting from a state of thermal equilibrium, the first pulse rotates the initial longitudinal polarization parallel to the x-axis, that is, yields a density matrix:

$\sigma_0 = I_x + S_x$

The second pulse serves to produce a spin echo. As in homonuclear J spectroscopy, the evolution of the system at time 2τ is entirely determined by the indirect interaction. At time 2τ, just before the third pulse, the density matrix is then:

$\sigma_1 = (I_x + S_x)\cos(2\pi J\tau) + 2(I_y S_z + I_z S_y)\sin(2\pi J\tau)$

After the third pulse, the density matrix becomes:

$\sigma_2 = -(I_z + S_z)\cos(2\pi J\tau) + 2(I_y S_x + I_x S_y)\sin(2\pi J\tau)$

The first term on the right-hand side corresponds to 0-Q coherence. As for the second term, it corresponds, to ±2-Q coherence, and it is the only part of σ_2 that is retained by the 2-Q filter. It is transformed by the fourth pulse into:

$\sigma_3 = -2(I_y S_z + I_z S_y)\sin(2\pi J\tau)$.

The last pulse serves to produce a spin echo and, as before, the evolution of the system after the time 2τ is entirely determined by the indirect interaction. Just before the acquisition time, the density matrix is then:

$\sigma_4 = -(I_y S_z + I_z S_y)\sin(4\pi J\tau) - 2(I_x + S_x)\sin^2(2\pi J\tau)$

In case of broad lines is possible to neglect the dispersive part of the signal (first term on the right side of the equation) and so the observed signal is:

$S = S_0 \sin^2(2\pi J\tau)\times\exp(-4\tau/T_2)$

Where T_2 is the relaxation time for that system. From the last equation it is possible to see that for first-order spin coupling, optimum conversion into double-quantum coherence requires that

$\tau = 1/(4J_{CC})$

and it is zero for $\tau = 1/(2J_{CC})$.

If the τ delay is synchronized with the rotation, $\tau = n/\omega_R$, the overall efficiency of an INADEQUATE sequence depends on one hand on the efficiency of the excitation of the double quantum coherences, which depends periodically on τ, and on the other hand on the decay of carbon magnetization during the τ delays. Efficiency is also affected by cancellation or addition effects during the detection of anti-phase or in-phase line shapes respectively in t_2. Ordinary INADEQUATE (Figure 8 (a)) yields anti-phase line shapes while refocused INADEQUATE (Figure 8 (b)) yields in-phase line shapes. Thus, at first glance, for solid systems, refocused INADEQUATE may seem to be more sensitive because of the detection of in-phase line shapes. However, in this case loss of signal due to relaxation occurs during two τ-π-τ delays instead of only one for the ordinary INADEQUATE sequence. On the other hand, it has been shown[55] that the refocused INADEQUATE experiment is particularly effective in disordered systems. In these cases a substantial contribution to the apparent line width due to distributions of shift frequencies can be refocused by a π pulse. Lesage *et al.*[55] showed that is advantageous to perform a refocused INADEQUATE for samples presenting a large ratio T_2'/T_2^*, where T_2' is the homogenous spin-spin relaxation time and T_2^* is the inhomogeneous line broadening, in this case mainly due to a chemical shift distribution.

In order to decide which pulse sequence was in our case more convenient, the value of T_2' had to be measured for polymer CsC_{60} in a spin echo experiment, in which a 180^0 pulse is added to a normal single pulse experiment and the time τ_1 is changed (Figure 9):

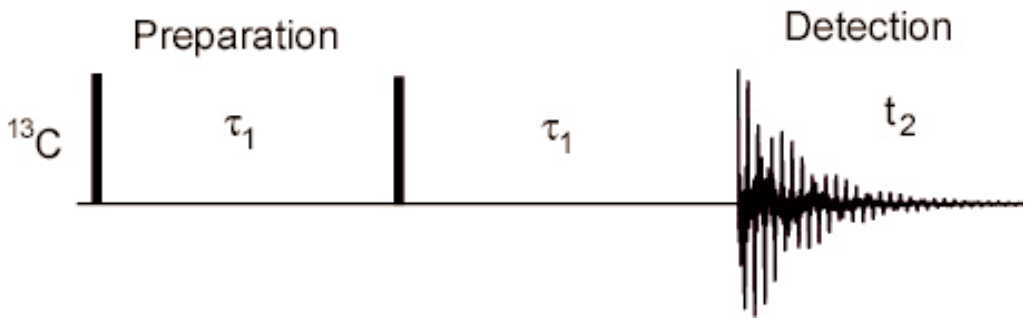

Figure 9: Pulse sequence for the spin-echo experiment

2.2.1 Experimental set-up

All the experiments featured for the CsC_{60} were acquired on a Varian Chemagnetics Infinity spectrometer operating at a proton Larmor frequency of 300 MHz on approximately 10 mg of material packed into a 3.2 mm MAS rotor spinning at 17 kHz. The full spectral width was 50 kHz, the free induction decay was acquired for 20.48 ms and a relaxation delay of 5 s was inserted between scans. Spin-echo experiments were performed with echo time up to 15 ms.

2.3 Results and Discussion

2.3.1 1D Spectrum

The ^{13}C MAS spectrum of CsC_{60} recorded at room temperature and a MAS rate of 17 kHz (Figure 10) shows Knight-shifted resonances which extend well beyond the normal ^{13}C chemical shift range. The linkage site which is sp^3 hybridised is expected to have a chemical shift of 30-45 ppm[45] and can be assigned to peak (i). Other sites on the fullerene molecule are expected to be shifted from the C_{60} position of 143 ppm by the Knight shift. Peaks (a), (b) and (c) have substantial positive Knight shifts and hyperfine couplings. The small differences between this spectrum and that in Ref. 48 arise from variations in Knight shifts due to sample heating effects arising from the spinning. As described in Ref. 48, the spectrum fits to 11 Lorentzian lines, with the resonances at 143 ppm and 179 ppm corresponding to residual unpolymerized C_{60} and high temperature cubic CsC_{60}, respectively. The complexity of the MAS spectrum and the broad lines arising from shift distributions caused by effects such as incomplete polymerization mean that recording a two-dimensional scalar correlation spectrum of CsC_{60} is an experimentally challenging task.

Two approaches to the development of scalar correlation experiments for solids have been described recently. The first of these[55] relies on refocusing the inhomogeneous linewidth to improve the effective resolution so that scalar couplings can be resolved and standard solution-state pulse sequences, such as INADEQUATE[56], can be used. The second[57,58] involves magnetization transfer under an isotropic mixing Hamiltonian induced by a MAS-synchronized rf pulse sequence which removes resonance offsets without

inadvertently recoupling dipolar interactions. Sample heating concerns and the need to distinguish any multiple-bond transfer dictated the choice of the first approach here.

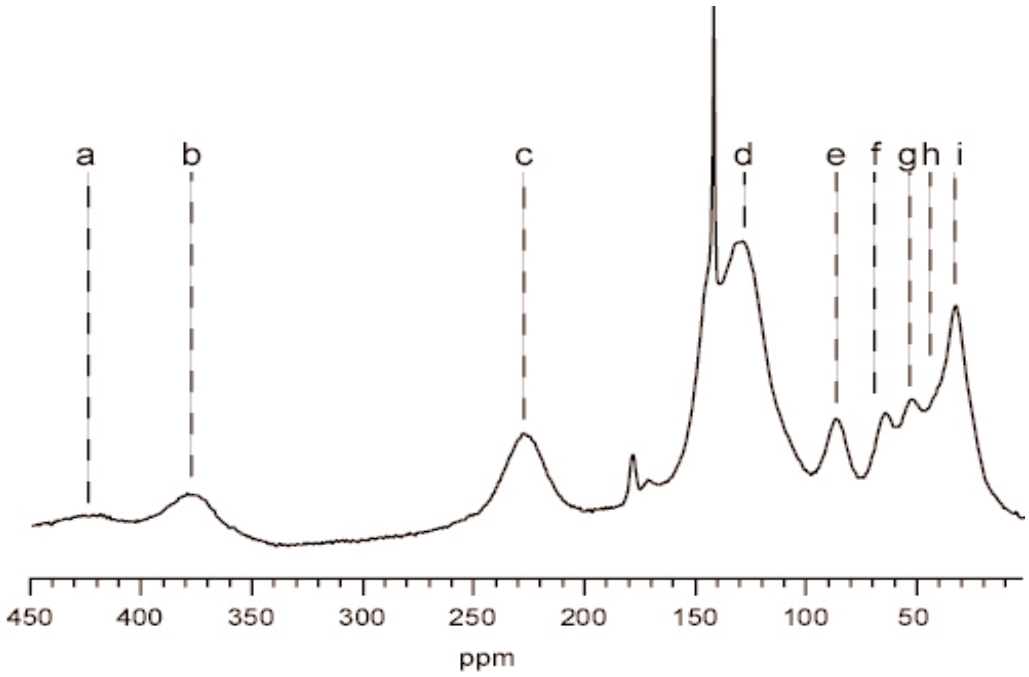

Figure 10: ^{13}C MAS spectrum of polymer CsC_{60}, recorded using parameters described in the text, showing the designations of the peaks used in this work. Note the Knight-shifted resonances which extend well beyond the normal ^{13}C chemical shift range.

2.3.2 T_2 measurements

In Table 1 T_2' values are listed as obtained from the experimental data shown in Figure 11, where some of the curves recorded from the spin-echo experiments are presented.

Peak/ ppm	T_2'/s
35	0.0056
40	0.0056
55	0.0054
65	0.0056
90	0.0054
115	0.0050
130	0.0048
230	0.0048
373	0.0048

Table 1: Values of T_2' for each peak of the 1D spectrum of Figure 10 calculated using the spin-echo pulse sequence schematically depicted in Figure 9. Note how the T_2' values decrease for peaks with larger ppm values.

It is possible to notice that there is a small but consistent decrease of T_2' value with increasing Knight Shift. This means that nuclei with larger Knight Shift are likely to relax quicker showing that the loss of coherence is conduction electron mediated.

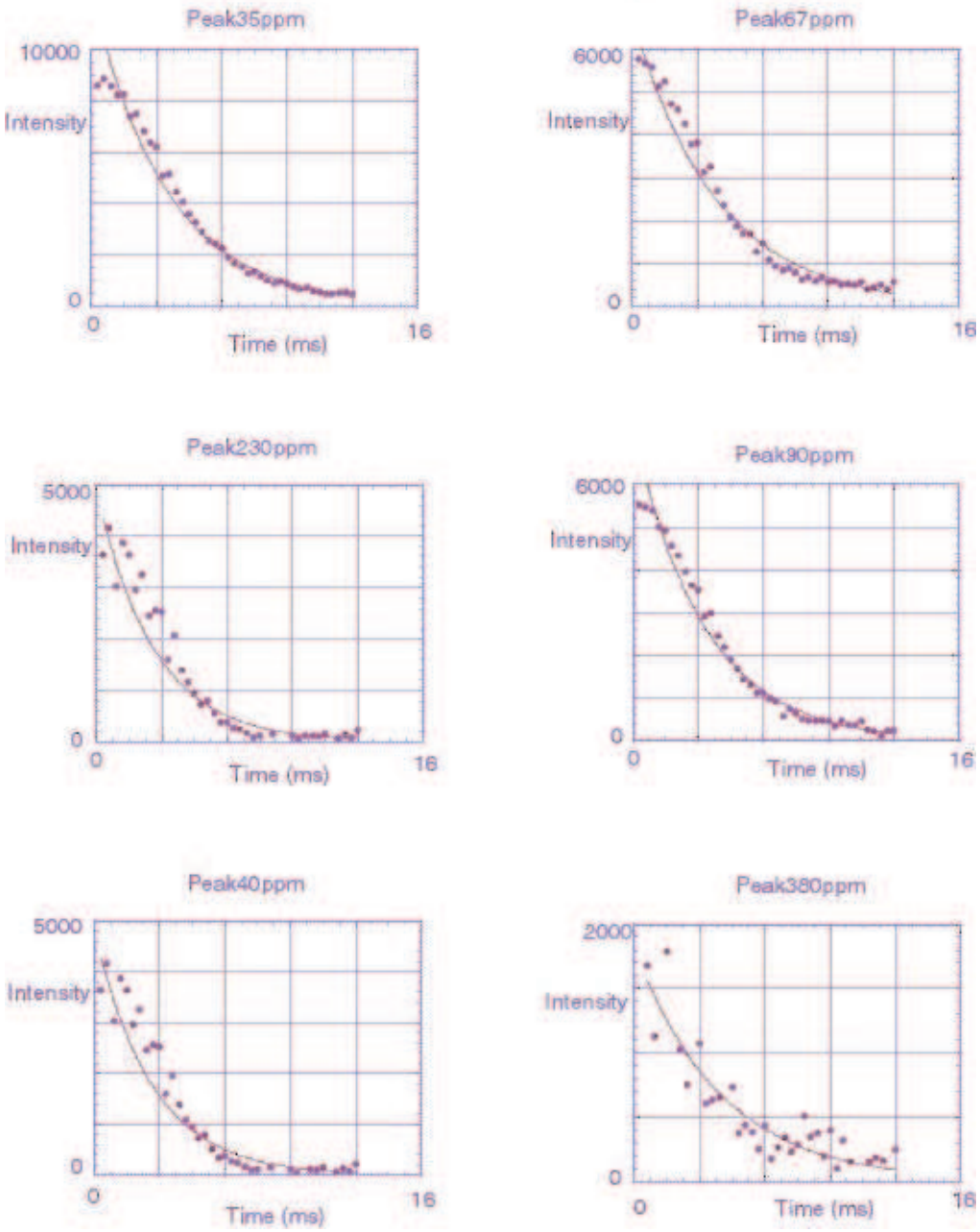

Figure 11: $T_2^{'}$ fitting from the data obtained using the pulse sequence of Figure 9.

From Table 1 it is possible to see that the value of T_2' found was of the order of 5 ms, giving values of the ratio T_2'/T_2^* of between 10 and 25 depending on the site. In Figure 12 (a) simulated spectrum with the apparent line width is shown together with the experimental 1D spectrum. It is straightforward to draw the conclusion that the refocused INADEQUATE will give us more detailed information about the structure of the sample than the normal INADEQUATE as the broadening due to the inhomogeneous line width is considerable in this particular case.

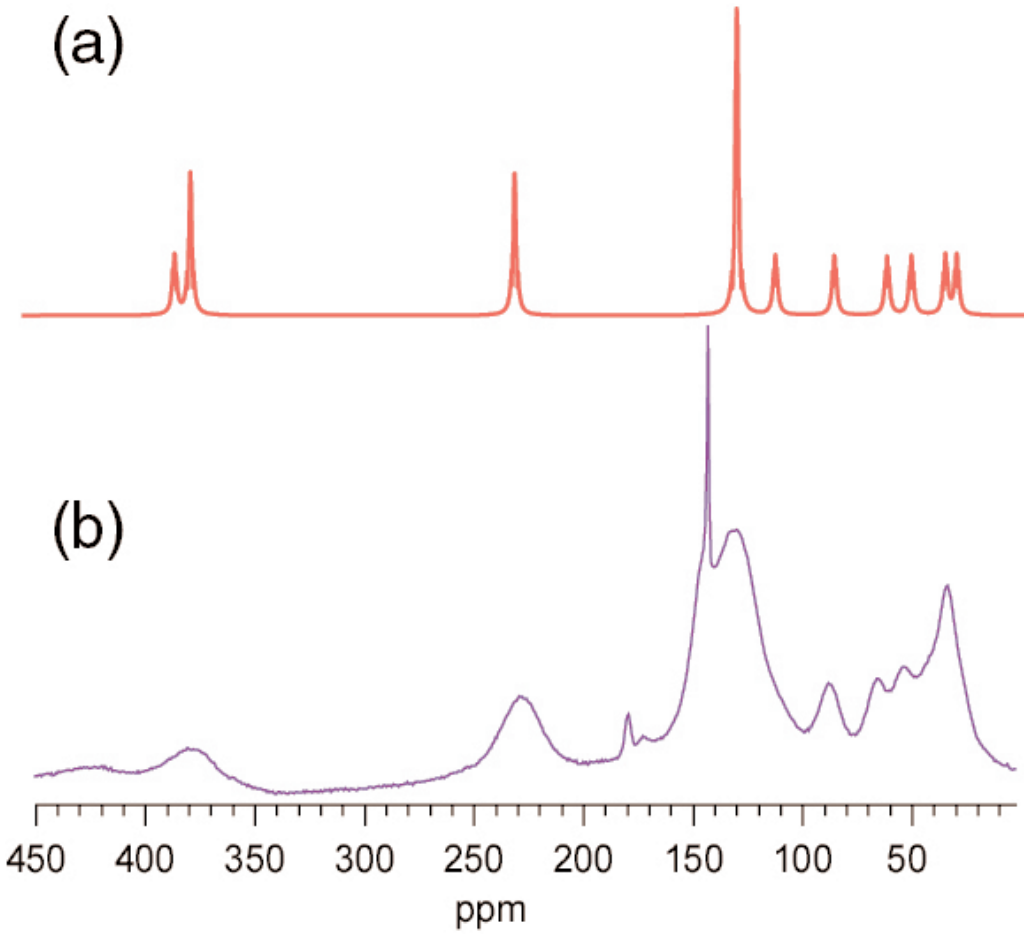

Figure 12: Comparison between the simulated (a) and experimental (b) 1D spectrum of CsC_{60}. In (a) the inhomogeneous line width was removed and the homogenous line width calculated by spin-echo measurements was used instead. Note that for this sample the inhomogeneous line width is very large due mainly to a distribution of chemical shifts.

2.3.3 Refocused INADEQUATE 2D Spectra

^{13}C refocused INADEQUATE spectra of polymer CsC_{60} were recorded with preparation delays (2τ) of between 2.14 and 6.14 ms. There were 150 values of the evolution time t_1 and the dwell time in this dimension was 5 μs. Pure absorption two-dimensional lines were achieved using TPPI. All other experimental parameters were as given for the one-dimensional spectrum of Figure 10. Figure 13 shows a refocused INADEQUATE spectrum of polymer CsC_{60} recorded with a preparation delay (2τ) of 2.94 ms. In (a) a region is plotted with 5 positive contour levels between 17.5 and 100 per cent of the maximum intensity. This plot allows individual peaks in the crowded upper right hand quadrant of the two-dimensional spectrum to be discriminated from one another, but the levels are too high to allow a number of broader and/or less intense peaks in the lower half of the spectrum to be observed. To overcome this cosmetic problem, the region of the spectrum with ω_1 between 400 and 550 ppm has been extracted and plotted in (b) with 5 positive contour levels between 6 and 50 % of maximum intensity. It should be noted that the co-ordinates of all the peaks visible in Figure 13 (a) and (b) obey Eq. **(2.1)**, except for one at (450 ppm, 29 ppm) for which the ω_2 co-ordinate is outside the range observed in the MAS spectrum. Peaks visible in Figure 13 were reproduced in all the refocused INADEQUATE spectra recorded. Each of the sum frequencies observed in the ω_1 dimension of the spectrum in Figure 13 can be assigned to a pair of carbon sites that are directly bonded in the molecule. All the peaks in the MAS spectrum can be assigned to sites in this way, using two further pieces of experimental evidence, namely that the sp^3 linkage site (1) corresponds to peak (i) which has been verified previously[45,46]

and that the pairs of sites (2)/(3) and (8)/(9) can be distinguished by the REDOR experiments described in Ref. 48.

The peak positions in the refocused INADEQUATE spectrum are summarized in Figure 14, which also gives the resulting assignment of the MAS spectrum. Only one of the sum frequencies expected on the basis of the assignment is missing from the spectrum; this is discussed in more detail below. It should be noted that the difference between the observed ω_1 frequency and the sum of the corresponding single-quantum frequencies is never more than 10 ppm and is less than 3 ppm in the vast majority of cases. In slices of the two-dimensional spectrum it is possible to resolve a shoulder at 114 ppm on the high-field side of peak d which has been designated d*[48] and can be assigned to site (13) on the basis of its connection to site (9). Resonance (b) appears to be split into two separate peaks with the high-field peak at 375 ppm assigned to site (14) on the basis of its connections to sites (8) and (9). This last point can be verified by a careful inspection of the peak positions in the low-field region of Figure 13 (b). The assignments given in Figure 14 are consistent with the peak positions observed in all the refocused INADEQUATE spectra recorded.

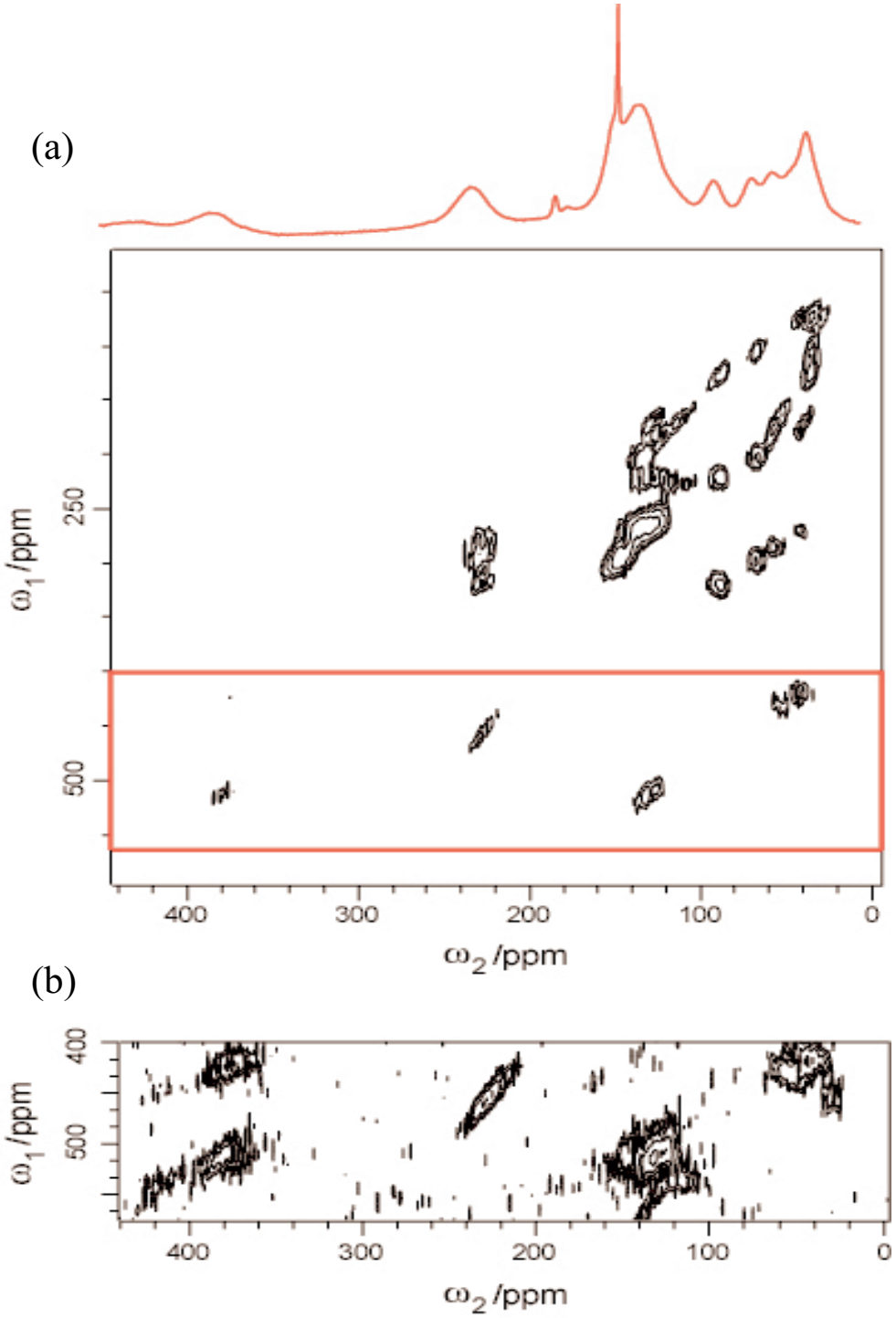

Figure 13: Part of a refocused INADEQUATE spectrum of polymer CsC_{60} recorded using parameters described in the text and a preparation delay (2τ) of 2.94 ms. In (a) 5 positive contour levels are plotted between 17.5 and 100 % of the maximum intensity. This allows individual peaks in the crowded upper right hand quadrant of the two-dimensional spectrum to be discriminated from one another. In (b) a region of the spectrum has been extracted and plotted with 5 positive contour levels between 6 and 50 % of maximum intensity. Scalar-coupled pairs of nuclei can be identified by the appearance of two peaks in the spectrum that share a common ω_1 frequency.

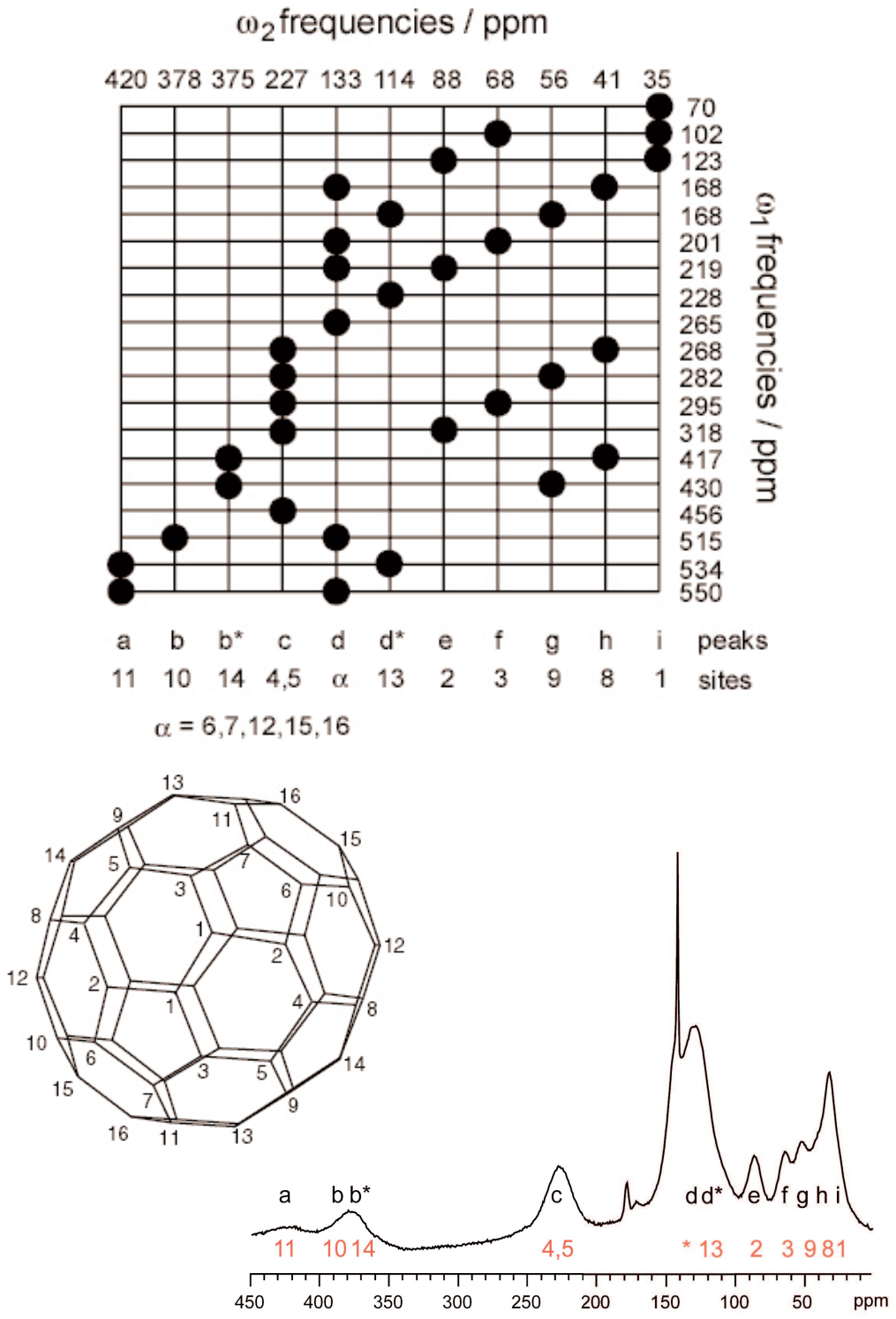

Figure 14: Summary of the peak positions in the refocused INADEQUATE spectrum, and the resulting assignment of peaks (a) to (i) in the MAS spectrum to sites (1) to (16) in the fullerene molecule. Note that peak positions obey Eq. **(2.1)** and that peak (d) results from the overlap of resonances due to sites (6), (7), (12),(15) and (16). In addition the structure of a single fullerene unit from polymer CsC_{60} is shown oriented such that the crystallographic a-axis and the polymer chain run approximately perpendicular to the paper. The inequivalent ^{13}C sites (1) to (16) are labeled.

2.3.3.1 Equivalence peaks

Several comments about the form of the spectrum are worthy of note, not least the fact that a number of peaks occur at co-ordinates $\left(2\omega^{i}_{SQ}, \omega^{i}_{SQ}\right)$, notably at ν_i frequencies of 70, 228, 265 and 456 ppm. In the following discussion these are referred to as "equivalence" peaks. Equivalence peaks would not normally be expected in a solution-state INADEQUATE spectrum, since magnetically equivalent nuclei have a vanishing scalar coupling even when chemically bonded. However, in materials such as polymer CsC_{60} the apparent linewidth arises in part from a superposition of resonances from nuclei made inequivalent by, for example, chain end effects, defects in packing or incomplete polymerization. Chemically bonded pairs of such inequivalent but unresolved nuclei will show a scalar coupling. It should be noted that the appearance of the equivalence peak at 70 ppm is further evidence that peak (i) does indeed correspond to site (1), since only a limited number of sites can result in this type of peak. This equivalence peak is the only one in the high-field part of the spectrum. The missing peak expected from the assignment is also an equivalence peak, namely that for site (14) at a ω_1 co-ordinate of 750 ppm. This part of the two-dimensional spectrum is not shown in Figure 13, as there is no evidence for a peak above the noise in this region. However, the large apparent line width for peak (b) in the MAS spectrum means this peak is expected to be weak.

2.3.3.2 Remote Peaks

With the large degree of isotopic enrichment in this sample of CsC_{60} so-called "remote" peaks connecting two non-bonded nuclei k and m that share a

common coupling partner l might also be expected. Such peaks are commonly observed in solution-state INADEQUATE spectra of abundant spins such as protons at frequencies given by $\left(\omega_{DQ}^{km}, \omega_{SQ}^{l}\right)$. However, they have not been observed to our knowledge for ^{13}C in solids, even with 100% isotopic enrichment.

In our spectra, a small number of remote peaks are just visible for the first time in solid-state NMR above the noise at longer preparation times, and their positions provide further verification of the assignment of Figure 14. Two examples taken from a refocused INADEQUATE spectrum with a preparation delay (2τ) of 5.9 ms are shown in Figure 15 where cross-sections parallel to ω_1 at (a) 130 ppm and (b) 348 ppm are shown. The high-field peak in Figure 15(b) is consistent with the assignment of peak (d*) at 114 ppm to site (13), since it arises from the remote connection between sites (5) and (13) via site (9).

The coherence transfer phenomena that give rise to these signals can be explained by considering a linear three-spin system. The system is assumed to be initially in thermal equilibrium, i.e. $\sigma(0) = I_{kz}+I_{lz}+I_{mz}$. For the sake of clarity, we consider the transformations of these terms individually, assuming that $J_{km}=0$, and neglecting residual longitudinal terms that remains after the excitation sandwich (first three pulses of Figure 8):

$$I_{kz} \xrightarrow{\pi J_{kl}\tau I_{ky}I_{ly}} \xrightarrow{\pi J_{lm}\tau I_{ly}I_{my}} 2I_{kx}I_{ly}\sin\pi J_{kl}\tau$$

$$I_{lz} \xrightarrow{\pi J_{kl}\tau I_{ky}I_{ly}} \xrightarrow{\pi J_{lm}\tau I_{ly}I_{my}} 2I_{ky}I_{lx}\sin\pi J_{kl}\tau\cos\pi J_{lm}\tau + 2I_{lx}I_{my}\cos\pi J_{kl}\tau$$

$$\cos\pi J_{lm}\tau - 4I_{ky}I_{lz}I_{my}\sin\pi J_{kl}\tau\sin J_{lm}\tau$$

$$I_{mz} \xrightarrow{\pi J_{kl}\tau I_{ky}I_{ly}} \xrightarrow{\pi J_{lm}\tau I_{ly}I_{my}} 2I_{ly}I_{mx}\sin\pi J_{lm}\tau$$

The resulting terms correspond to superpositions of zero and double quantum coherences. For simplicity, we consider $\tau = (2J_{kl})^{-1} = (2J_{lm})^{-1}$, and obtain immediately after the excitation sandwich

$\sigma(t_1 = 0) = 2I_{kx} I_{ly} - 4 I_{ky} I_{lz} I_{my} + 2 I_{ly} I_{mx}$.

These terms may be recast to give:

$$\sigma(t_1=0)=\{\frac{1}{2}(2I_{kx}I_{ly}+2I_{ky}I_{lx})\}-\{\frac{1}{2}(2I_{ky}I_{lx}-2I_{kx}I_{ly})\}+2I_{lz}\{\frac{1}{2}(2I_{kx}I_{mx}-2I_{ky}I_{my})\}-2I_{lz}$$

$$\{\frac{1}{2}(2I_{kx} I_{mx}+2I_{ky} I_{my})\}+\{\frac{1}{2}(2I_{ly} I_{mx}+2I_{lx} I_{my})\}-\{\frac{1}{2}(2I_{lx} I_{my}-2I_{ly} I_{mx})\}.$$

We concentrate on the double-quantum terms and eliminate the zero-quantum coherences by phase cycling, although in some situations their evolution may be of interest[5]. The double-quantum terms $\{\frac{1}{2}(2I_{kx} I_{ly}+2I_{ky} I_{lx}), \frac{1}{2}(2I_{ly} I_{mx}+2I_{lx} I_{my})\}$ are analogous to those found in a two-spin system. The third term carries information that cannot be derived from single-quantum methods. The evolution of this term is governed by the sum of the chemical shifts of the two remote spins, and by the couplings to the central spins I_l:

$$2I_{lz}\left(2I_{kx}I_{mx} - 2I_{ky}I_{my}\right) \xrightarrow{(\Omega_k I_{kz}+\Omega_m I_{mz})t_1} \xrightarrow{(\pi J_{kl} 2I_{kz}I_{lz}+\pi J_{lm} 2I_{lz}I_{mz})t_1}$$

$$2I_{lz}\left(2I_{kx}I_{mx} - 2I_{ky}I_{my}\right)\cos\Omega_{eff}t_1 \cos J_{eff}t_1 +$$

$$2I_{lz}\left(2I_{kx}I_{my} + 2I_{ky}I_{mx}\right)\sin\Omega_{eff}t_1 \cos J_{eff}t_1 +$$

$$\left(2I_{kx}I_{my} + 2I_{ky}I_{mx}\right)\cos\Omega_{eff}t_1 \sin J_{eff}t_1 +$$

$$-\left(2I_{kx}I_{mx} - 2I_{ky}I_{my}\right)\sin\Omega_{eff}t_1 \sin J_{eff}t_1 \qquad \textbf{(2.2)}$$

with $\Omega_{eff} = \Omega_k + \Omega_m$ and $J_{eff} = J_{kl} + J_{lm}$. If we consider a system with magnetically equivalent nuclei I_k and I_m, the effective frequencies are $\Omega_{eff} = 2\Omega_k$ and $J_{eff} = 2J_{kl}$. At the end of the evolution period, the $(\pi/2)_x$-mixing pulse

(fourth pulse of Figure 8) can only convert the first term in Eq. **(2.2)** into observable single-quantum magnetization. Thus we focus attention on the transformation of this term and retain only the observable part in the resulting density operator after a $(\pi/2)_x$-mixing pulse

$$\sigma^{obs}(t_1,t_2=0) = +\frac{1}{2} 4I_{kz}I_{ly}I_{mz}\cos(\Omega_k+\Omega_m)t_1\cos(J_{kl}+J_{lm})t_1 .$$

This anti-phase magnetization may be partly converted into in-phase magnetization by appending the sequence $[\tau/2\text{-}(\pi)_x\text{-}\tau/2]$ with $\tau \cong (2J_{kl})^{-1} \cong (2J_{kl})^{-1}$, and we obtain

$$\sigma^{obs}(t_1,t_2=0) = +\frac{1}{2} I_{ly}\cos(\Omega_k+\Omega_m)t_1\cos(J_{kl}+J_{lm})t_1\times\sin\pi J_{kl}\tau\ \sin\pi J_{lm}\tau + \text{anti-phase}$$

terms.

Residual anti-phase terms can be purged by applying the last $(\pi/2)_y$-pulse of Figure 8. Note that the sign of the I_{ly} term obtained is opposite with respect to the terms obtained in the two spin system. Thus in the refocused INADEQUATE spectra of CsC_{60} all signal associated with direct connectivity can be made to appear positive, while signals which arise from “remote” connectivities appear negative.

It should be noted that the remote peaks will occur only in the case that there is a particular configuration with 3 spins system though and not in the other cases. For that reason the signal is lot less intense than the normal peaks. Furthermore the signal will have a negative sign so is likely that lots of peaks get cancelled. For these reasons we do not observe many remote peaks apart from some rare exceptions cited above.

A simulation of the build up curve for remote peaks has been done and it is possible to see that the signal has negative intensity values. In Figure 16 such

simulation is shown, together with the simulation of the "ordinary" cross-INADEQUATE peaks. If the weak coupling Hamiltonian is used for the latter simulation, it is possible to see that the curves obtained are consistent with the analytical and experimental results. In Figure 17 the curves obtained adding the relaxation process (T_2 = 0.005 s from the spin-echo measurements) are also shown. It is now clear from the simulations that the build up of the signal intensity for the remote peaks happens at longer preparation delay and this is probably one of the reasons why the scientific solid-state community has missed them.

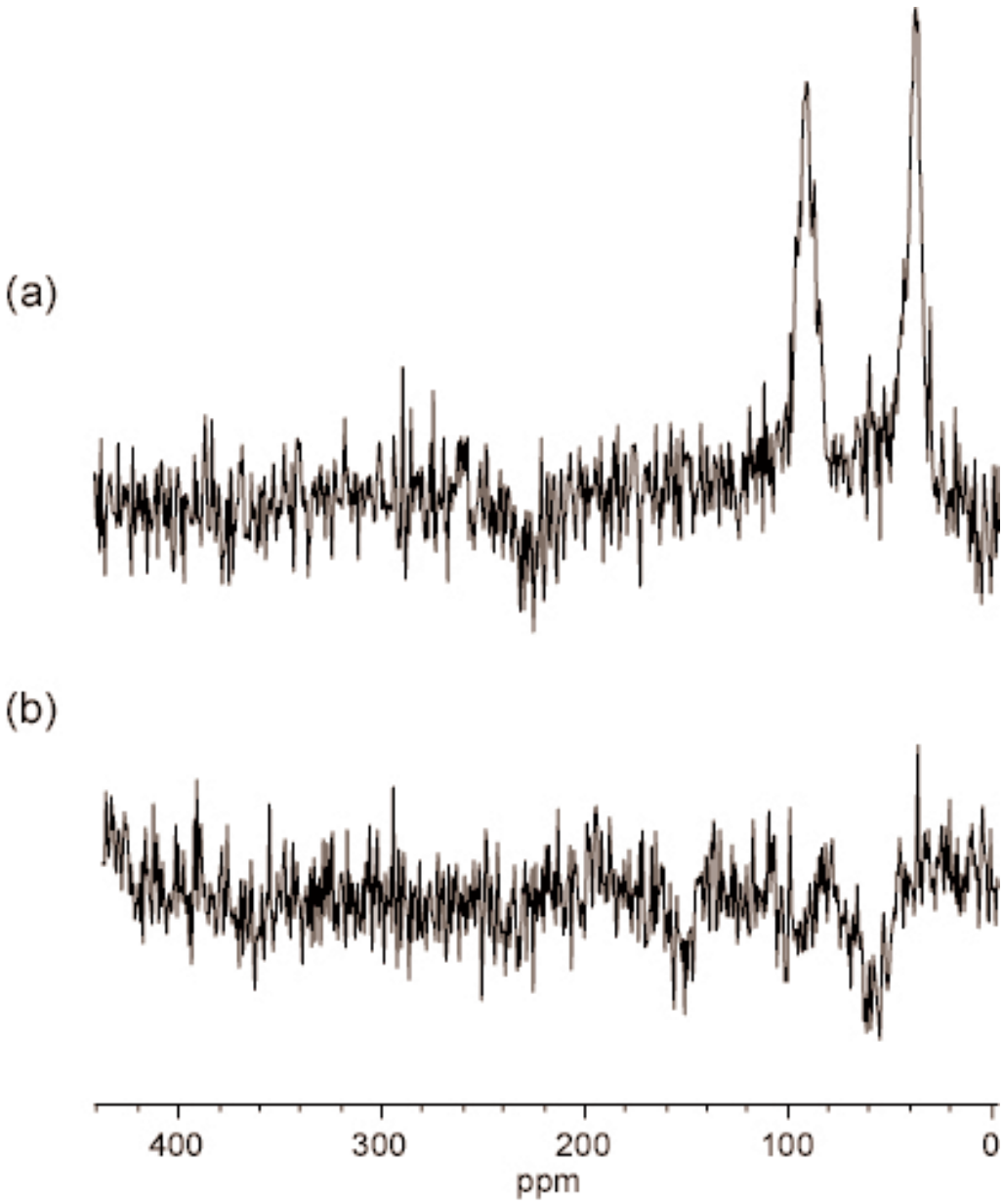

Figure 15: Cross-sections parallel to ω_2 taken from a refocused INADEQUATE spectrum of polymer CsC_{60} recorded using parameters described in the text and a preparation delay (2τ) of 5.9 ms at ω_1 frequencies of (a) 130 ppm and (b) 348 ppm. These show examples of remote peaks which connect two non-bonded nuclei which share a common coupling partner. Note that these peaks are of low intensity and opposite phase to the direct peaks as expected. In (a) the negative peak at 228 ppm arises from the remote connection between sites (2) and (8) via site (4), while in (b) the negative peak at 55 ppm arises from the remote connection between sites (5) and (13) via site (9). In (a) there is some interference at high field from the direct peaks connecting sites (1) and (2) which have maximum intensity at ω_1 = 123 ppm.

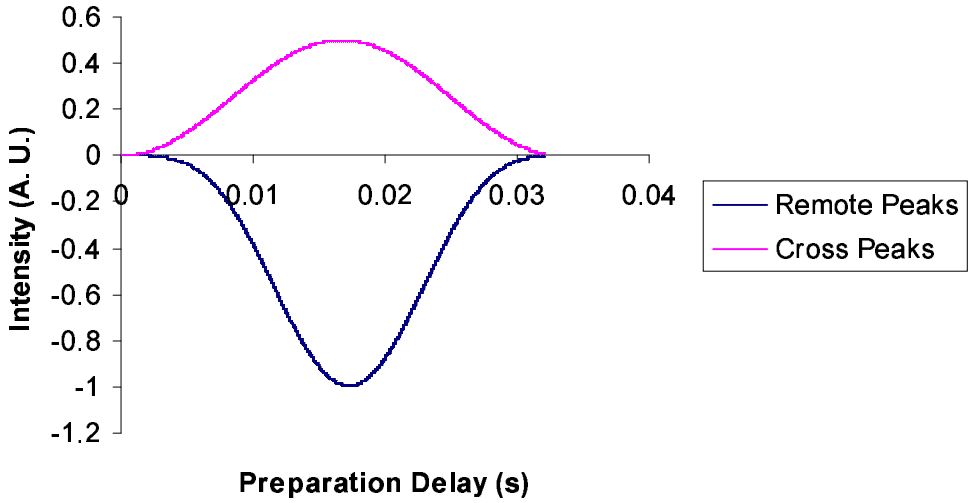

Figure 16: Simulations of the intensity of the build up curves for Remote peaks and Cross peaks neglecting the relaxation process. Note that the Remote Peaks intensity is negative.

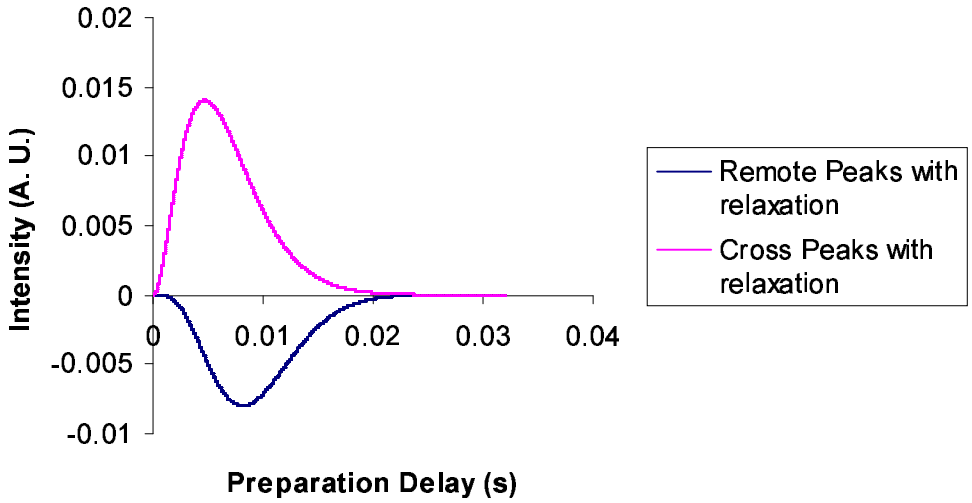

Figure 17: Build up of the Remote and Cross Peaks as in Figure 16 with the inclusion of the relaxation process (T_2 = 0.005 s as calculated with the spin-echo experiment). Note that in this case the maximum intensity is reached at different Preparation Delay values ($2\tau \cong 3$ ms and 8 ms for Cross and Remote Peaks respectively) and also the absolute intensity of the Remote Peaks is smaller than the one of the Cross Peaks.

2.3.3.3 Assignment

In Ref. 48 two possible assignments were found to be consistent with the NMR data. The difference between these hinges around sites (4) and (5) which are assigned to either peak (c) or peak (d) in the two possibilities. A choice between these could only be made on the basis of calculated hyperfine coupling constants, which suggested the former was the correct assignment. However, this ambiguity is removed by the refocused INADEQUATE spectrum due to the observed sum frequencies which involve peak d*. In both possibilities this peak corresponds to site (13) which is bonded to sites (11) and (9). In the second possibility, designated choice B in Ref. 48, peak (g) is assigned to site (11), while site (9) contributes to the intense peak (d). This assignment is not consistent with the refocused INADEQUATE spectrum, since it requires the appearance of peaks with a sum frequency of 247 ppm at (247 ppm, 133 ppm) and (247 ppm, 114 ppm) which are not observed. On the other hand, the possibility designated choice A in Ref. 48 is consistent with the refocused INADEQUATE spectrum. This choice requires peaks with a sum frequency of greater than 500 ppm linking peak (d*) with one of the low-field peaks (a) or (b). Such peaks are apparent in the refocused INADEQUATE spectrum, particularly at the lower contour levels plotted in Figure 13 (b). Since the whole assignment depends on the peaks which involve site (13), cross-sections through the spectrum of Figure 13 parallel to ν_2 at ν_1 frequencies of 168 ppm, 228 ppm and 534 ppm are shown in Figure 18 (a), (b) and (c) respectively. The quality of the refocused INADEQUATE spectrum is sufficient to assign peak (a) to site (11) on the basis of the low-field peak at (538 ppm, 420 ppm) in Figure 18 (c). It should be noted that

although the signal to noise is low this peak is visible in all the refocused INADEQUATE spectra recorded.

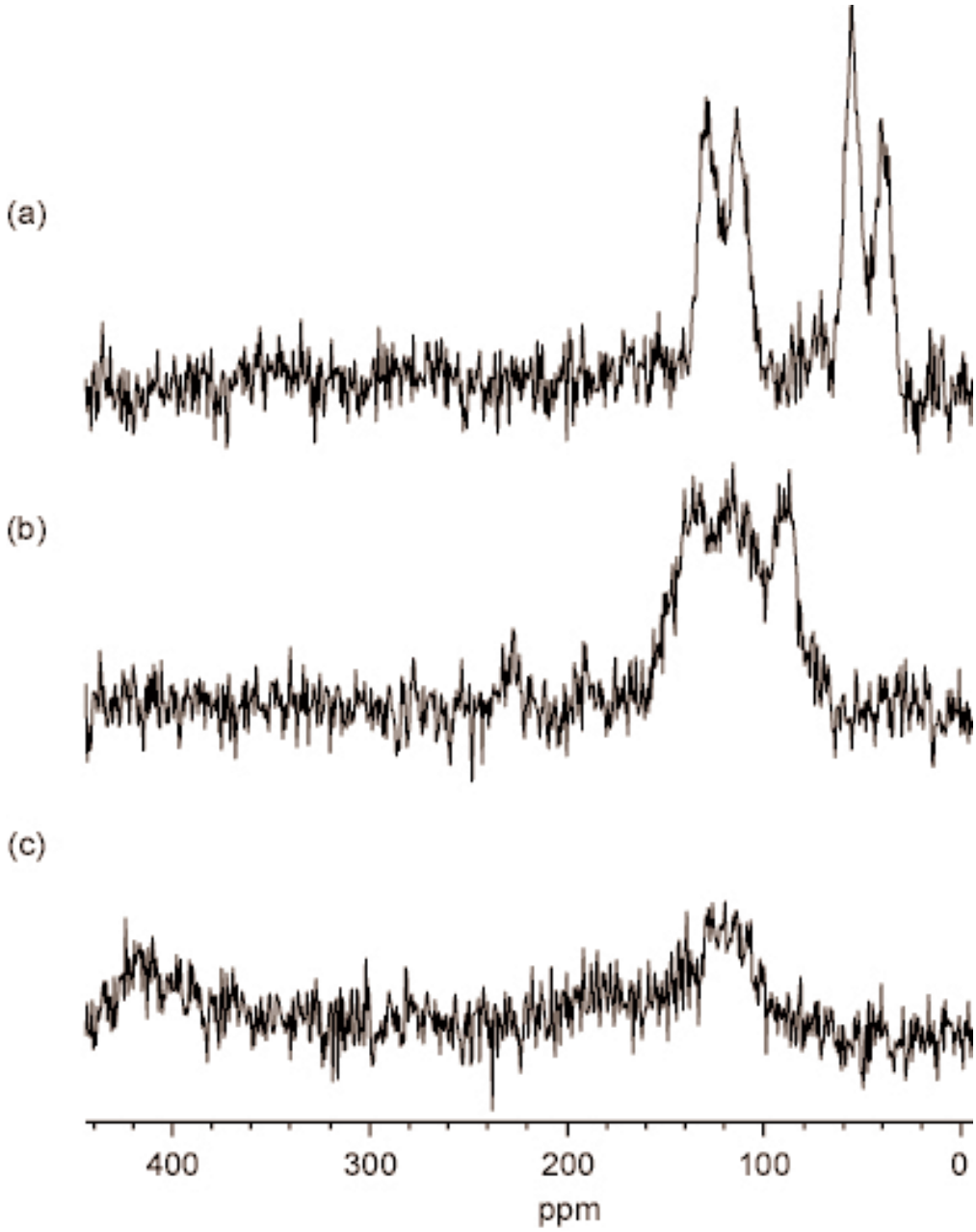

Figure 18: Cross-sections parallel to ω_2 taken from the refocused INADEQUATE spectrum of polymer CsC_{60} shown in Fig. 14 at ω_1 frequencies of (a) 168 ppm, (b) 228 ppm and (c) 534 ppm. Of these (a) and (c) arise from the connections between site (13) which is assigned to the resonance at 114 ppm in the MAS spectrum and sites (9) and (11) at 56 and 420 ppm respectively, while (b) shows an equivalence peak for site (13) at 114 ppm. Note the interference from peaks with similar ω_1 frequencies in (a) and (b).

With the assignment completed experimental Knight shift values can be extracted for each site on the fullerene molecule by estimating the chemical shift for all sites except (1) to be that of the ^{13}C resonance in C_{60}, namely 143 ppm. These values are shown in Table 2.

Electron density values calculated from

$$\rho(j) = \frac{K(j)}{\sum_j |K(j)|} \qquad \textbf{(2.3)}$$

are given for each site in Table 3. It should be noted that De Swiet *et al.* predicted sites 4, 5, 10, 11 and 14 to have the largest Knight shifts.[48]. Density functional calculations on a C_{60} trimer predict hyperfine couplings of 2.6, 2.6, 6.6, 6.6 and 6.8 MHz for these sites, respectively. Experimental Knight shifts and spin densities extracted from the spectrum are then in agreement with density functional calculations performed by de Swiet *et al.*[48] as it is shown in Table 4. In Figure 19 a C_{60} trimer is represented where sites with different hyperfine coupling are depicted with different colours.

It should also be noted that these calculations were carried out in the vacuum and do not include effects of packing in the solid which clearly break the symmetry between sites 10 and 11. Furthermore, note that a more detailed comparison between theory and experiment clearly requires a calculation that includes the effects of conduction between the polymer chain and the effect of the crystal field.

Peak	a	b	b*	c	d	d*	e	f	g	h	i
Position/ppm	420	378	375	227	133	114	88	68	56	41	35
K/ppm	277	235	232	84	-10	-29	-55	-75	-87	-102	0
Assignment	11	10	14	4,5	a	13	2	3	9	8	1

Table 2: Assignment, Positions and Experimental Knight Shifts for Resonances in the ^{13}C MAS spectrum of CsC_{60}

a. Peak d is assigned to sites 6, 7, 12, 15, 16

Site	1	2	3	4	5	6	7	8	9	10	11	12	13	14	15	16
K/ppm	0	-55	-75	84	84	-10	-10	-102	-87	235	277	-10	-29	232	-10	-10
ρ×100	0	-1.1	-1.4	1.6	1.6	-0.2	-0.2	-2.0	-1.7	4.5	5.3	-0.2	-0.6	4.5	-0.2	-0.2

Table 3: Experimental Knight Shifts and Electron Densities for Sites in CsC_{60}

Site	4,5	10,14	11
Hyperfine coupling (MHz)	2.2	6.6	6.8

Table 4: Hyperfine coupling calculated by Density functional calculations on a C_{60} trimer for some of the sites.

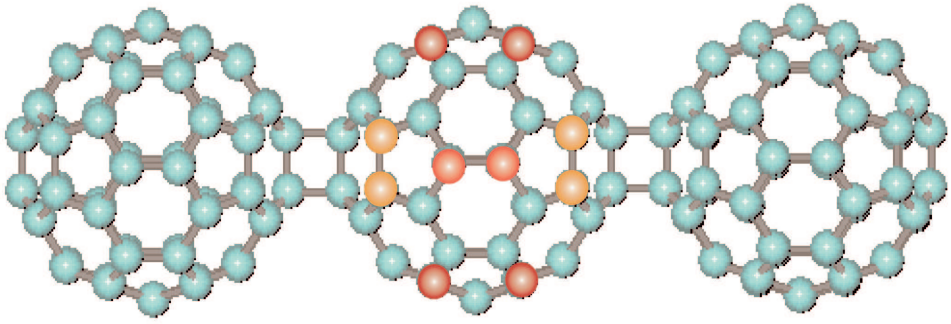

Figure 19: C_{60} trimer: sites with different hyperfine coupling are coloured differently. Note as the sites with larger hyperfine coupling and larger Knight Shift values (red) are around the "equator" of the C_{60} molecules.

2.4 Conclusions

An unambiguous assignment for the ^{13}C spectrum of CsC_{60} has been obtained using a refocused INADEQUATE experiment. In contrast to previous work the assignment does not rely on knowledge of the electronic structure of this material. Experimental Knight shifts and spin densities extracted from the spectrum are in agreement with density functional calculations performed by de Swiet *et al.*[48]. These in turn are based on models[47,52] in which the conduction electrons reside on sites around the equator of the fullerene molecule with insulating cycloaddition linkages between molecules. Hence the current data support a fully three-dimensional electronic structure for this material as opposed to a quasi one-dimensional one[35].

We demonstrated the experimental feasibility of the INADEQUATE experiment on an ^{13}C enriched sample of the polymeric phase of CsC_{60}, showing that INADEQUATE experiment leads to a sufficiently efficient excitation of double quantum coherence. Coherence transfer is exclusively mediated by the scalar J interactions, which leads to the unambiguous identification of through-bond connectivities.

The ^{13}C INADEQUATE spectra presented here show, for the first time in a solid, "remote" cross peaks between non-bonded pairs of nuclei which share a common coupling partner. These cross peaks are expected from a comparison with solution-state INADEQUATE at high levels of isotopic enrichment. In addition, new "equivalence" cross peaks, unique to solid-state INADEQUATE, have also been observed, and their origin explained.

3 Chain folding and morphology in long-chain *n*-alkanes

3.1 Introduction

It is important to understand the structure and motion of polymers, because of the manner in which they influence properties of practical interest. Several scientific techniques have been used to investigate them, and during the last 30-40 years solid-state NMR has featured prominently among these[59,60]. This effort has led to a better understanding of mechanical properties, but has also left many problems unsolved. Polyethylene (PE) has been widely investigated[61] because of its industrial interest and also because of the possibility of varying its morphology by different sample preparation procedures. Nevertheless, polydispersity has been a great hindrance to fundamental studies on crystallization and crystal morphology[62]. When different chain lengths are present in the sample, the extra chain lengths (cilia) from the longer chains have to be accommodated in an amorphous region. The structure of the resulting material is affected by polydispersity, and an ideal model compound should not have a wide distribution in the chain length.

Monodisperse polymers can be approximated by using narrow molecular weight fractions[63]. Monodisperse oligomers with a few tens of chain atoms have been synthesized chemically and studied for many years, most notably *n*-alkanes, the oligomers of PE[64,65,66], and more recently short oligomers of a number of aromatic polymers[67,68]. All these compounds have been investigated by several techniques[63], to answer some questions concerning the general structure of polymers. The issue of chain folding has been investigated

because changes in the chain folding can induce marked differences in structure and consequently in the overall performance and potential applications of polymers. For example, high molecular weight PE is a tough plastic solid because its chains are long enough to connect individual stems together within a lamellar crystallite by chain folding. The chains also wander between lamellae, connecting several of them together. These effects add strong covalent bond connections both within the lamellae and between them. On the other hand, only weak van der Waals forces hold the chains together in low molecular weight waxes, resulting in completely different properties[69].

There are several models to describe the morphology of semi-crystalline polymers, which differ mainly in the way in which the folding of the chain in the amorphous layer of the material is described. For this reason, it is very important, both for industrial applications[70] and for scientific interest[71], to know the nature of this fold. Despite all this, NMR has not been adopted very often to study chain folding. Only a few attempts have been carried out to correlate the NMR results with the chain folding. Schilling *et al.*[72] have explored the morphology of 1,4-*trans*-polybutadiene (TPBD) crystals by ^{13}C NMR spectroscopy using chemical methods. The crystals were suspended in toluene and reacted with *m*-chloroperbenzoic acid. It was expected that only the butadiene units in the fold surface would react completely and that the crystalline stems would not react at all. The results found in that work strongly favoured the model of a tight adjacent re-entry fold for TPBD lamellae grown from dilute heptane solution, but the method used to determine the fold and the crystalline stem lengths is only applicable to a system where the monomer units in the folds, the units in the stems, and the "junction" points between

folds and crystalline stems can be distinguished. Furthermore, it was assumed that only the butadiene units in the fold surface would react, the crystalline stems remaining impervious to the reagent.

We used solid-state NMR to study a long *n*-alkane $C_{246}H_{494}$, which can be made to crystallize in two forms. The chain folding in these was verified by X-ray scattering and Raman spectroscopy. We were able to observe differences in the NMR response for the two different forms. Furthermore, our NMR data allowed us to estimate the number of atoms involved in the fold.

As well as the chain folding, the motion of the chains exert a large influence on the properties of semi-crystalline polymers, such as PE[73]. For example, as crystallinity is increased, PE becomes less sensitive to wide variations of stiffness with temperature[74]. Chain diffusion is an important dynamic process in semi-crystalline polymers, determining, for example, their viscoelastic and transport properties[75]. Apart from general scientific interest in chain motion, chain diffusion is significant for the interpretation of longitudinal relaxation in ^{13}C NMR of semi-crystalline polymers.

The earliest investigations of the ^{13}C longitudinal relaxation in PE[76,77,78] assumed that the origin of the relaxation was a simple spin-lattice process. The initial part of the decay was observed to be non-exponential, which was attributed to a distribution of relaxation times[79] or the possibility of spin diffusion within the crystalline regions[80]. More recently, a series of longitudinal relaxation measurements in PE has been interpreted[81,82] as long distance solid-state chain diffusion between the amorphous and crystalline regions. According to Ref. 81, the relaxation in PE can be explained by chain diffusion only. In that paper, a Monte Carlo simulation of the diffusion of a

sample chain in a lamellar crystal was used to explain the recovery of ^{13}C magnetization after saturation. Nevertheless, Ref. 81 does not investigate the initial behaviour where the crystalline line grows in a way that cannot be justified by chain diffusion only.

The proposed mechanism for chain diffusion[83] was assigned to a chain jump process, first presented as a mechanism for the α relaxation observed by dynamic mechanical spectroscopy[84]. This relationship between the α process and longitudinal relaxation was already well established[85]. The α process is assigned to 180° jumps of the chain stems in the crystallites[86,87], like the helical jumps in other semi-crystalline polymers[88]. The motion effectively involves a rotation and a translation by one repeat unit, such that the portion of the chain in the crystallites is in its energetically most favourable position in the lattice before and after the jump. By increasing the temperature, there will be more parts of the chains that will have energy equal or larger than the activation energy for the α process, that is, chain diffusion is temperature activated.

In the next sections we investigate chain diffusion in PE and *n*-alkanes in order to give new insights into the relationship between chain diffusion and relaxation in semi-crystalline materials.

For a better understanding of the motion in PE and *n*-alkanes we performed other experiments on partially deuterated samples. To our knowledge, no studies on partially deuterated PE or *n*-alkanes are present in the literature. This is due to the difficulties with their preparation and to the fact that the important role played by the chain ends in the structure of the long *n*-alkanes has not been well recognized and understood[63]. The line shape in the ^{2}H

spectra are different from those for PE[105], because of the predominant role of the chain ends in this case. Hence, the experiments on partially deuterated *n*-alkanes in this thesis revealed important details of the structure and motion of PE, allowing models of motion for the chain ends in PE to be proposed.

The study of the long *n*-alkanes aids the understanding of the structure of PE, due to the fact that they are monodisperse. Problems rising from this approach are that in real polymers polydispersity can generate interactions between the chains that can alter the morphology. For this reason, we decided to investigate a mixture of deuterated *n*-alkanes in an attempt to link the gap between the pure model compounds and the real polydisperse polymers. Furthermore, deuterated *n*-alkanes can be used to study the nature of the amorphous layer and, particularly, the crystal-amorphous interphase. There have been only a few attempts in recent years in this direction. Small-angle x-ray scattering (SAXS) has been used to obtain the density correlation function across the lamellar stacks in semi-crystalline polymers[89,90], but the resulting structural information is of limited precision, due partly to poor positional order. Recently, Zeng and Ungar investigated a mixture of *n*-alkanes by different techniques[91] (SAXS, Raman spectroscopy). They proposed a new model where a triple layer super-lattice is found to be the structure of the low temperature phase of several binary solid solutions of very long chain *n*-alkanes with a chain length ratio between 1.3 and 1.7 and a chain length difference up to 100 carbon nuclei. One full repeat unit of the super-lattice structure contains three crystalline layers; the two outer ones contain both long and short molecules, while the middle layer contains the extended tails of the long molecules protruding from the two outer layers.

We investigated by solid-state NMR the same mixture studied in Ref. 91 and the results obtained complement the previous findings of Zeng and Ungar, although some new details of the structure and the crystallinity of such material are revealed.

3.2 Materials and Methods

3.2.1 Polyethylene and *n*-alkanes

To study the structure of semi-crystalline polymers we performed a simple single pulse experiment according to Figure 20. The curves for Ultra High Molecular Weight Polyethylene (UHMWPE) resulting from plotting the intensity of the signal versus the time τ_D are shown in Figure 21. There is an unexpected maximum at about 2 s on the relaxation curve for the peak at 29.5 ppm. A way to understand what is happening is to perform another experiment where the ^{13}C magnetization is pre-saturated with a series of 90^o pulses as shown in Figure 22. In this case, in order to produce the relaxation curves, the time τ_D is kept constant while τ_1 is varied and the intensity of the signal is plotted against τ_1.

Using the pulse sequence shown in Figure 22 with a τ_D of only 0.3 s we obtained saturation-recovery curves that are analogous to the one showed in Figure 21, where the maximum at 2 s is still present for the amorphous peak. A substantial change occurs when using longer τ_D values, as summarized in Figure 23 where three different experiments have been performed with different τ_D values at the constant temperature of 60^oC.

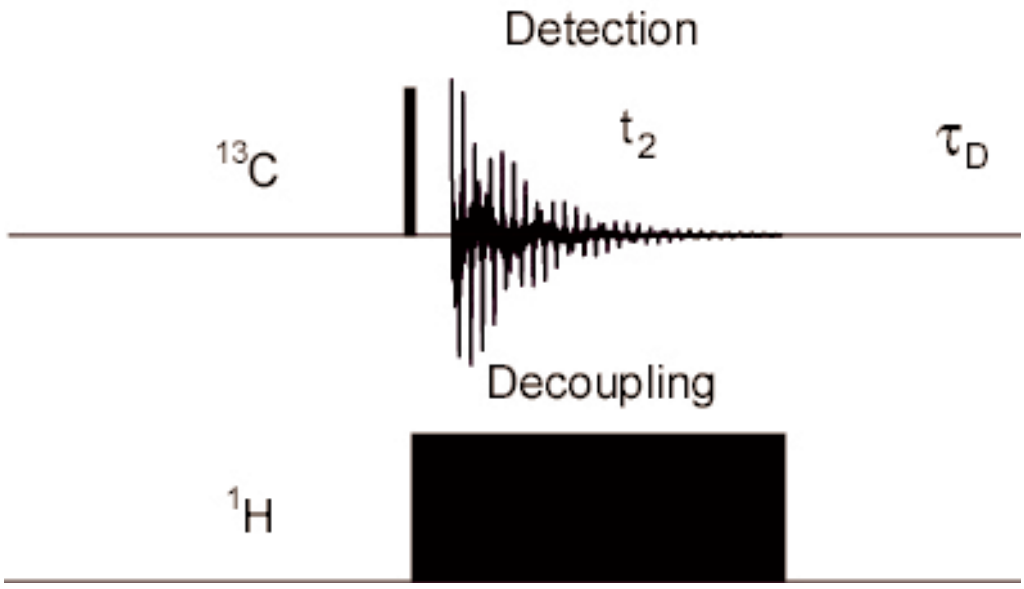

Figure 20: Pulse sequence for the single pulse decoupling experiment. Note the decoupling is on during the acquisition time and the time τ_D is varied in order to obtain the relaxation curve.

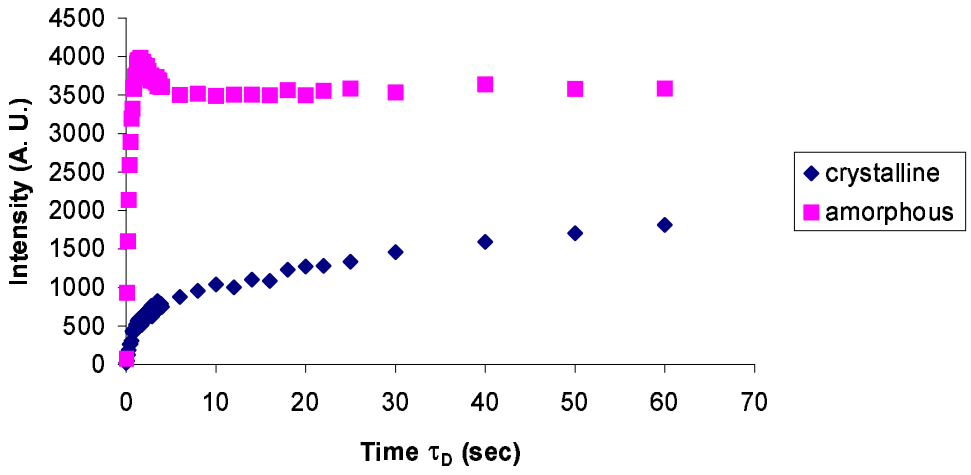

Figure 21: Relaxation curves of the crystalline (31.4 ppm, squares) and amorphous (29.5 ppm, diamonds) peaks at 60°C for UHMWPE. Note the maximum at about 2 s in the amorphous relaxation curve.

To explain our results we have to consider the fact that during the acquisition time in the single pulse decoupling experiment (Figure 20) the protons are saturated and so there is a transient nuclear Overhauser enhancement (nOe) of the ^{13}C signal as explained in section 1.1.4. When the pulse sequence described in Figure 22 is applied using a short τ_D, the nOe is still present as the protons are not fully relaxed at the beginning of the acquisition time for short values of τ_1. The nOe at low τ_1 values decreases with longer τ_D, and only disappears for values of relaxation time as long as 15 s (Figure 23 (c)) when the saturation-recovery curve of the amorphous peak will show the normal trend with no maximum. Although the final values of intensity measured in the two different cases (short and long τ_D) are the same, the build up of the signal at the beginning is substantially different, and neglecting the presence of nOe could gravely affect the modelling of the experimental results. Note that even the crystalline peak is enhanced by using a short τ_D and this strongly indicates that the origin for the longitudinal relaxation is similar for both phases.

The crystallinity of the sample was calculated experimentally by performing wide line ^1H NMR experiments. A standard 90_x-τ-90_y solid-echo pulse sequence was used, with inter-pulse spacing, τ, varying between 7 and 14 μs. The broad component of the spectrum (representing the crystalline phase) obtained at each value of τ was fitted to a Gaussian function. The intensities of all the Gaussian functions so found was plotted as a function of τ and the curve obtained was fitted to another Gaussian function and this was extrapolated back to zero to obtain the crystallinity, which was calculated to

be 61% at room temperature and 57% at 60°C. The data to obtain the crystallinity at room temperature are shown in Figure 24.

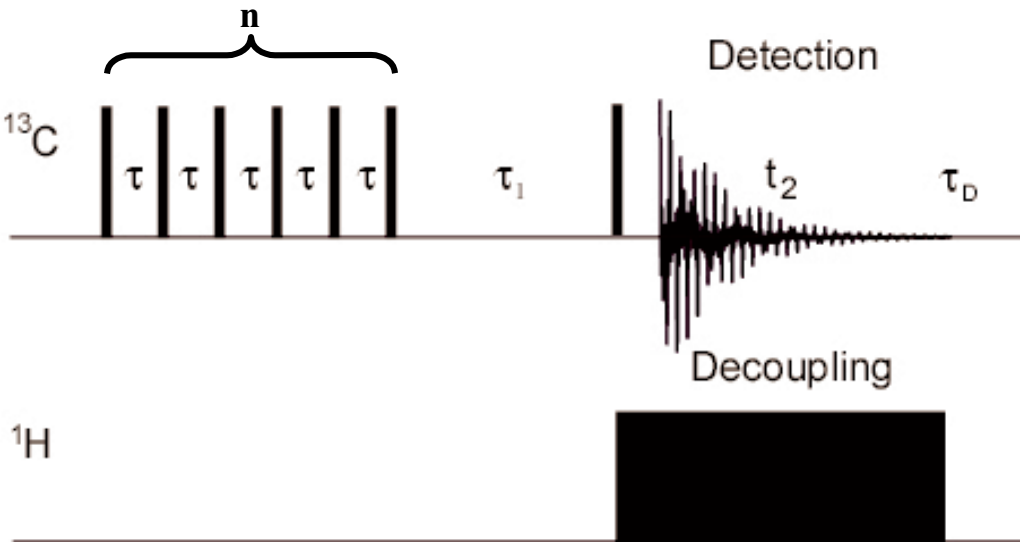

Figure 22: Saturation-recovery pulse sequence developed to measure the ^{13}C longitudinal relaxation. Presaturation was performed on the ^{13}C channel by applying several 90° pulses (n=20) with an interval τ of 3 ms between them. The time τ_1 is varied to obtain the relaxation curve. Different results are found using different τ_D time as explained in the text.

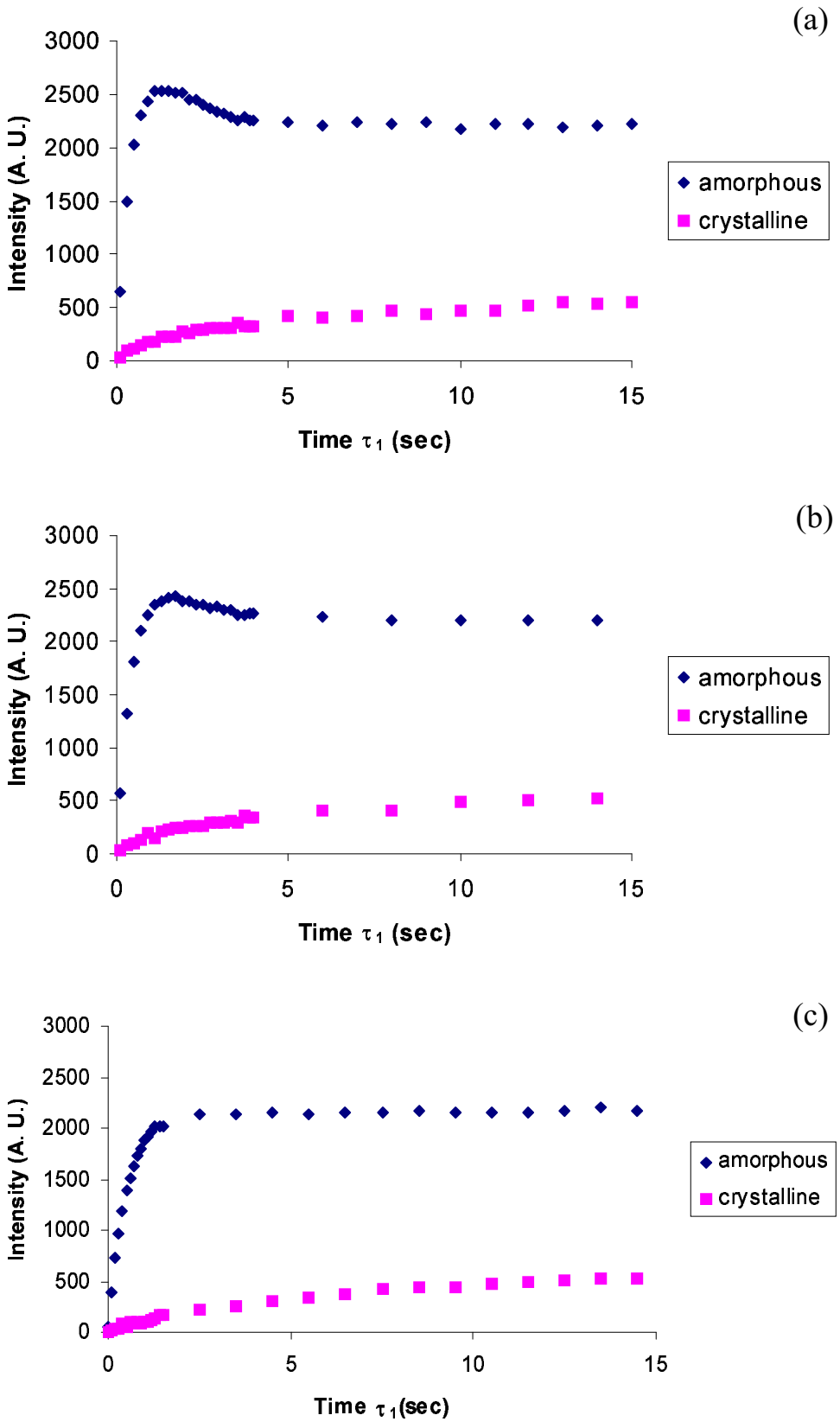

Figure 23: Relaxation curves for UHMWPE at room temperature obtained plotting intensity versus τ_1 using the pulse sequence shown in Figure 22, keeping τ_D constant. Different τ_D values were used for the three experiments: (a) τ_D = 0.3 s; (b) τ_D = 0.8 s; (c) τ_D = 15 s.

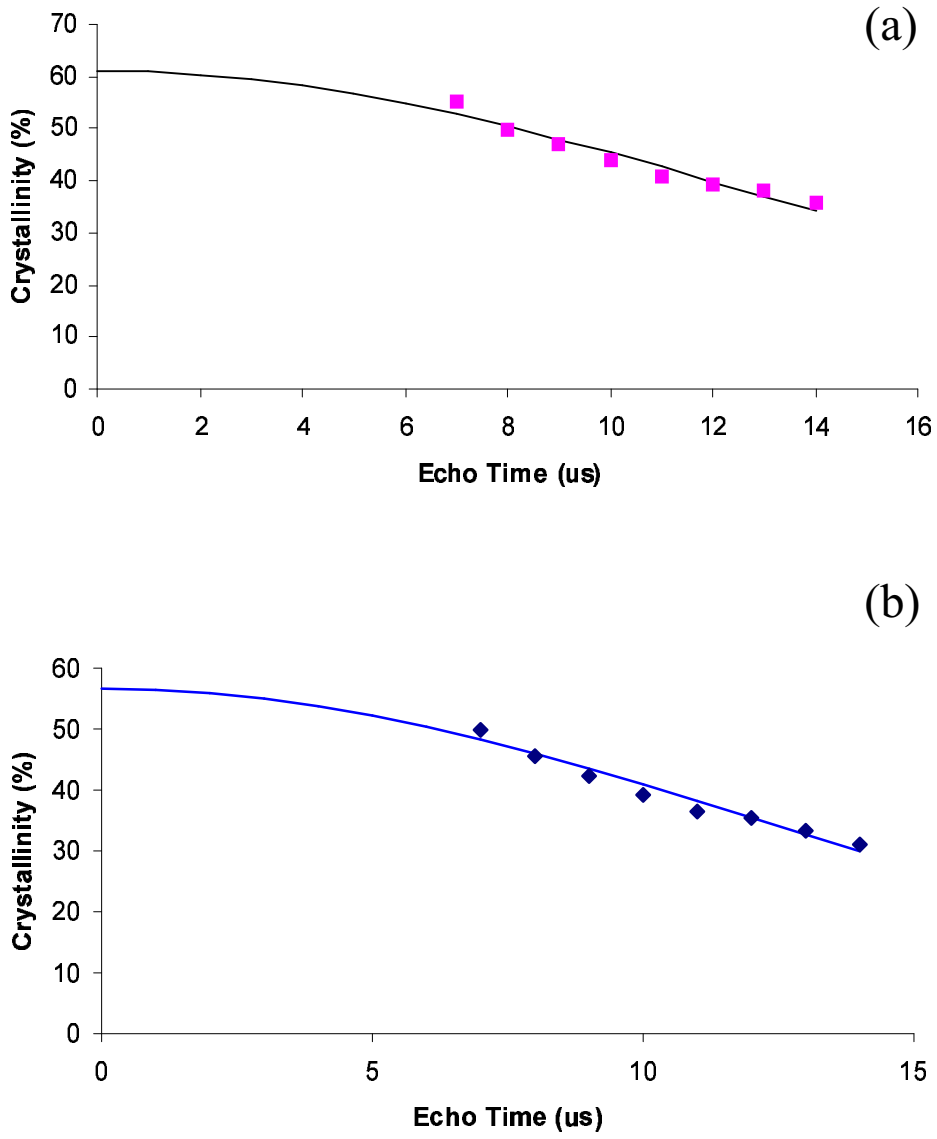

Figure 24: Crystallinity for UHMWPE at T = 20°C (a) and T = 60°C (b) calculated by the solid-echo experiment as described in the text.

The next samples studied in our laboratory were *n*-alkanes corresponding to the formula $C_{246}H_{494}$. The pure long chain *n*-alkanes were kindly provided by Drs G. M. Brooke and S. Mohammed, University of Durham. For details of synthesis see Ref. 92. It has already been shown in the literature[93] that it is possible to prepare from the same *n*-alkane both the once folded (OF) and the extended (E) form, depending on the rate of cooling the sample from the melt,

the OF form being kinetically more favoured (fast cooling rate) and the E form thermodynamically more stable (slow cooling rate), as crystals comprising folded chains are more likely to be formed the greater the super cooling[94]. The extent of super cooling is defined as $T_m - T_c$, where T_m is the melting temperature and T_c the crystallization temperature. Although the extended chain crystal is the one of maximum stability, the probability of chains extending themselves fully in primary nucleation is low at large super cooling. Chain-folded fluctuations that involve lower free energy barriers are preferred. Even if an extended chain substrate is available, the folded chain crystal growth is still greater due to the large number of possible folded molecular conformations and the large number of possible attachment positions along the extended chain sites.

Accordingly, to prepare bulk samples of *n*-alkane exclusively comprising OF crystals, the samples were quenched to a large super cooling from the melting point for crystallization. The rate of super cooling is crucial for obtaining samples that are exactly OF instead of randomly folded. In our case, it was made sure that the cooling rate from the melt (T_m = 128.6°C) was exactly 3°C/minute and that the sample was annealed at T = 90°C for at least 8 hours. In order to obtain the E form we cooled the sample from the melt at 0.2°C/minute until 120°C and then we annealed the sample for 8 hours. Both samples were then finally brought to room temperature with a cooling rate of 1°C/minute.

Applying these two different procedures, samples of both forms were prepared, and the structure was confirmed by DSC[95,96], X-ray diffraction[95] and by visual (optical microscopic) observation of individual crystals. The two

different samples have been successively investigated by solid-state NMR as it will be described in section 3.3.2.

3.2.2 Deuterated samples

As discussed in section 3.1, for a better understanding of the motion for the inter-lamellae part, we decided then to investigate different deuterated compounds. A long chain *n*-alkane having a deuterated chain end and corresponding to the formula $C_{12}H_{25}(CH_2)_{192}CHDC_{11}D_{23}$ ($C_{216}H_{434}$-d_{24}) was studied as well as a mixture of *n*-alkanes corresponds to the formula ($C_{12}H_{25}(CH_2)_{192}CHDC_{11}D_{23}$+ $C_{162}H_{326}$) ("the mixture"). The samples, kindly provided by Drs G. M. Brooke and S. Mohammed, University of Durham, were crystallized from toluene solution and the crystals have chains perpendicular to the lamellar surface[93]. $C_{216}H_{434}$-d_{24} has been prepared to be in the extended (E) form, having been cooled down slowly, according to the procedure described above, while the mixture has been obtained simply adding to $C_{216}H_{434}$-d_{24} the non-deuterated long *n*-alkane ($C_{162}H_{326}$)[97]. This latter compound changes drastically the structure of the crystal, as it will be revealed by our NMR studies (3.3.4).

In sections 3.3.3-3.3.4 it will be shown that to simulate the line shape obtained experimentally from the ^2H NMR spectra, two particularly simple motional mechanisms for long chain molecules have been used, the "crankshaft" 5-bond motion[98,99] and the rotation of the methyl group[100]. The simulation has been done using the method proposed by Heaton[101], calculating the evolution of transverse magnetization **M** following a sequence of radio frequency pulses as it is described by the stochastic Liouville equation,

$$\frac{d\mathbf{M}(t)}{dt} = [i\mathbf{\Omega} + \mathbf{W}]\mathbf{M}(t) = \mathbf{A}\mathbf{M}(t)$$

The components of **M** represent the complex transverse magnetization for each of the nM sites, defined by a particular orientation and/or conformation. The matrix operator **Ω** is governed by the secular part of the spin Hamiltonian and is diagonal with elements ω_i, which are the precession frequencies of the spins at the different sites *i*. Dynamic processes are described explicitly by the exchange operator **W**. Each off-diagonal element W_{ij} represents the rate of transfer of population from site *j* to site *i*, and is governed by the model used to describe the molecular dynamics.

The relaxation function **M**(t) may be evaluated if we consider only times t which are integral multiples of δ, times short enough so that **Ω** and **W** approximately commute,

$\exp(\mathbf{A}\delta) \approx \exp(i\mathbf{\Omega}\delta)\exp(\mathbf{W}\delta)$.

In this particular case, we can write:

$\mathbf{M}(t) = \mathbf{M}(n\delta) = \mathbf{s}_n(\delta)\,\mathbf{M}(0)$,

$\mathbf{s}(\delta) = \exp(i\mathbf{\Omega}\delta/2)\,\mathbf{p}(\delta)\exp(i\mathbf{\Omega}\delta/2)$,

Choosing δ as long as possible in order to provide a good approximation to the true magnetization evolution. The elements of *p(t)*, obtained by solving the corresponding master equation[102], are:

$$[p(t)]_{ij} = \sum_k u_{ik} u_{jk} \exp(\lambda_k t),$$

where u_{ik} are elements of the eigenvector matrix of the exchange operator **W** and λ_k are the corresponding eigenvalues. Explicit forms for the matrix elements of the exchange operator for jump motion and rotational diffusion

are given elsewhere[103,104]. For a jump motion model that involves n sites the values $[p(t)]_{ij}$ can be calculated as:

$$[p(t)]_{ij} = \frac{1 + (n-1)\exp\left(\frac{-n\Delta}{2\tau_c}\right)}{n} \qquad \text{for } i = j$$

$$[p(t)]_{ij} = \frac{1 - \exp\left(\frac{-n\Delta}{2\tau_c}\right)}{n} \qquad \text{for } i \neq j$$

where τ_c is the correlation time and it is linked to the exchange rate k by:

$k = 1/2\tau_c$

3.2.3 Experimental set-up

All the experiments featured in section 3 were acquired on a Varian Chemagnetics Infinity spectrometer operating at a proton Larmor frequency of 300 MHz.

A Varian Chemagnetics MAS probe with a maximum spinning speed of 7 kHz, holding a 7 mm rotor was used for all the ^{13}C and proton spectra, while a Varian Chemagnetics static probe was used for all the experiments on the deuterated samples.

3.2.3.1 Undistorted deuteron line shapes: SOLID ECHO

Since deuteron spectra of solids are extremely broad, covering a frequency range of about 250 kHz, undistorted spectra are difficult to obtain[105]. The rapid decay of magnetization following the application of an r.f. pulse precludes the

use of standard FT methods since a significant part of the signal is lost in the inevitable dead-time of the receiver. This rapid decay of magnetization, on a timescale of the order of the inverse width of the spectrum (δ^{-1}), i.e. a few μs, results from destructive interference of the different spectral components. By applying a second pulse, in quadrature with the first one, the magnetization can, however, be refocused, leading to the formation of a solid echo[106]. By taking the FT of the data starting at the echo maximum, undistorted absorption spectra may be obtained[107,108]. In absence of motion the formation of the solid echo is limited by T_2^* only, in presence of motion, however, the NMR frequencies in the periods of destructive interference and constructive refocusing, respectively, may be different. This not only leads to a reduction of the echo amplitude, but also causes characteristic signal changes[109]. This can be exploited to extend the dynamic range of line shape studies by using deliberately long delay times τ_1 and the signal intensity can provide additional information about different types of motion. The solid echo pulse sequence is schematically depicted in Figure 25. Of course, the system must be broadband over a spectral range of approximately 300 kHz. This is relatively easy to achieve for the receiver, much less so for the transmitter. The spectral density $F(\omega)$ of a rectangular pulse of amplitude B_1, duration $2t_p$ centered about ω_0 is given by[110]:

$$F(\omega) = t_p B_1 \frac{\sin \Delta\omega t_p}{\Delta\omega t_p}, \qquad \Delta\omega = (\omega - \omega_0).$$

For ^{2}H powder spectra $\Delta\omega \leq 130$ kHz. If one wants to obtain the undistorted powder spectrum directly one must require that $F(\omega)$ at the outer edges of the spectrum differ from $F(\omega_0)$, the value at the centre, by no more than 5%[110].

Therefore one must use pulses of duration no more than 1.35 μs. In order for these to be π/2 pulses one must achieve $B_1 \geq 280$ G in a broadband probe! In practice it turns out not to be essential to meet these requirements fully. By choosing 45° pulses for the solid echo sequence the pulse length of 1.55 μs was sufficiently short to obtain solid-state ^{2}H spectra that were not distorted. The spectra did not change significantly when the sin *x/x* correction suggested by Hentschel *et al.*[105] was applied. To obtain spectra that are symmetric around the centre frequency we found that the tuning of the probe was essential so that the latter was adjusted until we obtained perfectly symmetric spectra.

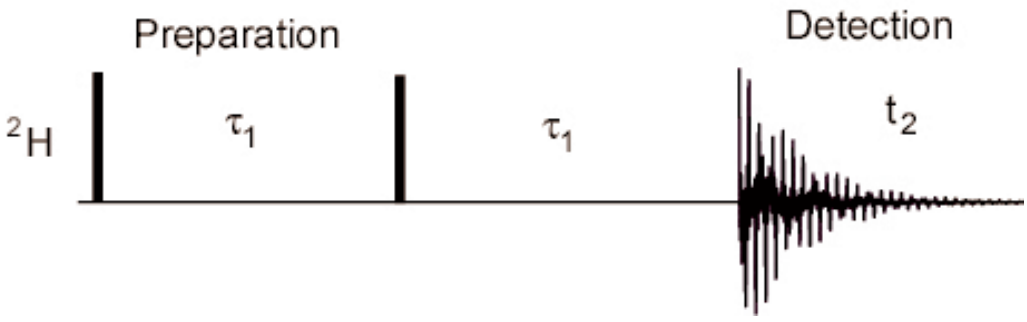

Figure 25: Solid echo pulse sequence. The black rectangles represent 90° pulses

In order to get the relaxation times for the different portions of the deuterated samples, we performed the saturation-recovery experiment. The pulse sequence starts with five 90° pulses separated by ~ 2 ms during which the nuclear magnetization is saturated. A waiting time τ_0 is applied prior to the application of the solid echo sequence. This pulse sequence, identical to the one shown in Figure 22 apart from the echo pulse, is shown in Figure 26.

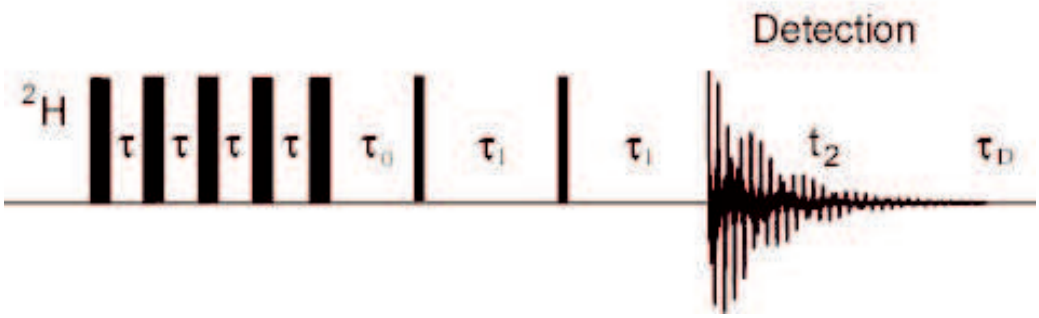

Figure 26: pulse sequence for the Saturation-Recovery experiment. The time τ was 2 ms, τ_1 was 100 μs and τ_0 was varied from 1 s up to 30 s. The τ_D used was 1 s. The pulses before τ_0 are 90° while after τ_0 45° pulses are applied for the reason explained in section 3.2.3.1.

3.3 Results and discussion

3.3.1 Ultra High Molecular Weight Polyethylene (UHMWPE)

The first sample studied in our laboratory was Ultra High Molecular Weight Polyethylene (UHMWPE). Although performing solid-state NMR experiments on this sort of samples is not something completely new, we found in the literature different interpretations[81,82] of some important issues for this sample such as the ^{13}C longitudinal relaxation and the possibility to relate it to the structure.

Furthermore, the results that we obtained for UHMWPE could be used to test our models and simulations, so that we can compare the differences in structure between long polymers like UHMWPE and the long-chain *n*-alkanes, highlighting the similarities and/or peculiarities.

First of all let us consider the spectrum of UHMWPE recorded using the standard single pulse experiment where we decouple the protons during the acquisition time (Figure 27). Using a relaxation time of 13 s allows us to observe two clearly separated peaks at about 29.5 and 31.4 ppm, although the latter is only partially relaxed. For aliphatic molecules, it is well known that the change of a carbon-carbon bond conformation from trans to gauche results in a significant up-field shift for the resonances of neighbouring carbons. These conformational shift variations, denoted as the γ-gauche and vicinal-gauche effects, can be observed for solution as well as for solid-state MAS NMR spectra[111].

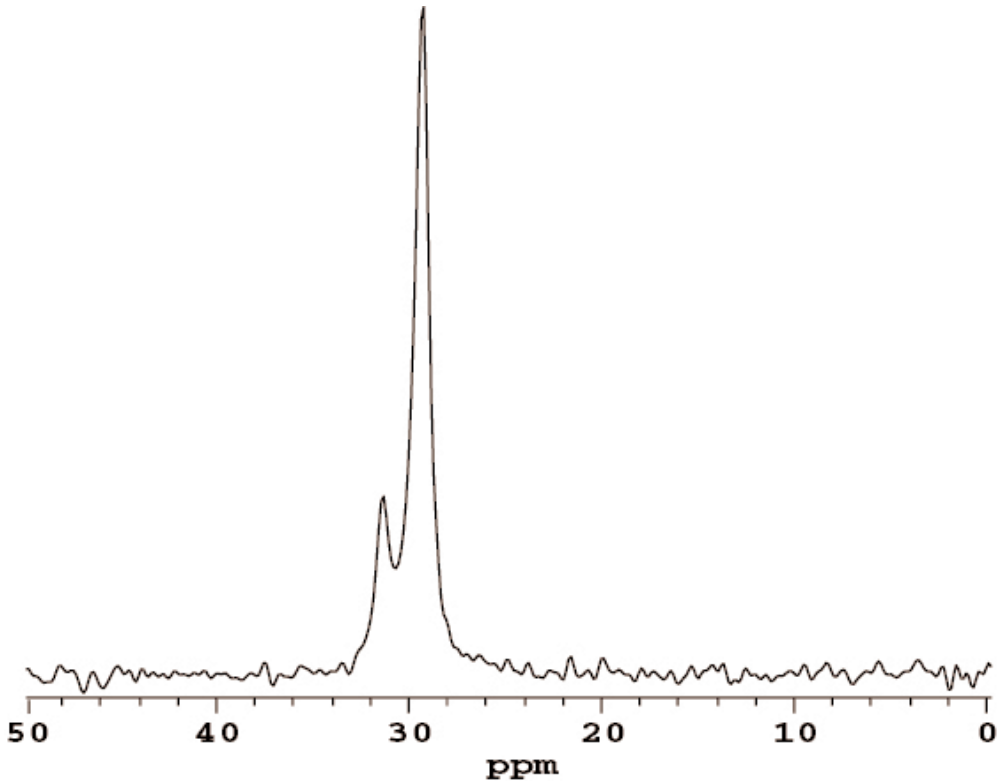

Figure 27: ^{13}C 1D spectrum of UHMWPE acquired with a relaxation delay of 13 s, acquisition time of 25.6 ms and a spectral width of 20 kHz. The sample was spinning at 4 kHz.

The relatively narrow peak at 31.4 ppm corresponds to carbon atoms in regions where the chains adopt an all-trans conformation ("crystalline phase"), while the peak at 29.5 ppm arises from inner carbon atoms in regions where there are some gauche carbon bonds ("amorphous phase"). The relaxation delay of 13 s was chosen so that the all-trans peak is partially saturated.

Since simple examination of the 1D spectrum does not provide further information, we decided to study the recovery of ^{13}C magnetization after saturation for UHMWPE at different temperatures, in order to build a model of relaxation that can simulate the experimental data of Figure 29. As discussed in the introductory section (3.1) the chain diffusion has to be the main factor responsible for the recovery of the magnetization. Nevertheless,

accurate fits cannot be produced by chain diffusion only, as at short time the recovery of the magnetization gives rise to a steep slope. Analogously, the introduction of spin diffusion in the model does not reproduce the curvature requested by the experimental data at short relaxation time. In Figure 28 two different attempts to simulate the data using only chain diffusion and spin diffusion are shown.

We then introduced in the model a rapid T_1 relaxation process for a small part of the crystalline regions. The origin of this T_1 is typically associated with relaxation in a particular area of the crystalline regions called the interphase[82]. This seems quite reasonable, as it is very unlikely that the boundaries between the amorphous and the crystalline phase are as small as one or two ^{13}C nuclei. A much more realistic model predicts that the transition in phase involves at least 9% of the crystalline regions[112]. Experimental evidence for the presence of such an interphase are reported in literature, and a model where an interphase region on the surface of the crystallites besides the two crystalline and amorphous phases is present, has been often proposed as a consequence of the higher configurational constraint of the units adjacent to the crystalline region in comparison to the chains in the pure amorphous domain[113]. Experimental studies such as broad-line ^{1}H NMR[114,115,116,117], high-resolution solid-state ^{13}C NMR[113,118,119], Raman spectroscopy[120,121], small-angle X-ray[122] and neutron scattering among others clearly demonstrate the presence of an appreciable interfacial region that is characterized by the partial ordering of the chain units.

Fits to the experimental values in Figure 29 were produced by means of a Monte Carlo simulation of the diffusion of a sample in a lamellar crystal

where an interphase between the amorphous and the crystalline parts was introduced. This model chain consists of 100 crystalline stems, each 250 repeat units long, 99 amorphous loops (plus two chain ends) whose length was adjusted to match the crystallinity. The interphase consisted of 26 nuclei (≅10% of the crystalline phase) that although contributing to the crystalline signal, were made able to relax through a normal relaxation process with a T_1 ≅ 6 s.

The ^{13}C nuclei that are in the amorphous regions were allowed to relax with relaxation time constant (T_1) obtained from the experimental curves of the amorphous part (T_{1a} ≅ 0.5 s). With every jump of a crystalline stem, the lengths of two adjacent loops are increased and decreased, respectively, by one repeat unit. As a result of successive diffusion steps, all parts of the chain slowly move away from their initial positions, while the loop lengths fluctuate. The jumps have a finite probability of success, and a random number generator is used to determine whether a particular jump is successful. The probability can be translated directly into a jump rate and therefore will vary at different temperatures. After each diffusion step only the nuclei in the amorphous and in the interphase portions are allowed to relax. The relaxation step is also implemented statistically using a random number generator with the probability of relaxation in the amorphous phase set to be greater than that in the interphase. The experimental data were fitted very well using the modified diffusion model so described, where the jump rate was increased at higher temperatures as described in Figure 29.

This model fits the data of UHMWPE in a very satisfactory way. So far it has been an open question as to whether the diffusion is hindered by

entanglements, tight re-entries, and similar constraints of the chain loops in the amorphous domains. The rate of the diffusion process found in our simulation suggests that although the molecules show a fast diffusion rate (100 jumps/s at 60^{o}C), this is considerably smaller than the one expected for free diffusion at this temperature[81] (1000 jumps/s), that is the process is slowed down by constraints of the chain loops in the amorphous domains. The values of the diffusion rate at different temperatures found in our simulations allowed us to estimate the activation energy for the α process, E_a = 105 ± 10 kJ/mol. This result fits very well with literature values[123] of 104-116 kJ/mol for the α relaxation in PE.

Our model is also the only sensible one that can fit the analogous data for the long chain *n*-alkane ($C_{246}H_{494}$) as it is shown in the next paragraph. In that case the chain diffusion seems still to be the main driving force for the relaxation of the crystalline part although it cannot explain the experimental data in the whole range of time alone. Again the introduction of an interphase allows us to simulate coherently all the experimental data.

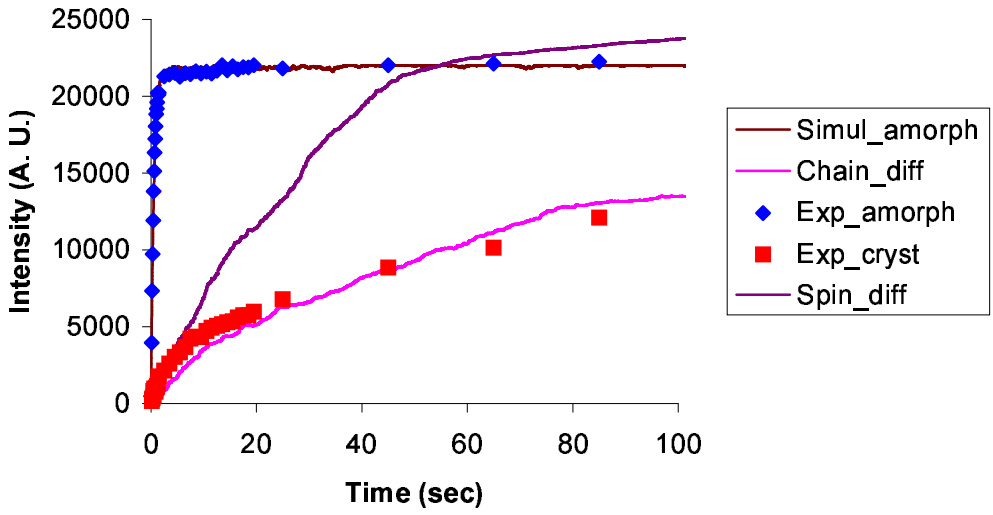

Figure 28: Simulation of the recovery of the magnetization for UHMWPE at 60°C using different models. As an example, two of the different attempts of simulation based only on chain and spin diffusion are shown. If the experimental data at short relaxation time (<30 s) are simulated, the rest of the simulated curve diverges from the experimental data at longer time, being the predicted recovery of magnetization too rapid for the crystalline part. Vice versa, trying to fit the data at longer time gives rise to large discrepancy between the calculated curve and the experimental data at short time.

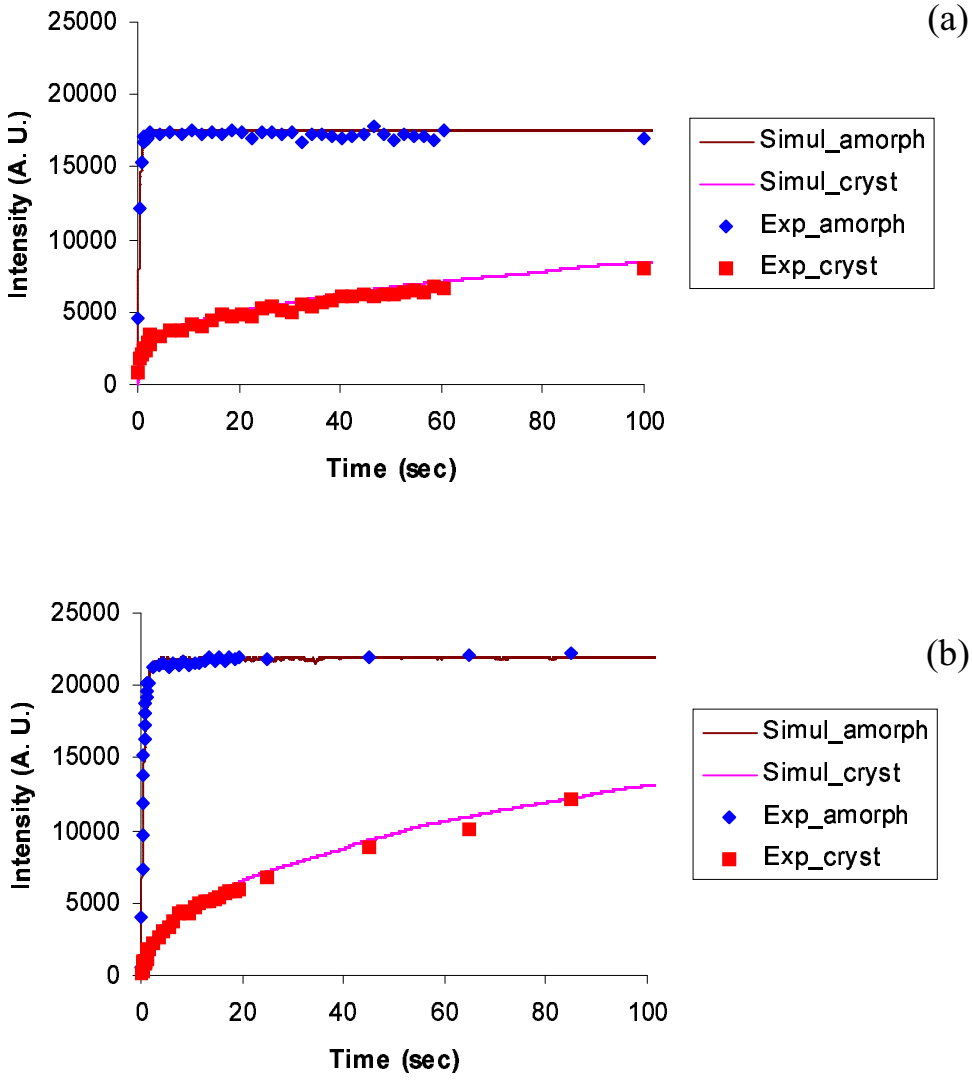

Figure 29: Simulation of the recovery of the magnetization for UHMWPE at 20°C (a) and 60°C (b) using the chain diffusion model where the presence of an interphase was introduced. In this case the simulated curve fits the experimental data in the whole range of relaxation time. The chain diffusion increases with temperatures as expected so that the optimal jump rate that better fits the experimental data was ≅10 jumps/s at 20°C (a) and ≅100 jumps/s at 60°C (b). Note also that the amorphous part increases at high temperatures (b) and that the recover of the crystalline magnetization is visibly quicker.

3.3.2 n-Alkanes

We performed ^{13}C MAS single pulse experiments at a Larmor frequency of 75.45 MHz on approximately 100 mg of $C_{246}H_{494}$ in both the once-folded (OF) and extended (E) forms packed into a 7.5 mm MAS rotor spinning at 3 kHz at room temperature. The MAS rate was chosen to ensure that spinning sidebands were not overlapping with the main peaks. The spectra obtained from the two samples are shown in Figure 30. It is possible to assign the different peaks to different parts of the chain by comparison with the literature for shorter *n*-alkanes[65], so we have been able to assign the main peaks at about 31.4 ppm and 29.5 ppm to the -**C**H_2- of the chain. The other peaks are due to carbon atoms in the chain ends, such as -**C**H_3 (13.4 ppm), -**C**H_2CH_3 (23.3 ppm), -**C**$H_2CH_2CH_3$ (32.8 ppm). Lots of important results can be inferred from the two spectra in Figure 30. First of all, for both samples, because of the presence of the peak at 29.5 ppm, is obvious that part of the chain is in the amorphous phase, where some carbon nuclei have gauche-gauche conformations and experience a large mobility. This result is in agreement with all the previous studies done on these kinds of compounds that have shown a lamellar structure where crystalline regions alternate with amorphous ones[124]. Nevertheless, in contrast to all the previous studies, from these samples we can obtain some quantitative information on the amount of material contained in each phase. In contrast to UHMWPE, where there was no signal from the ends of the chains, from these samples we are able to observe peaks that correspond to the methyl and the last methylene group. For τ_D as long as 15 s, the signals from the chain ends, as well as the amorphous peak, are fully relaxed. Hence, the amount of amorphous material can be

quantified by normalizing with respect to the methyl intensity. The complete list of results obtained is shown in Table 5, where N_a is the number of nuclei in the amorphous phase.

	OF (20°C)	OF (60°C)	E (20°C)	E (60°C)
N_a	7±1	9±1	2±1	3±1

Table 5: Number of carbon nuclei in the amorphous part (N_a) for OF and E at different temperatures calculated as explained in the text.

In order to gain more information about the structure and the motion of this sample, we performed the same experiment as described previously for UHMWPE, using the pulse sequence of Figure 22 and varying the time τ_1. The results are shown in Figure 31. As in UHMWPE, the main peak at 31.4 ppm due to the crystalline -**C**H_2- has a very long relaxation time (T_1), while all the other peaks have very short T_1.

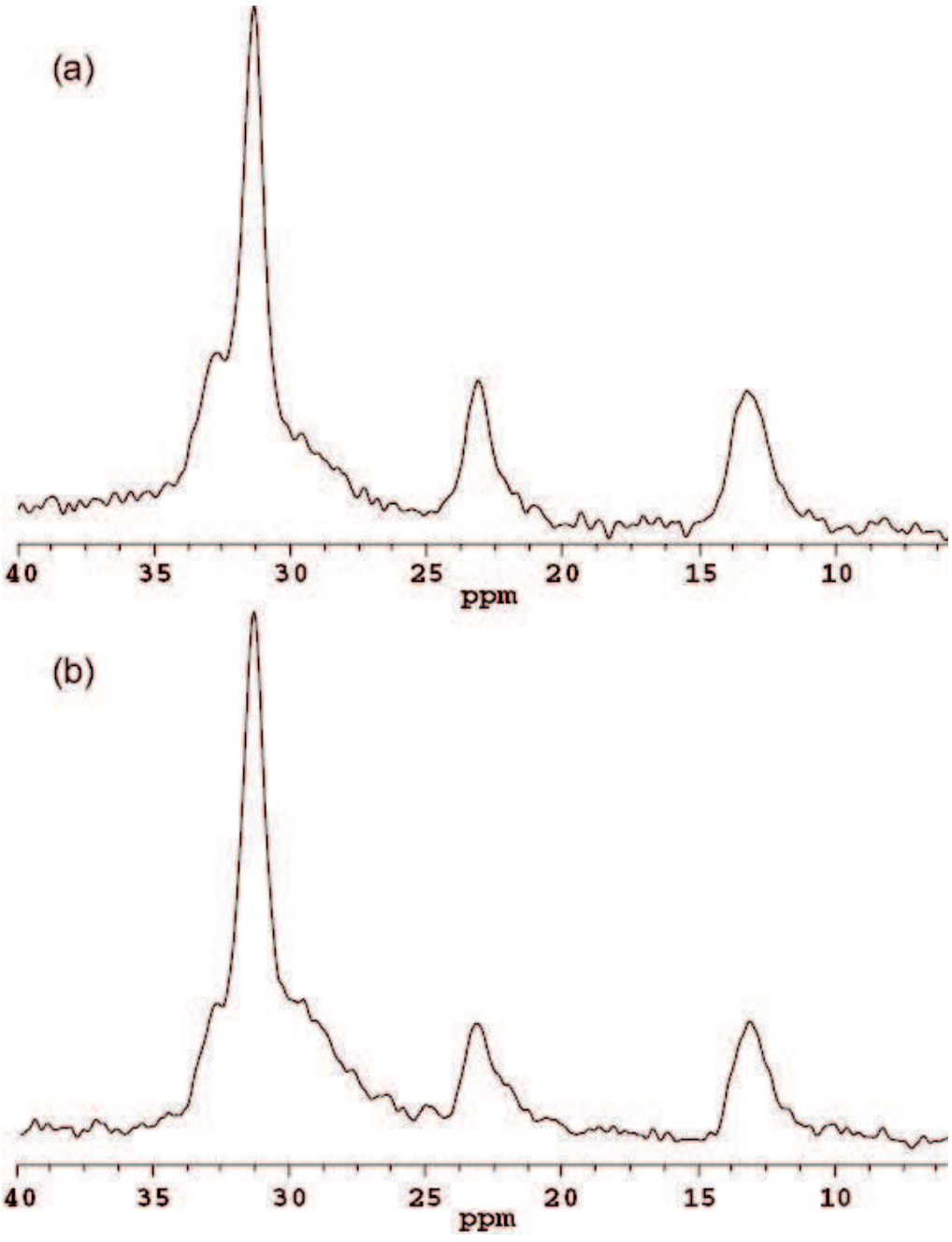

Figure 30: ^{13}C 1D spectrum for OF (a) and E (b) at room temperature. The full spectral width was 15 kHz, the Proton decoupling was on during an acquisition time of 34.12 ms and a relaxation delay (τ_D) of 15 s was inserted between scans. Note that in (b) the signal coming from the chain ends is more intense due to the smaller scaling factor of the crystalline peak.

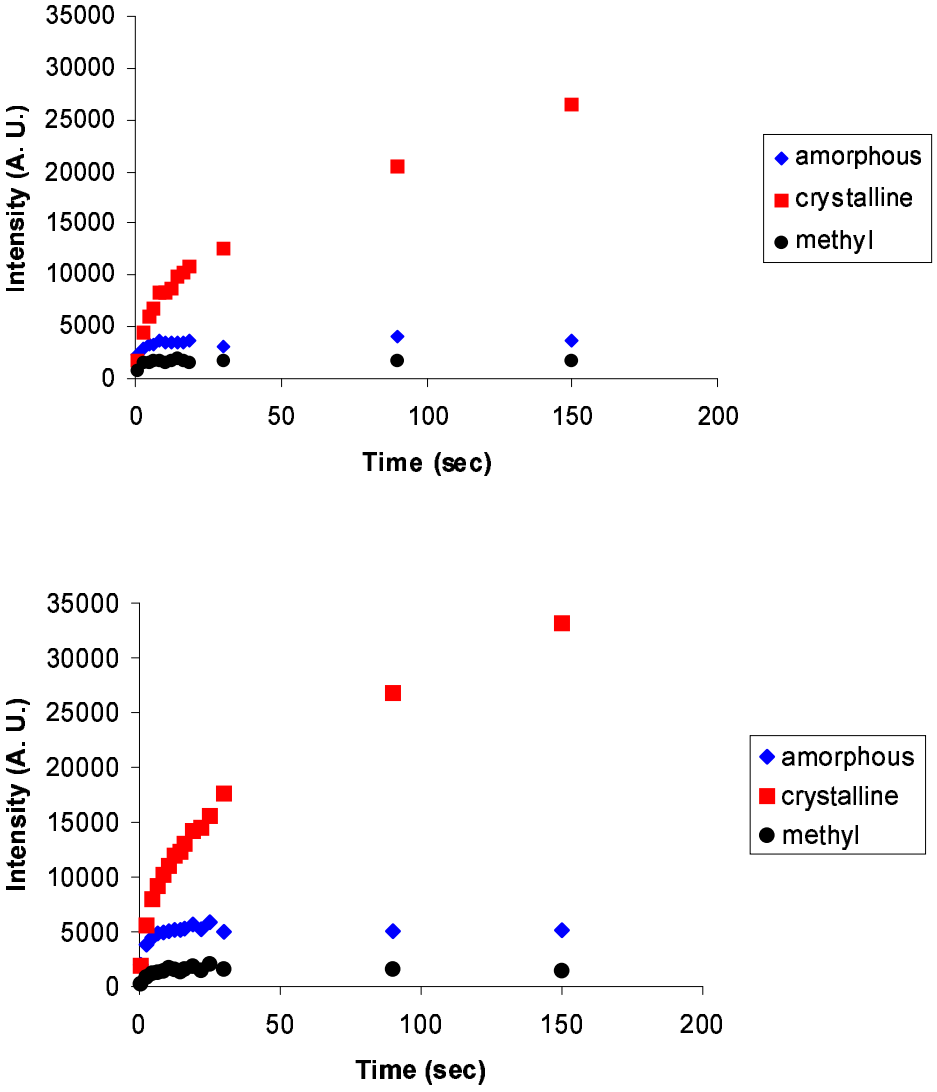

Figure 31: Saturation-recovery curves for OF at (a) 20°C and 60°C (b). Note that at higher temperature the amount of amorphous phase is slightly larger and that the recovery of the crystalline magnetization is faster. The analysis of the data is given in the text

There has been considerable argument over the years concerning the way in which folding occurs and the nature of the fold plane[62]. The models range from random re-entry ones, where a molecule leaves and re-enters a crystal randomly, to adjacent re-entry models, whereby molecules leave and re-enter the crystals in adjacent position. The main consensus of opinion appears to be that in single crystals grown from dilute solution the molecules undergo adjacent re-entry[125]. Two particular adjacent re-entry models have been suggested where the folds are either regular and tight or irregular and of variable length (Figure 32). Our data prove unambiguously that the fold involves no more than 6-7 carbon nuclei (this result comes from the N_a values reported in Table 5) and for this reason we can confirm that, for the OF sample studied, the model of Figure 32 (a) is the case.

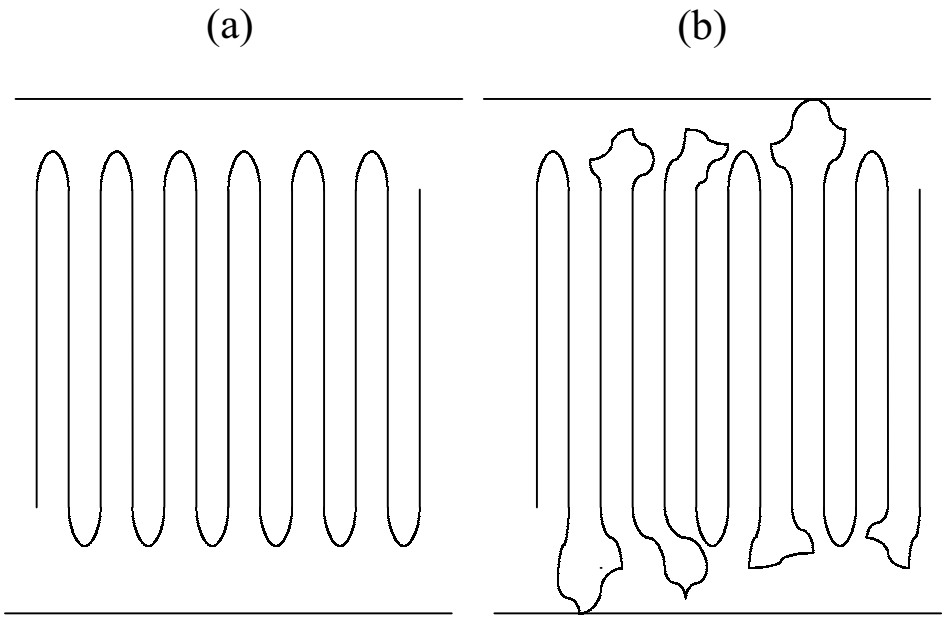

Figure 32: Adjacent re-entry models: (a) folds are regular and tight and only few carbon atoms are involved; (b) the folds are irregular and of different lengths and dozens of carbon atoms are involved.

Comparing the 1D spectrum for PE, OF and E allows the possibility to draw other important conclusions. While for PE the amorphous peak is well resolved and separated from the crystalline one, in OF the two lines are not as well resolved. In this case it is possible to fit the amorphous peak with two Gaussians, one at the same chemical shift as in PE (29.5 ppm), and an additional peak at 27.5 ppm, not present in the 1D spectrum of PE and E. As mentioned above, the amorphous peak corresponds to ^{13}C nuclei that are in gauche-gauche conformations. Following the *ab initio* calculations[126] of Born and Spiess, we can attribute the two peaks at 29.5 ppm and 27.5 ppm to ^{13}C nuclei with one and two gauche conformers in the γ position, respectively. This important result can be explained by considering the nature of the fold. Our experimental results show that in OF the fold is very tight and involves only 6-7 carbon nuclei. Computer models of PE folds in the literature[127] predict similar tight folds, involving only 7-8 carbon nuclei, with the bonds in the sequence $g^-g^-g^+g^+tg^+$, where $g^\pm$ represents a conformer with a gauche torsion of a positive or negative torsional angle. In long chain *n*-alkanes, only two nuclei will have both the γ-carbons gauche, while the rest will have one γ-carbon trans and gauche. On the other hand, we found that in PE the fold is not as tight and there are not many carbon nuclei with both γ-carbons in a gauche conformation, so that the only peak present in the spectrum is the one that corresponds to the carbons with only one γ-carbon gauche (29.5 ppm).

Analogously in E there are no folds, so that the peak at 27.5 ppm is not present, while the very small peak at 29.5 ppm is attributed to the very few ^{13}C nuclei that have one γ-carbon in a gauche conformation.

This result is surprising when compared with previous findings in the literature[124] where the fold in $C_{246}H_{494}$ has been quantified to contain 24 bonds. In order to understand this one has to consider the procedure used to prepare the OF sample. As mentioned above, the super cooling of the sample from the melt has to be carried out in a very controlled way in order to get a fold as tight as few carbon nuclei. If the sample is quenched from the melt, the number of nuclei involved in the fold can increase by as much as 20-30 nuclei. These considerations are supported by our NMR data in Figure 33, where the ^{13}C spectrum of a sample that was rapidly quenched from the melt is shown. In this case the peak at 29.5 ppm for the amorphous part is much more intense than in Figure 30 (a), since the number of nuclei involved in the fold in this case equal to about 25 (calculated from the normalization with the methyl groups). It is also important to notice that in this case only the peak at 29.5 ppm is present in the spectrum for the amorphous part. As expected, there are no carbon nuclei that have two γ-carbons in a gauche conformation because in this case the fold is not as tight as in OF, being similar to the fold found for UHMWPE.

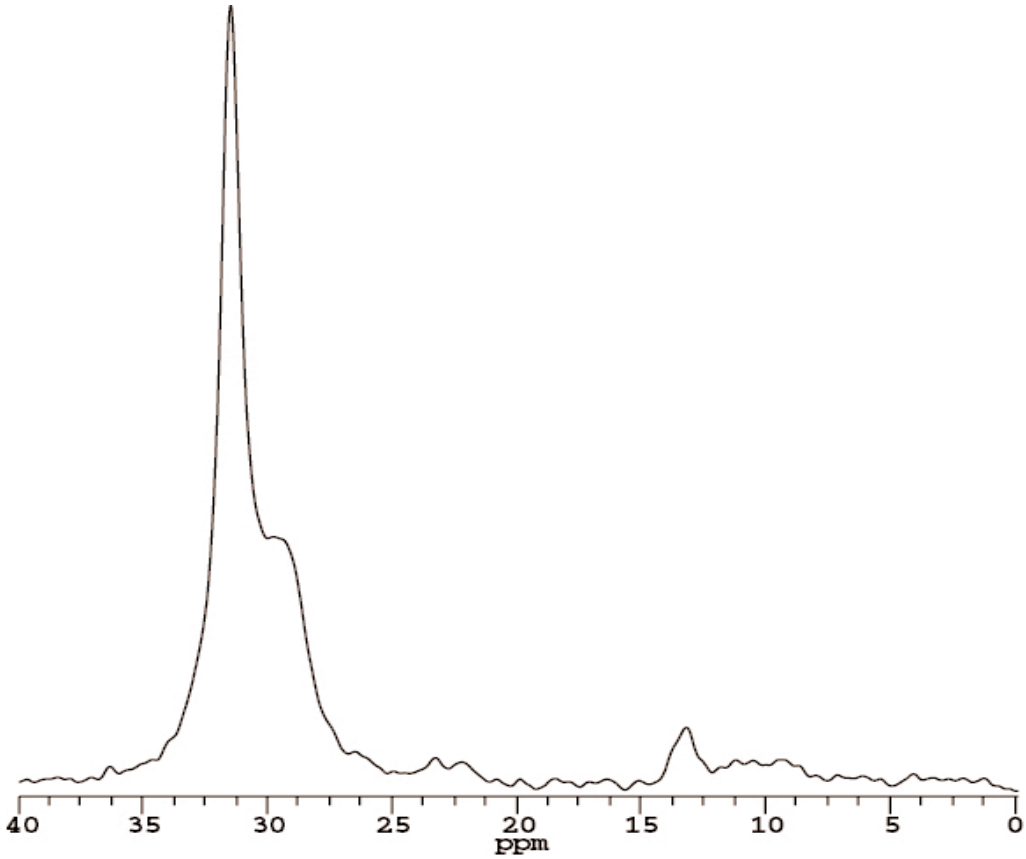

Figure 33: 1D spectrum for OF quenched from the melt. The full spectral width was 15 kHz, the acquisition time was 34.12 ms and a relaxation delay (τ_D) of 15 s was inserted between scans. Note that in this case the amorphous peak at 29.5 ppm is larger than in Figure 30 (a) due to the fact that the number of carbon nuclei involved in the loop is, for the sample prepared in this way, equal to about 25.

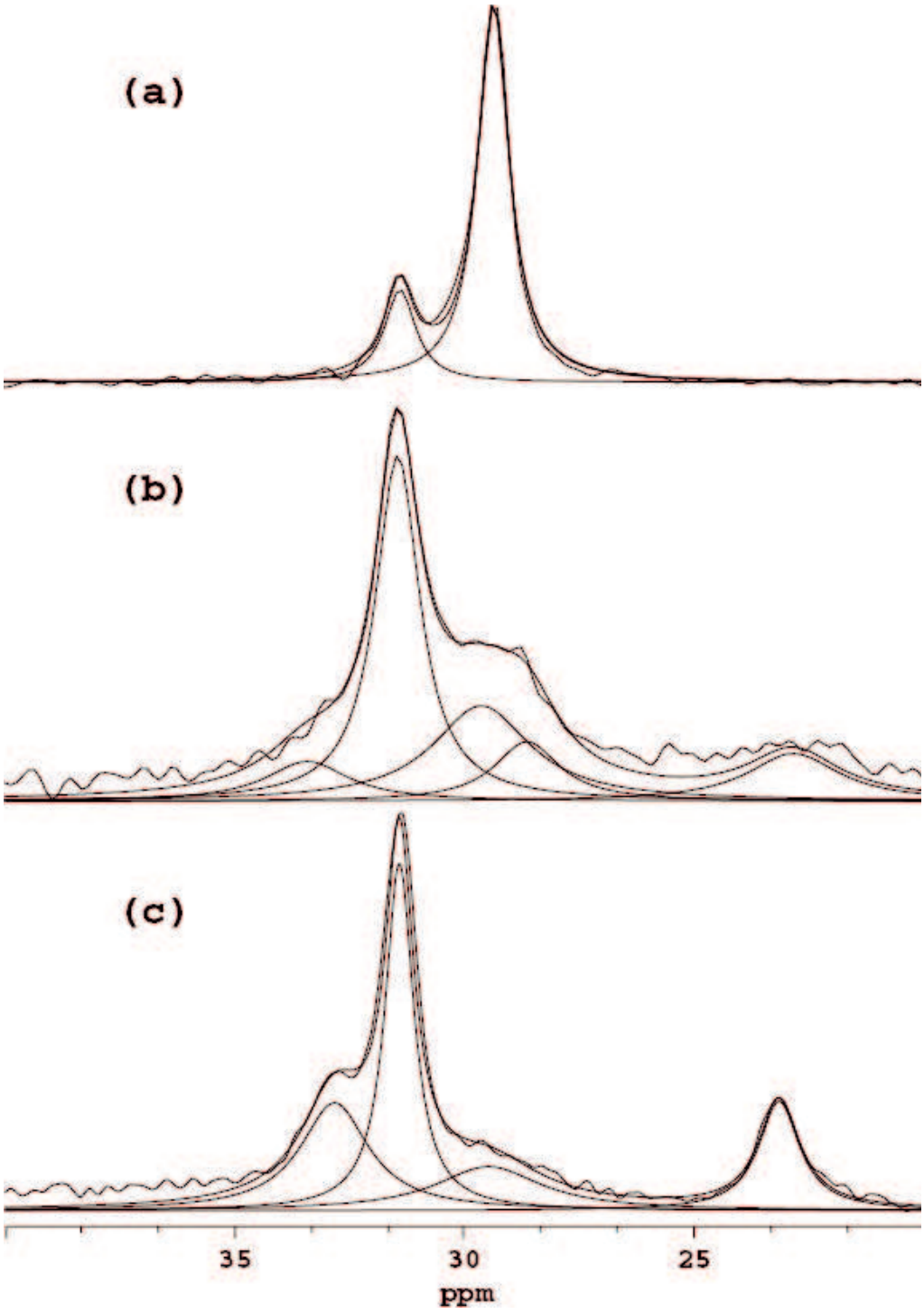

Figure 34: 1D spectrum at room temperature of UHMWPE (a), OF (b) and E (c) obtained using the pulse sequence of Figure 22 with a relaxation delay τ_D of 20 s in order to ensure that the amorphous peak was fully relaxed. The deconvolution of the spectra is explained in the text.

The same simulations of chain diffusion done for UHMWPE can be repeated here. In this case, the fact that chain diffusion alone cannot explain the recovery of magnetization is even more evident, and from this fact we can also draw some other important conclusions. Only a small portion of the crystalline part samples the amorphous region, because the methyl group cannot enter the crystalline lamellae. This observation is in contrast to the proposal of P. G. Klein *et al.*[124] that the methyl group is unconstrained, but is consistent with the X-ray scattering work done on the sample, as reported in Ref. 63. Therefore chain diffusion cannot be the only way for the crystalline magnetization to recover and, once again, a crystalline portion (the interphase) that relaxes through a rapid T_1 relaxation process must be present. Our simulations fit the experimental data for both OF and E using a modified version of the simulation program developed previously for UHMWPE. For OF the model consists of 2 crystalline stems with 117 repeat units and 1 amorphous loop (plus two chain ends) with 6 repeat units. The interphase consisted of 20 nuclei (≅10% of the crystalline phase) which, although contributing to the crystalline signal, were made to relax with a $T_1 \cong 6$ s. An average over ten simulations was taken in order to obtain a more reliable result. A schematic representation of the OF structure as predicted by our model is shown in Figure 37. For E the same parameters were used but no amorphous loop was introduced, so that the crystalline stem contained 240 repeat units, 20 of which constituted the interphase as in OF.

The ^{13}C nuclei in the amorphous regions were allowed to relax with relaxation time constant (T_1) obtained from the experimental curves of the amorphous part ($T_{1a} \cong 2$ s). Again, chain diffusion was executed as a microscopic random

process in the same way as for UHMWPE at different temperatures. For E the only constraint was that the methyl group was prevented from penetrating the crystalline stem, while for OF, in addition, the loop was not allowed to be less than 4 repeat units. The data fitted at two different temperatures with the y-axis normalized to the methyl intensity are shown in Figure 35 for OF, and in Figure 36 for E.

In the simulations of the amorphous peak intensities, the curves show an oscillation that is visible in the graphs as "noise". This feature can be explained by the following argument. As in UHMWPE, the number of carbon nuclei that are in the amorphous part can vary at each diffusion step, due to the different number of atoms that are involved in the fold at a particular time. Nevertheless, in contrast to UHMWPE where there is a large amorphous part (more than 20000 carbon nuclei), for OF and E the variation of ±2 carbon nuclei can be observed, as it represents a significant fraction of the total amount of carbons in the amorphous phase. Although this does not affect the conclusions drawn from the simulations, in order to avoid this effect, the simulation would need to be run for a prohibitively long time.

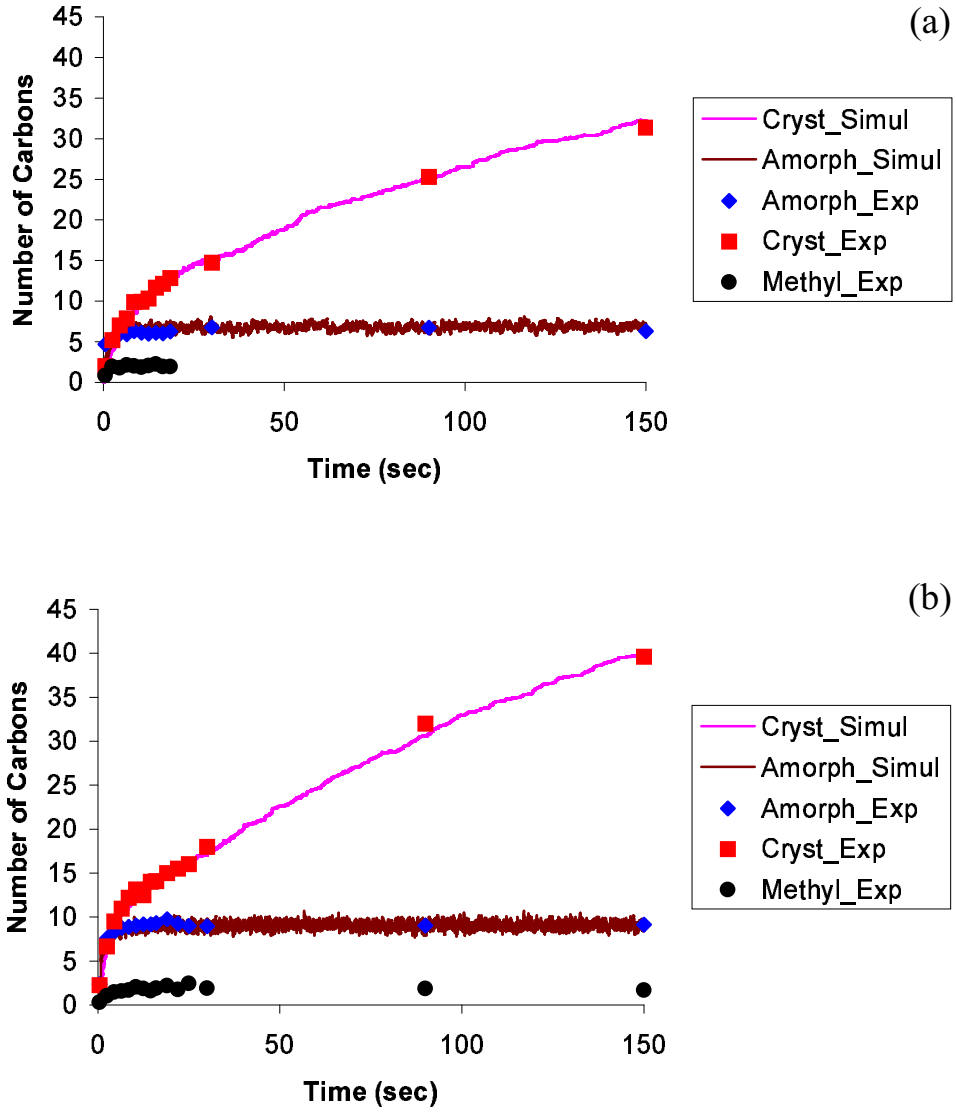

Figure 35: Montecarlo simulation of the relaxation curves for the OF at 20°C (a) and 60°C (b). In the same graph the crystalline, the amorphous and the methyl group lines are plotted and the intensities are normalized in order to obtain the number of carbon nuclei on the y-axis. The noise observed in the simulations of the amorphous curve is justified in the text.

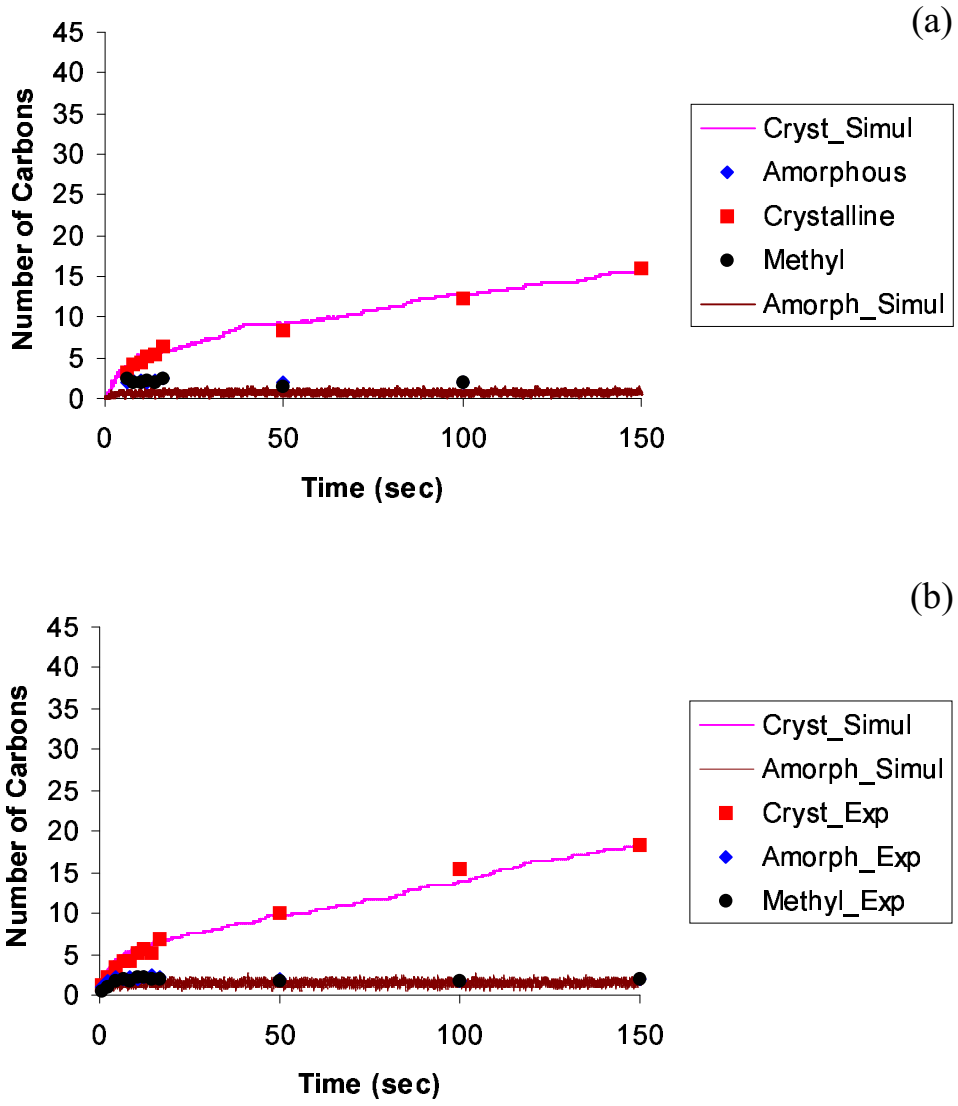

Figure 36: Montecarlo simulation of the relaxation curves for the (E) at 20°C (a) and 60°C (b). In the same graph the crystalline, the amorphous and the methyl group lines are plotted and the intensities are normalized in order to obtain the number of carbons on the y-axis. The wiggle observed in the simulations of the amorphous curve is justified in the text.

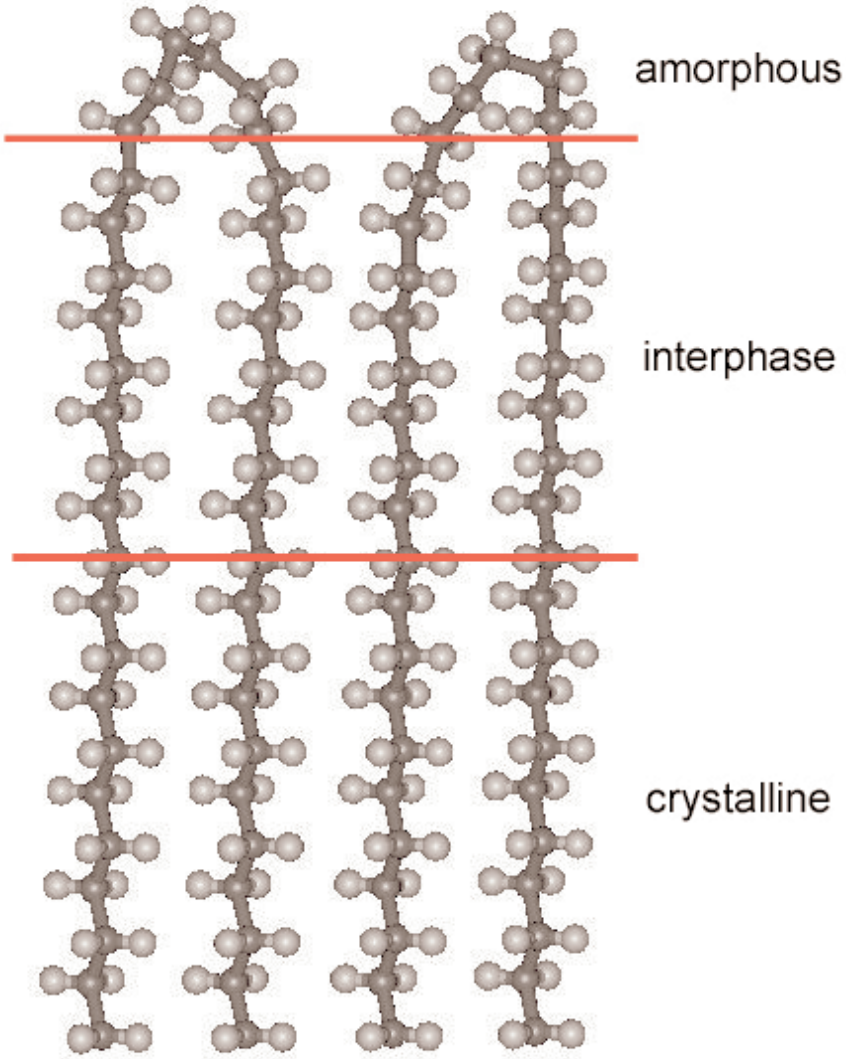

Figure 37: schematic representation of the OF structure. For simplicity the amorphous part is constituted by folds only and the chain ends are not represented. Note also that the crystalline part is not in scale with the rest of the picture but it is truncated to highlight the other regions.

3.3.3 Deuterated *n*-alkane ($C_{216}H_{434}$-d_{24})

The success of the deuteration of the chain ends can be checked by performing a normal cp spectrum as shown in Figure 38 where the cp spectrum of $C_{216}H_{434}$-d_{24} (extended form) is reported together with a cp spectrum of $C_{246}H_{494}$ (E). The spectra were recorded with the same conditions as in Figure 30, apart from the initial cross-polarization carried out with a contact time of 3 ms and a τ_D = 20 s. The cp spectrum shown in Figure 38 confirms that the sample has one deuterated chain end, since the peaks associated with the chain ends decrease in intensity by a factor of two (peaks at 13.4 and 23.3 ppm). This is because there is no cross-polarization for the deuterated ^{13}C, so that the signal from these sites disappears.

The ^{2}H NMR data were obtained at a deuterium frequency of 46.06 MHz. In order to obtain the spectra shown in Figure 39, the solid echo experiment was performed[109] as explained in section 3.2.3.1. The line shape of the solid echo spectra (Figure 39) can be treated as a superposition of the spectrum in the rigid lattice limit and a motionally narrowed central region attributed to the "amorphous part" as it has been done in the literature for PE[109]. Nevertheless, the spectra recorded performing the simple solid echo experiment are already quite different from all the ones reported in literature for PE[61]. In the latter case the amorphous part was present as a Lorentzian peak in the middle of the Pake pattern that tended to disappear at low temperature, when the entire polymer is considered to be rigid. In our sample the amorphous part gives rise to a motionally averaged Pake pattern inside the one due to the rigid part. Before analysing in more detail the reasons why this is happening, it is useful to consider Figure 40, where two solid echo spectra of $C_{216}H_{434}$-d_{24} are shown

at the same temperature of -100°C. All the experimental conditions were the same as the ones used in Figure 39, except that in Figure 40 (a) a τ_D of 10 s has been used, while in Figure 40 (b) the τ_D was only 1 s, in order to emphasize the mobile part.

The methyl line shape (motionally narrowed Pake pattern) does not disappear at low temperatures and is well resolved from about –20°C. At these temperatures the spectra recorded are a superposition of two different Pake patterns, as shown in Figure 40 (a). This means that the behaviour of the chain ends is not the same as the bulk (as proved with the non-deuterated samples). This difference between the chain ends (inner Pake pattern) and the rest of the chain (outer Pake pattern) has never been observed for PE. In that case parts of the chain ends such as the methyl groups represent only a small portion of the sample and their signal is obscured by the much larger signal from the chain. In our deuterated sample, the motion described by the line shape is a chain end motion, completely separated from the bulk motion.

For these reasons, an accurate study of the line shape at different temperatures can give us information about the motion of parts of the chains that could not be disclosed otherwise. Furthermore, as we discovered in the previous section, changing the temperature varies not only the correlation time but also the percentage of interphase and amorphous parts. In solid-state ^{2}H NMR this has a large impact on the line shape of the solid echo spectrum that for this reason contains also information about the changes in the structure of these semi-crystalline samples and this is clearly shown by the changes in the features of Figure 39.

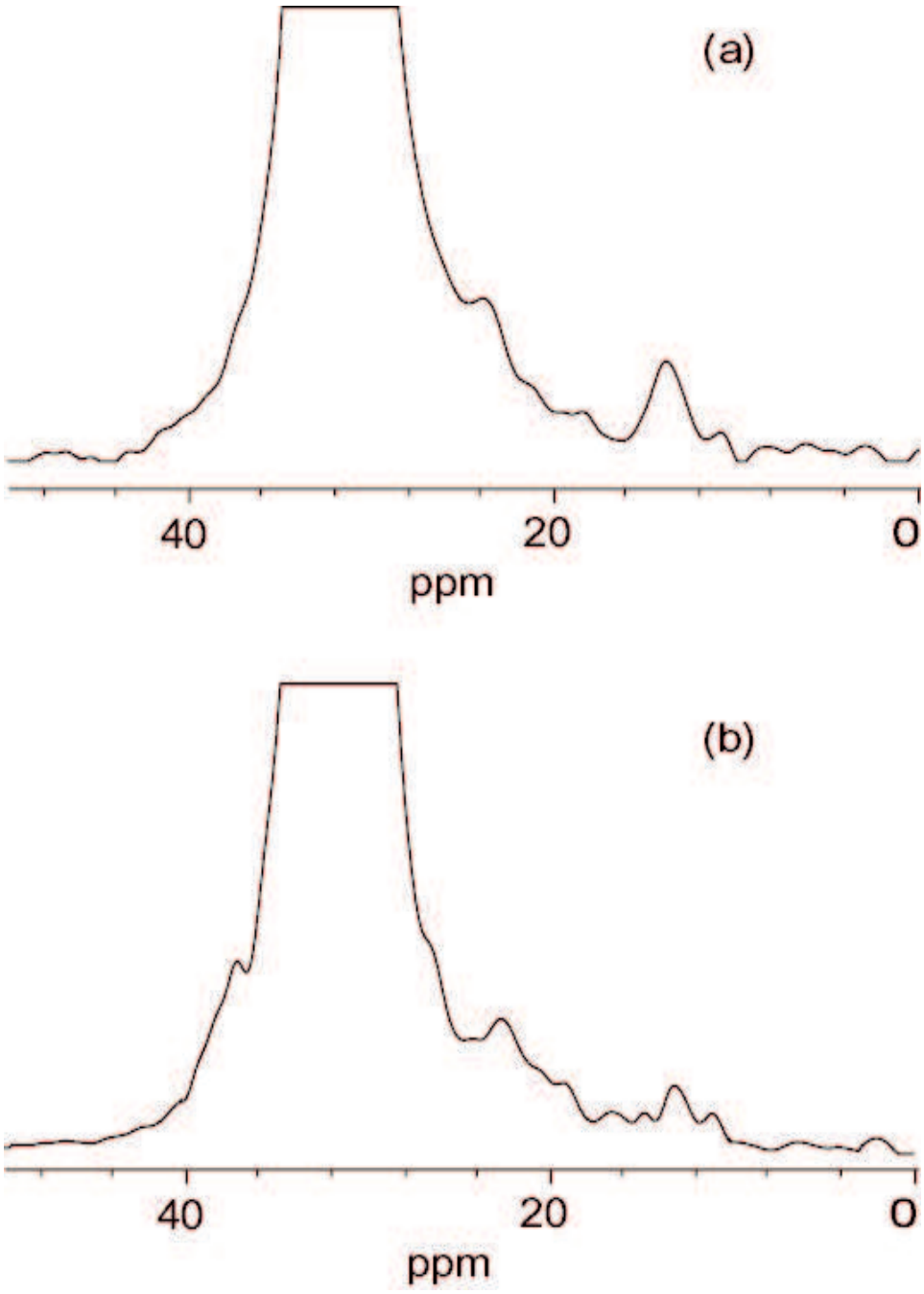

Figure 38: Cross polarization ^{13}C 1D spectra for E (a) and $C_{216}H_{434}$-d_{24} (b). The peak at about 30 ppm is truncated to emphasize the chain ends. Note that in (b) the signal from the chain end normalized to the main peak at about 30 ppm is halved as cross polarization cannot happen for the one chain end that is deuterated.

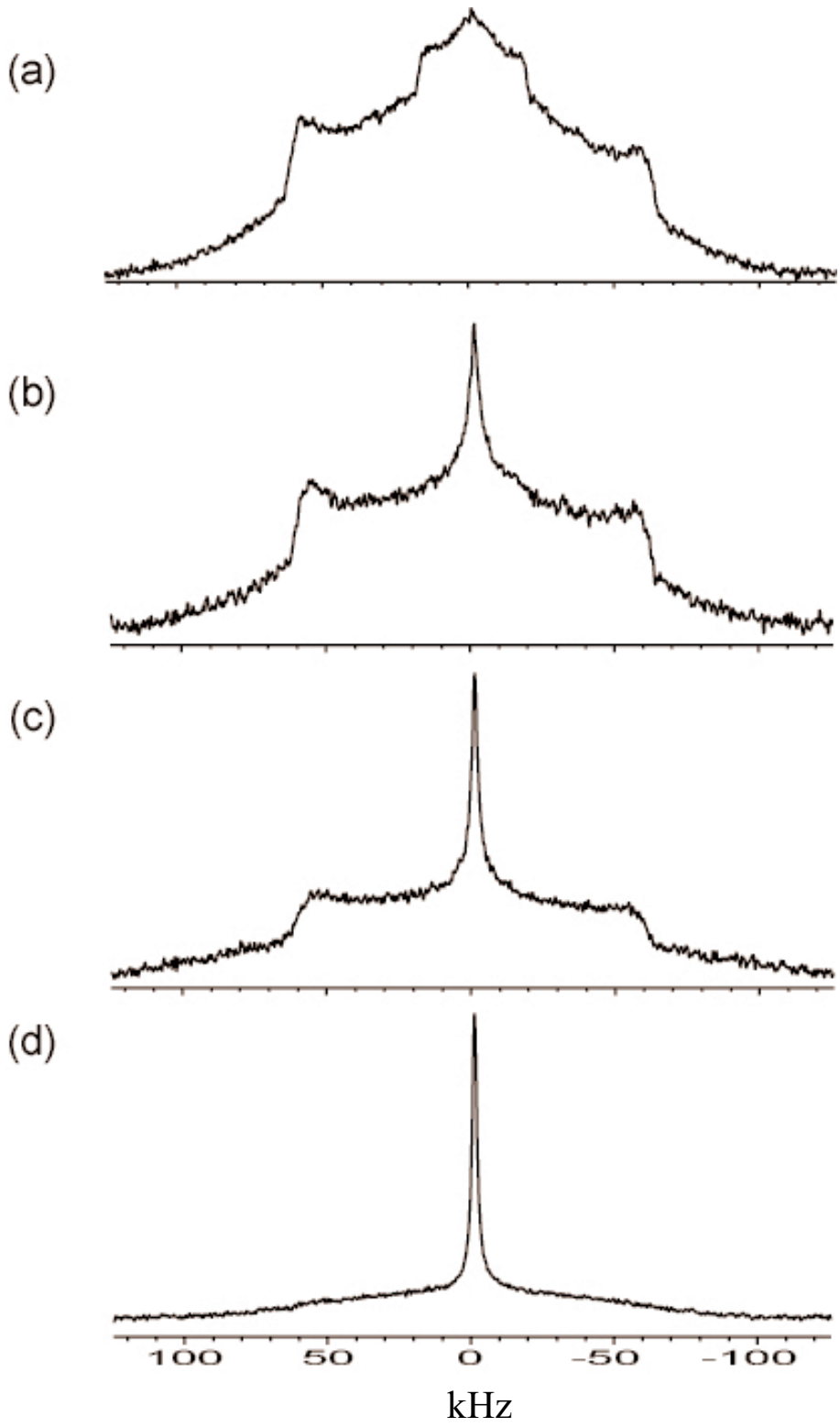

Figure 39: Solid-echo spectrum for $C_{216}H_{434}$-d_{24} at 50°C (a), 90°C (b), 100°C (c) and 120°C (d). The solid echo time was 100 μs, the τ_D 10 s, the acquisition time 4.096 ms, the spectral width 250 kHz and the number of scans was 2224. The pulse length of 1.55 μs was sufficiently short for obtaining solid-state ^2H spectra that were reduced in intensity by only about 5% at the outer edges.

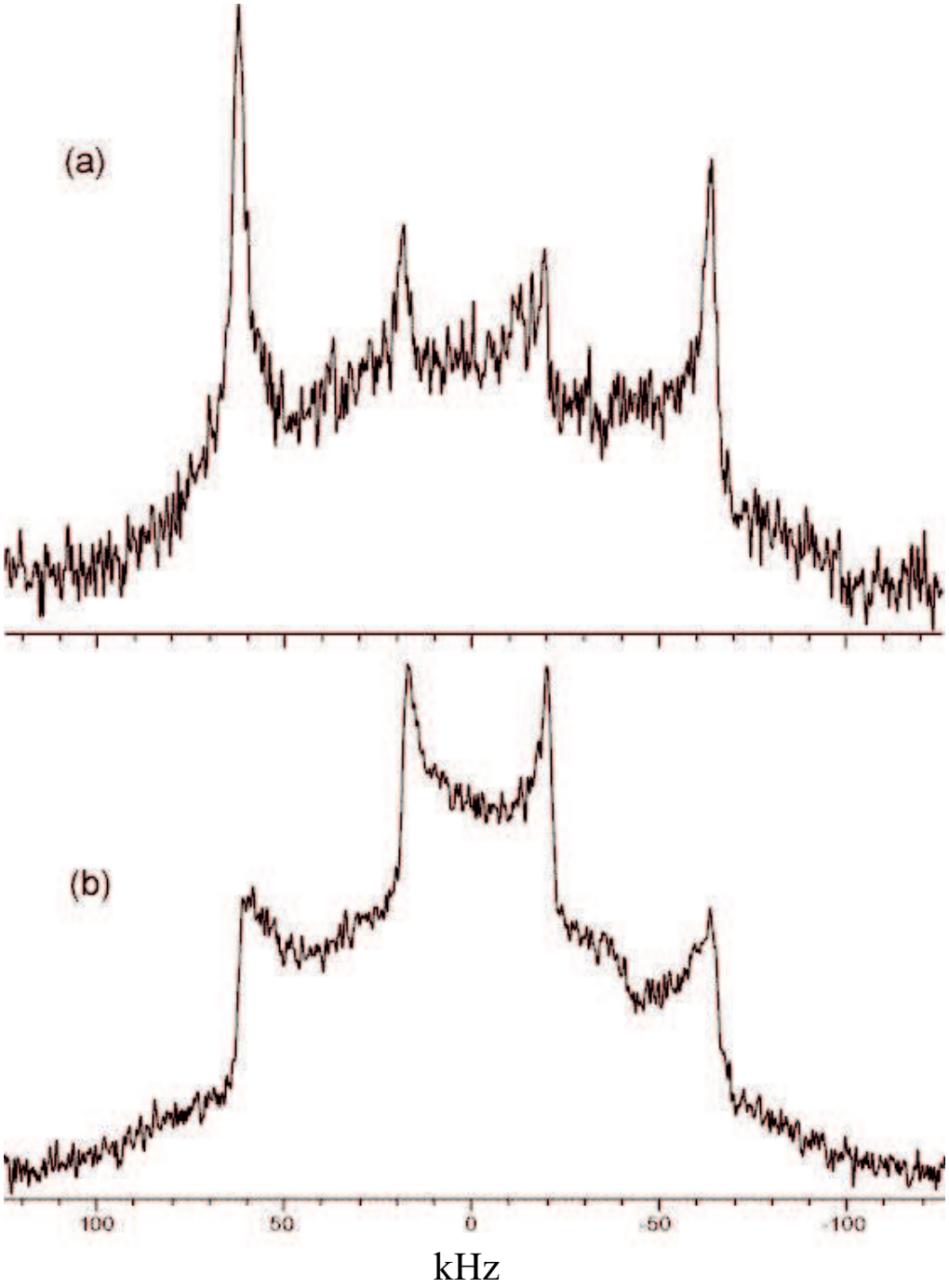

Figure 40: Solid-Echo spectra of $C_{216}H_{434}$-d_{24} recorded at –100°C with τ_D = 10 s (a) and τ_D = 1 s (b). All the other acquisition parameters are the same as in Figure 39.

In order to fit the experimental line shape, we wrote a simulation program based on the method described in section 1.3.2. In the literature only two simple motional mechanisms are considered for *n*-alkanes, the "kink" 3-bond motion[98,99] and the "crankshaft" 5-bond motion[100] (see Figure 41). The former involves three C-C bonds and there is an interchange between two C-H bond directions, while the latter involves five C-C bonds and there is an interchange between three C-H bond directions. The latter is the most common motion in the bulk. To simulate the experimental line shapes we used a model where the rotation of the methyl groups is included as a three-site motion (interchange between three C-H bond directions) with a short correlation time, while the rest of the chain undergoes the crankshaft 5-bond motion, with a longer correlation time (slower crankshaft motion). For high temperatures the introduction of isotropic motions was necessary. In Figure 42 and Figure 43 the calculated line shape is shown together with the experimental results obtained at different temperatures. The experimental line shape is simulated well at low temperatures using three different contributions (fast 3-fold rotational motion, slow crankshaft motion and rigid component). For -100^{o}C we have:

- A rigid part (72.5%) having a correlation time of 100 μs or more;
- A more mobile part (15%) having a correlation time of 0.22 μs (crankshaft);
- A very mobile part (12.5%) with a correlation time of 0.08 μs (3-fold rotation).

It is worth noticing that although the crankshaft motion and the methyl rotation are different, both motions are well simulated by a three-site model, as long as an appropriate correlation time is chosen.

Because of the small number of ^2H nuclei present in the sample, it is relatively easy to evaluate which parts of the chains are responsible for the different contributions to the line shape. To calculate the percentage of CD_3, it is sufficient to consider the formula of the compound $C_{12}H_{25}(CH_2)_{192}CHDC_{11}D_{23}$, obtaining straightforwardly :

$$\frac{3}{24} * 100 = 12.5\%$$

That is the same percentage found in the simulation for the very mobile part. This first result confirms that, even at this low temperature, the methyl group undergoes a 3-fold rotational motion with a small correlation time, even when NMR sees almost the entire sample as "static". From the simulation it is also possible to say that another four ^2H nuclei are relatively mobile even if they move more slowly than the CD_3 groups. This means that even at these low temperatures a very small portion of the chain is undergoing some motion, being in a molecular environment where there is an amount of "free space" (the same "amorphous" regions that contain the methyl groups). We attributed this slower motion to the two methylene groups next to the methyl group. The rest of the ^2H (72.5%) are completely static and this means that the nuclei in the interphase are not moving at all at these temperatures.

All the line shapes obtained at different temperatures have been simulated using the same criteria and the results are shown in Figure 42 and Figure 43.

Increasing the temperature up to 20^{o}C (Figure 42) has three major effects:

- The percentage of the static part decreases and the number of ^2H nuclei involved in the slow crankshaft motion increases;
- All the correlation times decrease;
- Part of the contribution of the fast 3-fold rotational motion is lost and an isotropic component starts to appear.

At this stage it is important to notice that for temperatures below 40°C the sum of the percentage of the isotropic and the fast rotational motion is always constant and equal to 12.5%, showing that is still only the methyl group that undergoes the isotropic motion.

Heating the sample above 40°C (Figure 43) causes an increasing amount of ^2H nuclei to undergo the isotropic motion, while the correlation times keep decreasing. At this stage all the ^2H nuclei in the methyl groups are undergoing isotropic motion.

At higher temperatures the isotropic component plays the largest role and tends to become more similar to a Lorentzian when the temperature is increased. This result has been found previously[19] and it shows that the system is in the fast exchange limit, where the line shape becomes independent of the exchange rate.

These simulations are a further proof that the amorphous part for the extended long *n*-alkanes is very small. Being only the last 12 carbon nuclei in the chains attached to deuterium atoms (from the formula $C_{12}H_{25}(CH_2)_{192}CHDC_{11}D_{23}$), the amorphous part has to be smaller than that, as a small percentage of the deuterated ends is shown to be static from Figure 43, even at temperatures as high as 100°C.

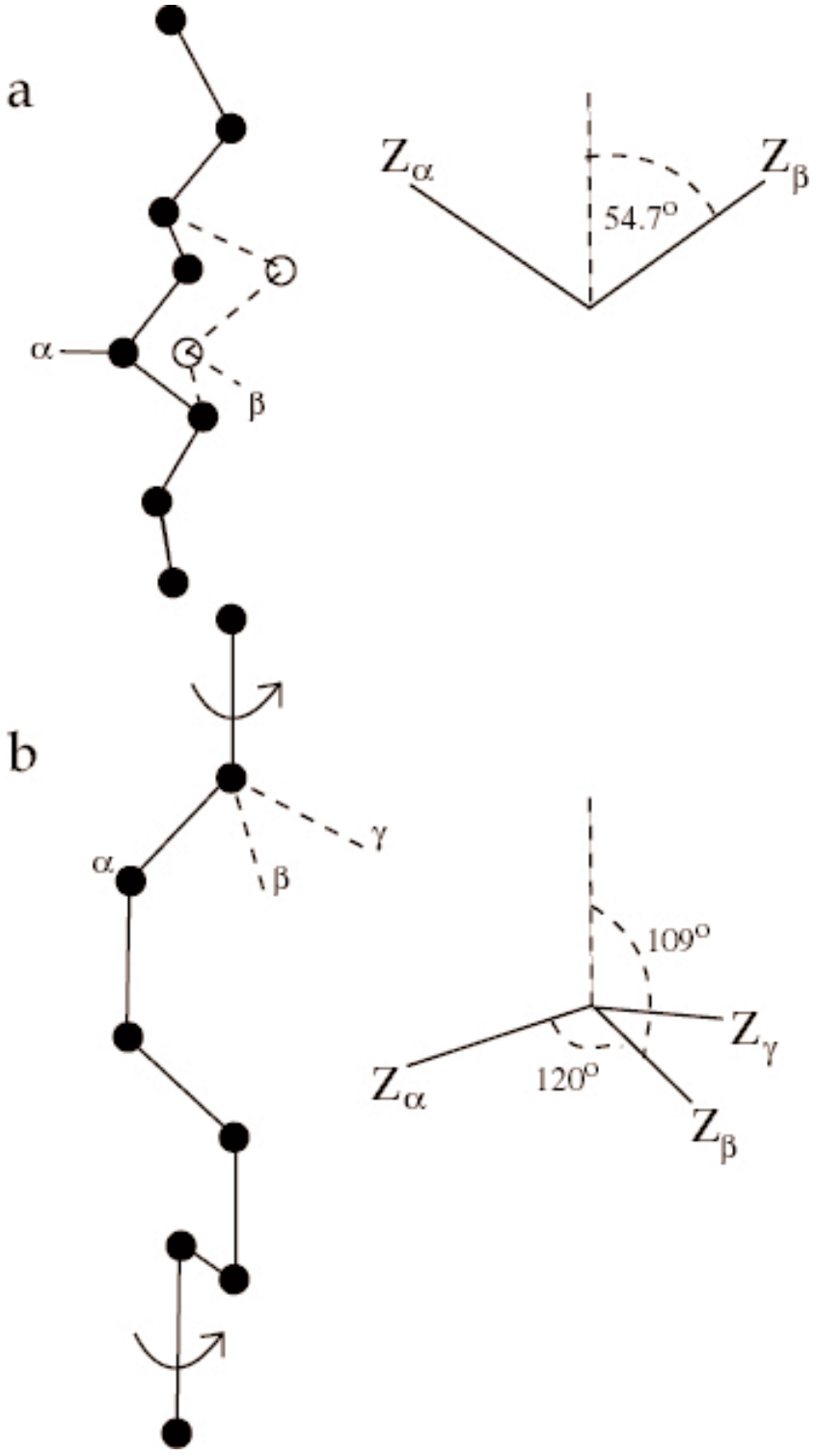

Figure 41: Sketch of simple motional mechanisms, the kink-3-bond motion (a) and the crankshaft 5-bond motion (b), involving interchange between 2 and 3 C-H directions, respectively.

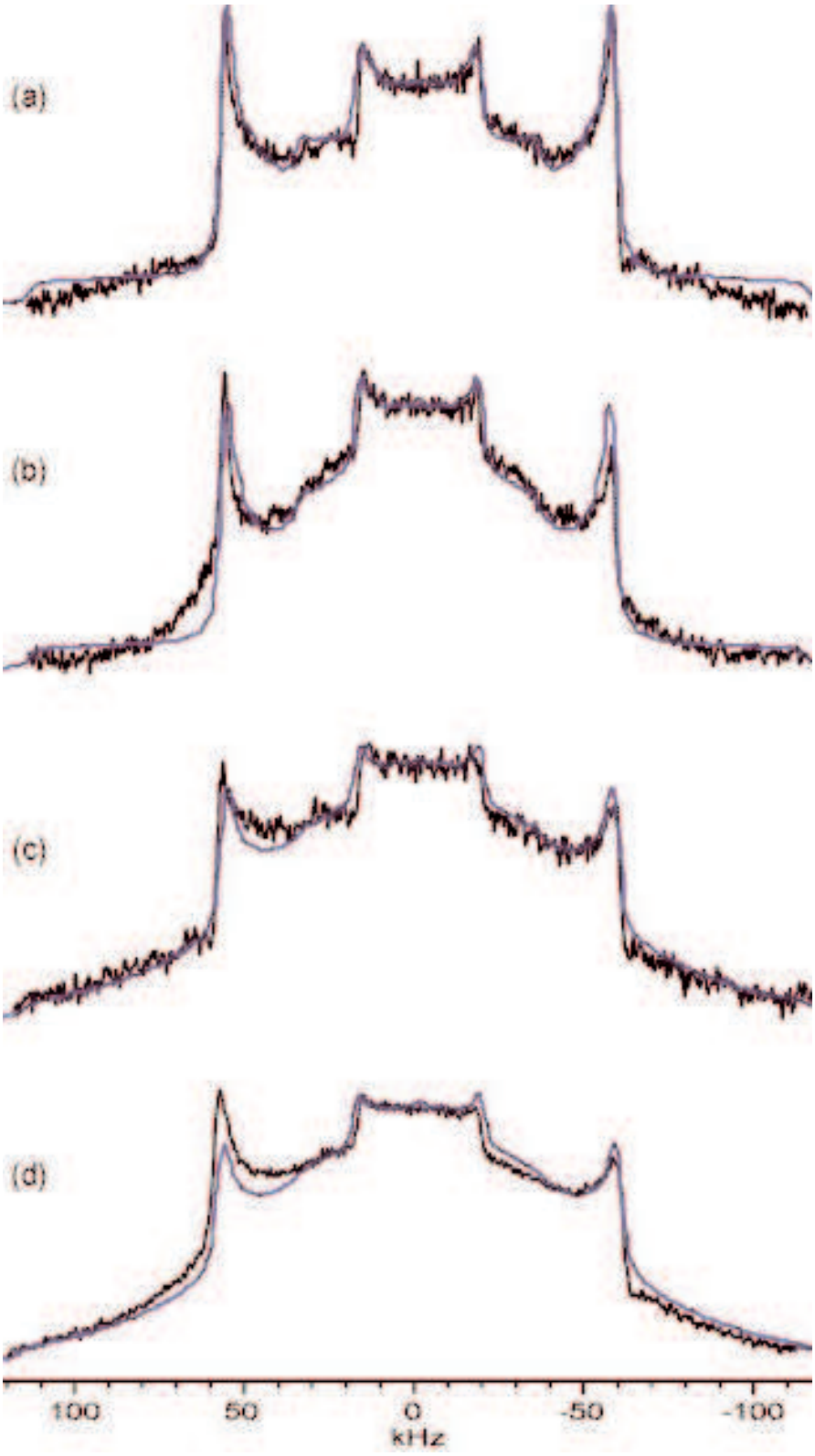

Figure 42: Simulation of the solid-echo spectrum (blue line) recorded at T = -100°C (a), -60°C (b), -20°C (c), +20°C (d). The acquisition parameters are the same as in Figure 39.

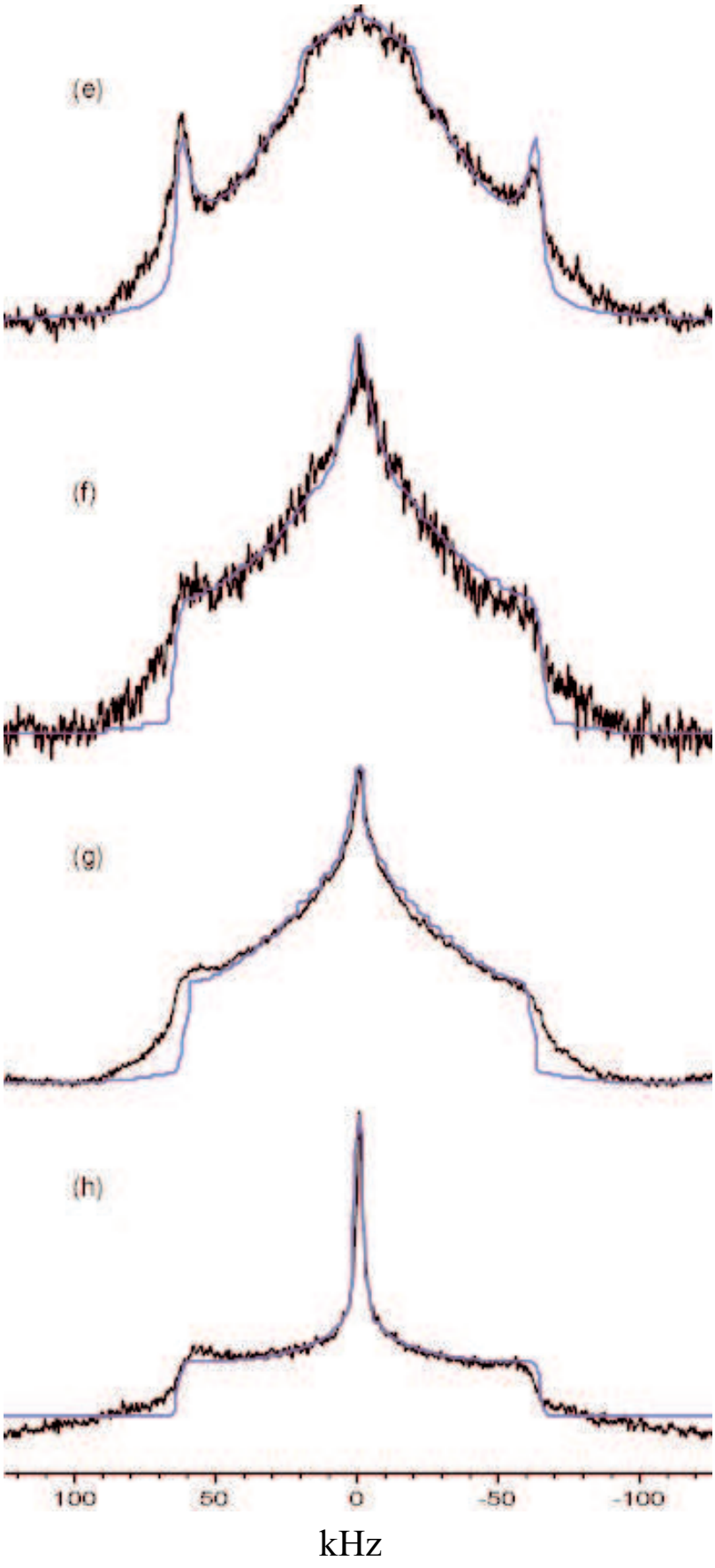

Figure 43: Simulation of the solid-echo spectrum (blue line) recorded at T = +40°C (e), +80°C (f), +90°C (g), +100°C (h). The acquisition parameters are the same as in Figure 39.

Studying the deuteron line shape as described above allowed us to observe the motion of the chain ends, nevertheless further quantitative information about the structure of our deuterated sample can be gained reverting, once again, to the investigation of the relaxation times in the ^2H spectra. In order to measure the relaxation times for the different portions of the deuterated samples, we performed the saturation-recovery experiment as explained in section 3.2.3.1. The relaxation times shown in Table 6 have been obtained by recording the solid echo amplitude as a function of τ_0 and by fitting the experimental curves obtained (Figure 44) to exponentials.

As mentioned above, the recovery of spin magnetization after saturation could clearly be separated into a rapid increase due to mobile deuterons in the amorphous regions and a slow increase due to "rigid" deuterons in the interphase regions. We determined the spin-lattice relaxation time at various temperatures for both rigid (T_{1I}) and amorphous (T_{1A}) deuterons performing the saturation-recovery experiments at different temperatures. In Figure 44 the increase of the integral intensity for the whole range of frequencies are shown at three different temperatures. It is important to notice that at room temperature it is impossible to fit the exponential increase with only one exponential curve, because the two different phases (interphase and amorphous) are both present in the percentages shown in Table 6. When the temperature increases the percentage of the interphase part tends to diminish and for a temperature equal to 100^{o}C it is already possible to fit the experimental curve with just one exponential, proving that at this temperature almost all the deuterated carbons can be considered to be in the amorphous phase.

Analogously, it is possible to estimate from this measurement the number of ^2H nuclei that are in the amorphous part of the sample at room temperature (N_a (^2H)), which is:

N_a (^2H) = 34×(number of ^2H)/100 = 34×24/100 ≅ 8

Eight ^2H atoms are then in the amorphous part at room temperature. This means that, excluding the methyl and the methylene group bonded to the methyl, about 1.5 carbon nuclei are in the amorphous phase, according to this calculation. This number has to be multiplied by 2, as in this case only one end of the molecule is analysed. This result fits very well with the calculation done in the previous section from the carbon spectrum of the E form, where about 2±1 carbon nuclei have been found in the amorphous phase, excluding the methyl and the first methylene group of the chain at room temperature. In both different calculations, the amorphous part in the E sample is smaller than the one found in the OF, and never larger than a few carbon nuclei.

Temperatures (^{o}C)	T_{1I}	T_{1A}	%I	%A
25	7.7 s	0.8 s	66	34
85	1 s	0.4 s	57	43
100	0.4 s	0.4 s	1 phase	1 phase

Table 6: T_1 relaxation time at different temperatures for the fitting of the exponential increases reported in Figure 44. From the parameters used in the fitting it is possible to extrapolate the percentages of the phases (T_{1I} = T_1 for the interphase, T_{1A} = T_1 for the amorphous part). For temperatures ≥ 100^{o}C only one phase is detected.

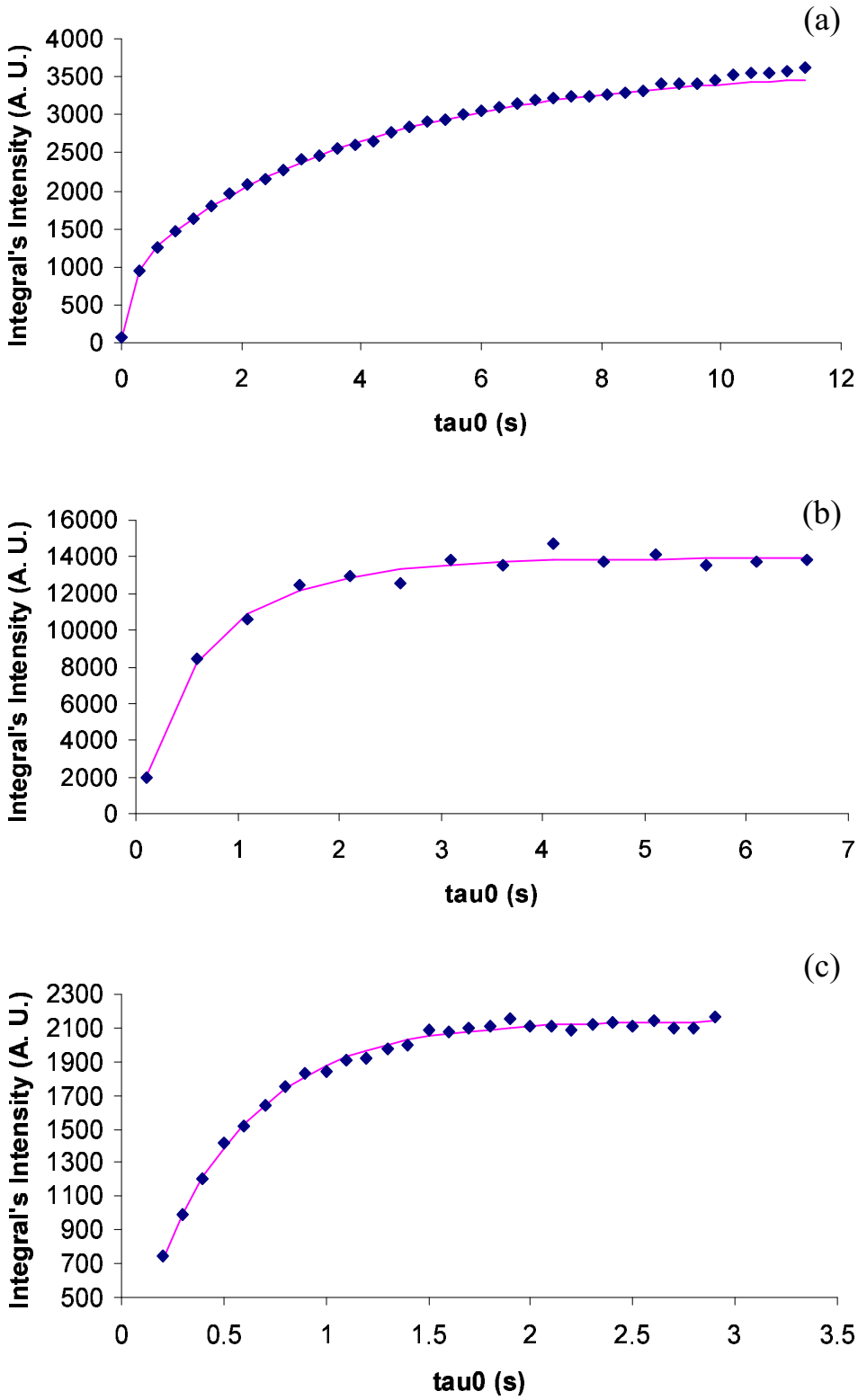

Figure 44: Curves of the recovery of the magnetization obtained performing the Saturation-Recovery experiment described in Figure 26 at 25°C (a), 85°C (b), 100°C (c). The solid line is the result of a double exponential fit for (a), (b) and a single exponential for (c).

3.3.4 Mixture of *n*-alkanes

The peculiarity of the mixture is that two *n*-alkanes having different lengths are mixed and only the longer *n*-alkane has deuterated chain ends. In Figure 45 the solid-echo spectra at different temperatures of the mixture are shown. It is possible to see that there are significant differences from the case studied previously ($C_{216}H_{434}$-d_{24}, see Figure 39). The narrowing of the Pake pattern into a single line due to isotropic motion occurs at a lower temperature in this case and this is an indication that the motion of the chains in the lamellae are different. The molecules are much more mobile even at room temperature and this can be interpreted in terms of the so-called super-lattice structure proposed by Ungar and Zeng[91]. In that model a binary mixture of long *n*-alkanes with the chain length ratio between 1.3 and 2 have been found to form predominantly two mixed phases, a high-temperature one and a low-temperature one, separated by a reversible transition at about 100^{o}C. While the shorter *n*-alkane chains are fully crystalline and confined to the crystalline layer, in the high-temperature phase the longer *n*-alkane chains traverse the crystalline layer and the surplus length, the cilia, form the amorphous layer. Below the phase transition temperature, according to Ungar and Zeng there is the formation of a super-lattice crystalline structure based on a triple-layer repeat unit. The two outer layers contain extended chains of the shorter *n*-alkane (in our case $C_{162}H_{326}$) as well as the major portion of the longer chain molecules ($C_{216}H_{434}$-d_{24}). The middle layer contains only the surplus length of the longer molecules protruding from the two end-layers and, according to Ref. 91, at room temperature even this middle layer is crystalline. This last assertion is not confirmed by our NMR data. Because only the chain ends of

the longer *n*-alkane are deuterated, these are the nuclei that give rise to the line shape in the spectra and therefore the early narrowing of the Pake pattern into a single line due to isotropic motion at low temperatures (<100^{o}C) seen in Figure 45 supports a structure where the small middle layer is not totally crystalline even at 100^{o}C. On the other hand, if the middle layer was completely amorphous, we should not be able to observe any static contribution in the line shape of Figure 45, even for temperatures below 100^{o}C. The fact that we see a static contribution for temperatures up to 80^{o}C means that in this regime the middle layer is still restricted in its mobility, being more mobile than the interphase in $C_{216}H_{434}$-d_{24}, but less mobile than an amorphous layer completely constituted by just chain ends.

Furthermore, the transition from the super lattice structure and the formation of a structure that is just an alternation of amorphous and crystalline layers seems to be more gradual from our NMR data as we do not see a sharp change at 100^{o}C, but a gradual increment of the mobility of the middle layer, that eventually will be mobile as an amorphous layer constituted only of chain ends for temperature > 100^{o}C.

All these results are confirmed by the Saturation–Recovery experiments performed on this sample (See Table 7) as seen for the $C_{216}H_{434}$-d_{24} sample. The motion in this case is much faster and already at a temperature equal to about 25^{o} C the NMR sees the middle layer relaxing with two T_1 constants, one of them (T_{1MA}) attributed to the very mobile chain ends (methyl, last methylene bonded to the methyl) having a very short correlation time, and the other one (T_{1M}) attributed to the middle layer that is more mobile than the interphase in $C_{216}H_{434}$-d_{24}, as explained above. This proves the peculiarity of

this layer that cannot be described either as a complete crystalline or amorphous one, having the very mobile chain ends inserted in a semi-ordered structure.

T(°C)	T_{1I}(a)	T_{1A}(a)	%I	%A	T_{1M}(b)	$T1_{MA}$(b)	%M	%M(A)
25	7.7 (s)	0.8 (s)	66	34	4.9 (s)	0.8 (s)	46	54
85	1.0 (s)	0.4 (s)	57	43	0.8 (s)	0.4 (s)	15	85

Table 7: T_1 relaxation times and percentages for the interphase and the amorphous parts at two different temperatures are listed for sample $C_{216}H_{434}$-d_{24} (a) in comparison with the T_1 relaxation times and percentages of the middle layer (T_{1M} and T_{1MA} from the double exponential fit) for the mixture (b). These values have been calculated performing the Saturation-Recovery experiment.

In Figure 46 a comparison of the spectra at minus 100°C for the two different samples, $C_{216}H_{434}$-d_{24} and the mixture, shows some interesting features. As discussed above, the inner Pake pattern is due to a fast motion where there is an interchange between three C-H bond directions that was attributed for sample ($C_{216}H_{434}$-d_{24}) to the rotation of the methyl group. In the mixture the percentage of this motion rises from 12% to 30% as it is calculated from the simulation shown in Figure 47. Clearly in this case not only the methyl group undergoes to that kind of motion, but other sites as well. This means that even at this very low temperature the super-lattice structure has an amorphous layer where the nuclei move faster than everywhere else in the sample.

Following the same procedure as in section 3.3.3, we fitted all the experimental line shapes at different temperatures using our simulation program according to the Heaton model. The results are shown in Figure 48 and two important considerations can be drawn:

- From the percentage obtained to simulate the experimental line shapes we can say that, even at temperatures as low as -100^{o}C, at least 4 carbon nuclei in the chain experience a crankshaft 5-bond motion, with a correlation time similar to the one experienced by the methyl group in its rotational motion.
- The data are easily simulated using the same model as in sample ($C_{216}H_{434}$-d_{24}), but in this case the decrease of the correlation times used in the simulations is much more rapid, so that already at 90^{o}C all the deuterated carbons are undergoing isotropic motion.

These findings further prove that the introduction of a shorter *n*-alkane in the structure of sample ($C_{216}H_{434}$-d_{24}) drastically changed the overall picture, where the deuterated chain ends of the longer *n*-alkane are more mobile as they are inserted in the middle layer of the super lattice structure as explained above.

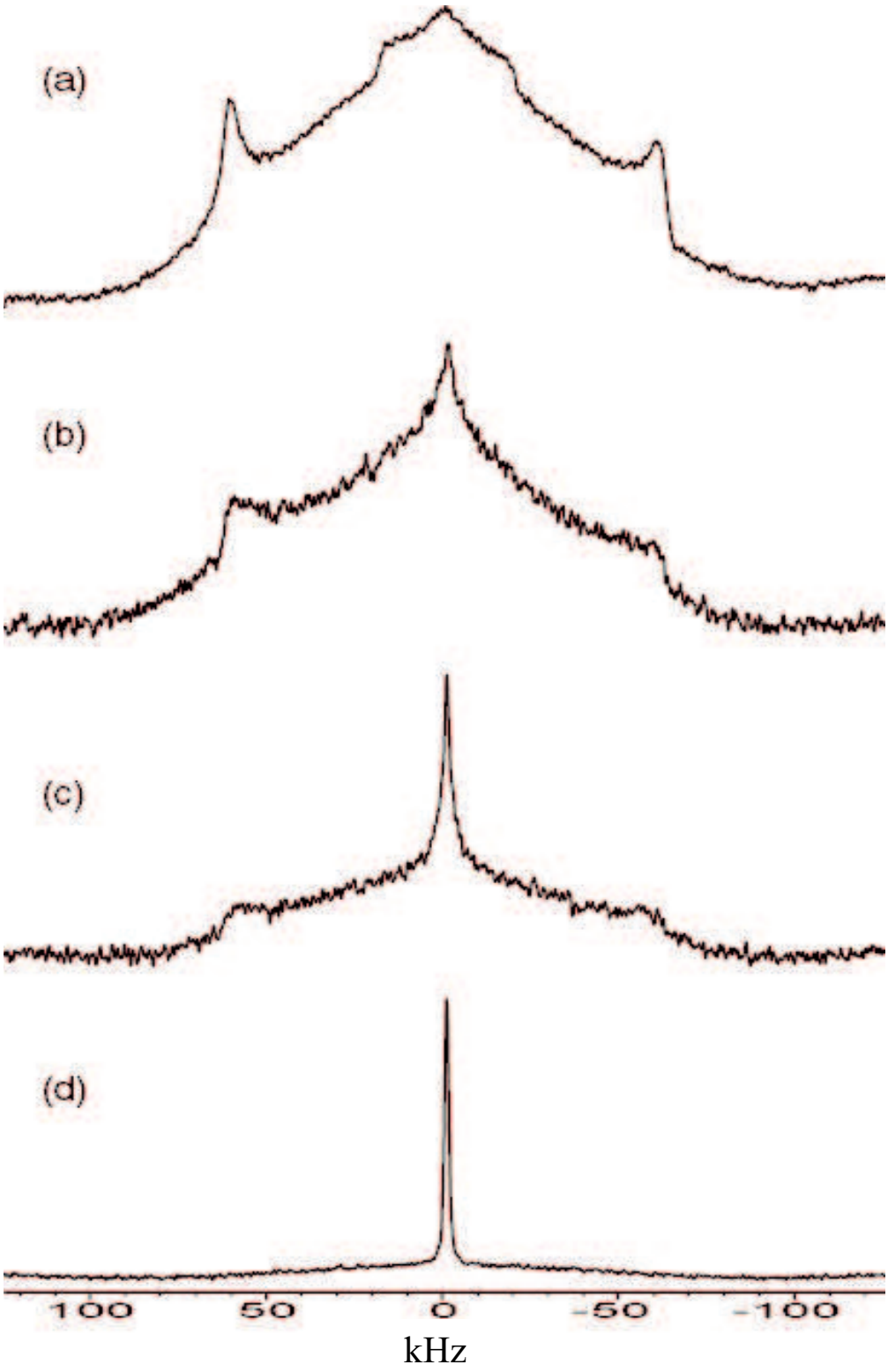

Figure 45: Solid-echo spectrum for the mixture at 25°C (a), 50°C (b), 80°C (c) and 100°C (d). The solid echo time was 100 μs, the τ_D 10 s, the acquisition time 4.096 ms, the spectral width 250 kHz and the number of scans was 2224. The pulse length of 1.55 μs was sufficiently short for obtaining solid-state ^2H spectra that were reduced in intensity by only about 5% at the outer edges.

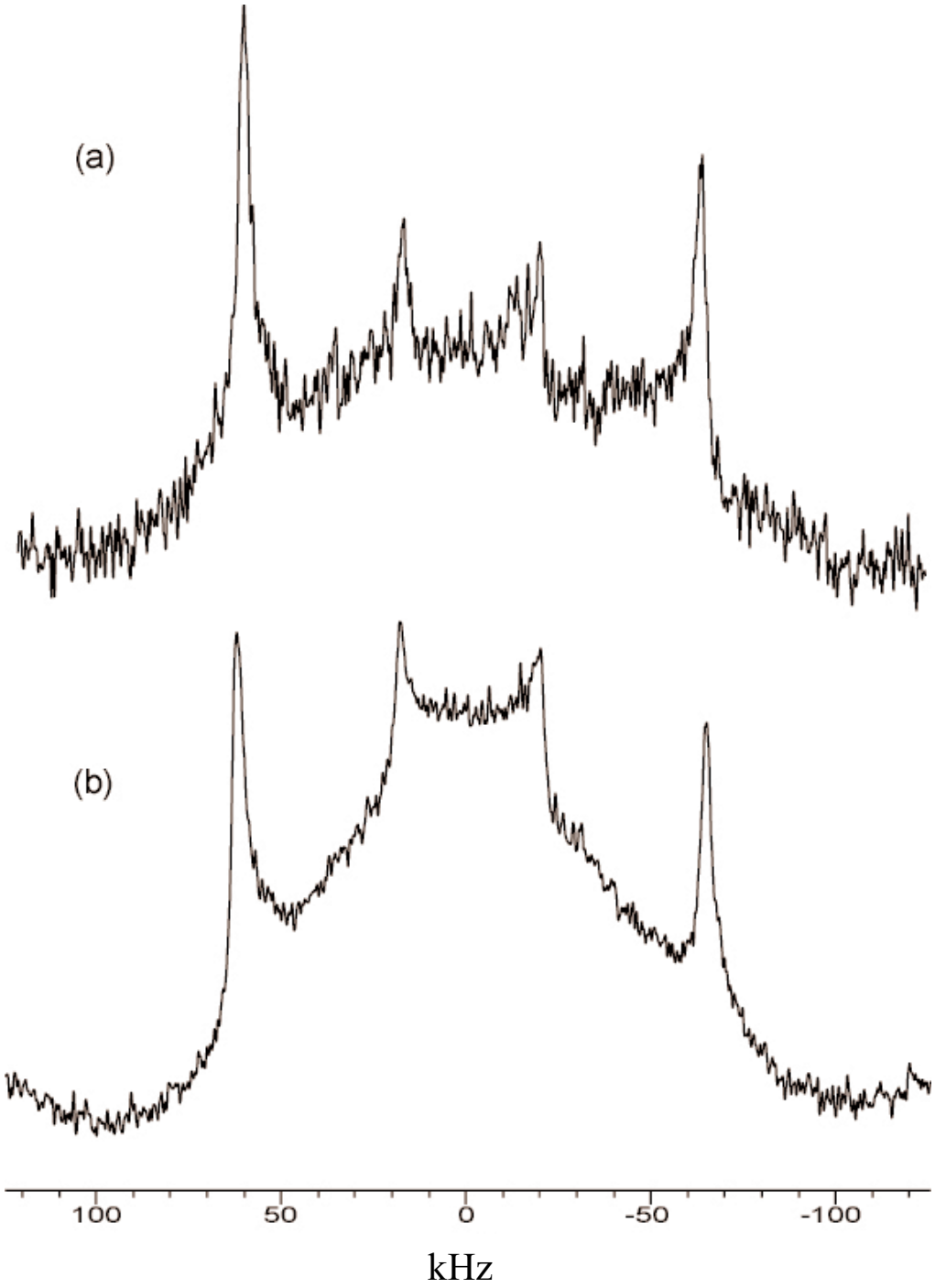

Figure 46: Solid-Echo spectrum at $-100^{o}C$ for the two samples $C_{216}H_{434}$-d_{24} (a) and the mixture (b). Note that the percentage of the fast motion in (b) is larger than in (a). All the acquisition parameters are the same as in Figure 45.

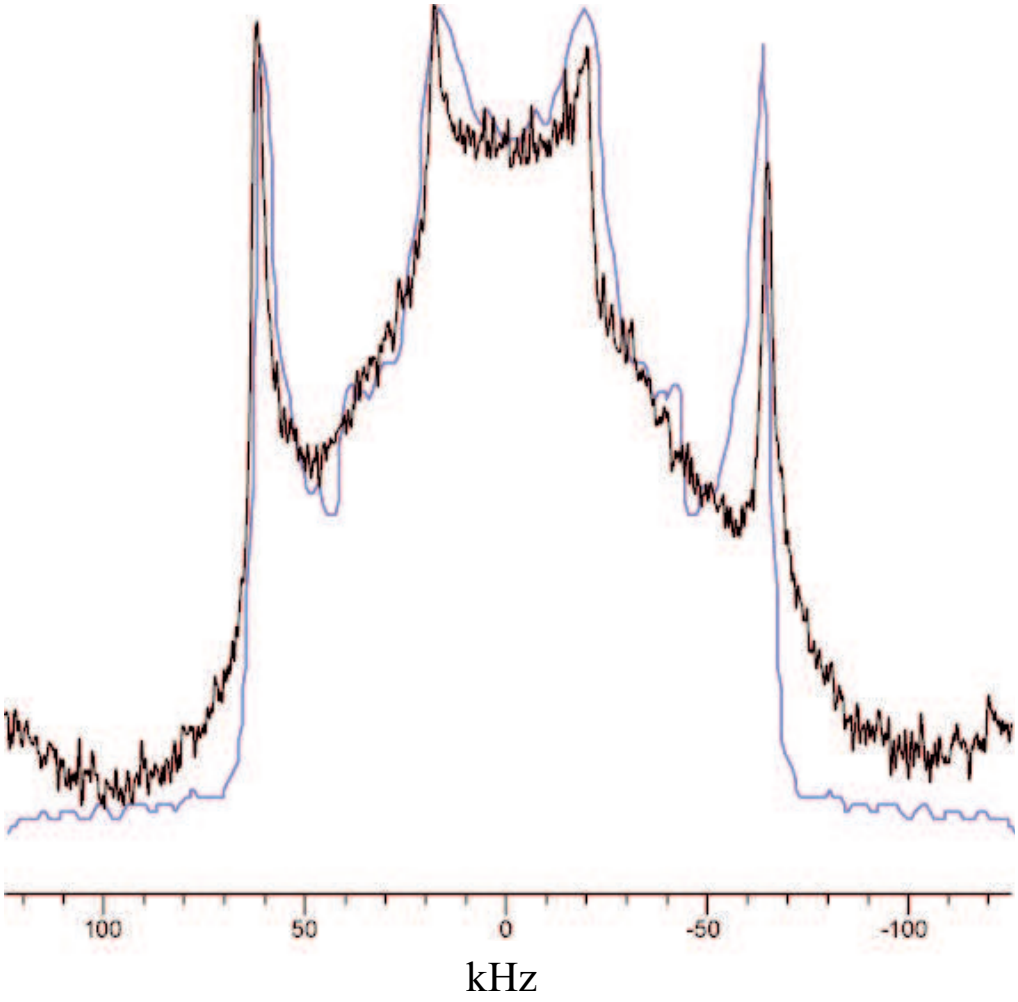

Figure 47: Simulation of the solid-echo spectrum for the mixture at –100°C (blue line). The simulation line was obtained by using a correlation time of 0.3 μs for the fast crankshaft 5-bond motion (30%) and 100 μs for the static motion (70%). Note that any longer correlation time for the static motion did not change the simulated line shape significantly.

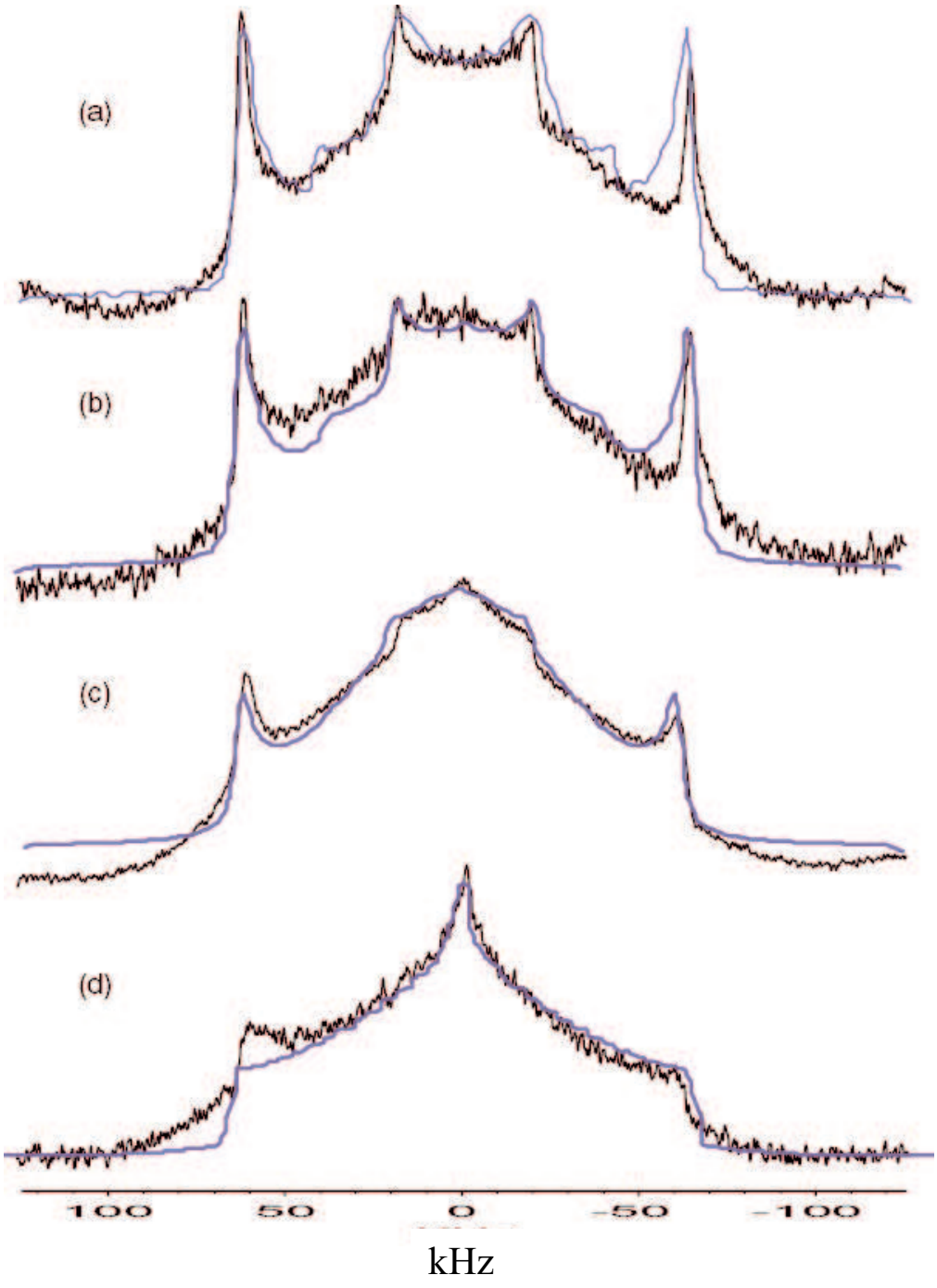

Figure 48: Solid-echo spectrum for the mixture at -100°C (a), -70°C (b), 20°C (c) and 50°C (d). The solid echo time was 100 μs, the τ_D 10 s, the acquisition time 4.096 ms, the spectral width 250 kHz and the number of scans was 2224. The pulse length of 1.55 μs was sufficiently short for obtaining solid-state ^2H spectra that were reduced in intensity by only about 5% at the outer edges.

3.4 Conclusions and future studies

The main aim of section 3 was to elucidate some intriguing issues such as structure, morphology and motion of polymeric materials and long chain *n*-alkanes. Some interesting experimental results, together with theoretical models, gave an insight on important scientific questions such as chain folding, motion and NMR relaxation mechanisms. This enabled us to correlate the properties of the samples studied to their structures and finally to the different preparation procedures. We managed to characterize, simply by NMR measurements, samples that have been prepared in different ways, highlighting and explaining similarities and/or differences with analogous studies found in the current literature.

From our NMR studies on UHWPE we found that the recovery of magnetization is partly due to chain diffusion and partly due to relaxation in a mobile interphase between amorphous and crystalline layers. The fact that this interphase shows up in the spectrum with the same shift as a crystalline peak means that motion such as the kink 3-bond and the crankshaft 5-bond are not responsible for the recovery of the magnetization in the interphase, as both types of motions imply the presence of some gauche carbon bonds that would shift the carbon signal to the "amorphous phase" region. For this reason we propose that the motion responsible for the recovery of the magnetization in the interphase involves the displacement of a large section of the chain. It seems reasonable to think that this portion of the chain (the interphase) is dragged by the mobile chain ends into some sort of motion that, although keeping all the carbon bonds in the trans conformation, it drives a relaxation mechanism with a measurable T_1.

At all temperatures investigated our proposed model was able to fit perfectly the experimental data in the whole range of relaxation times.

From the NMR investigation of long chain *n*-alkanes we have been able to draw some important and unambiguous conclusions. First of all, in the case of $C_{246}H_{494}$, our NMR data confirmed that it is possible to prepare reversibly from the same *n*-alkane both the once folded (OF) and the extended (E) form, depending on the rate of cooling the sample from the melt. Particularly, we have been able to calculate for OF the number of carbon nuclei involved in the fold, which varies depending on the rate of cooling the sample. If it is quenched from the melt, we found that it is possible to obtain samples with a consistently large amorphous part, having a fold that involves up to 25 carbon nuclei.

On the other hand, if the sample is cooled quickly but in a controlled manner (for details see section 3.2.1) a much more crystalline material is produced. Such a compound, labelled OF in the previous sections, was studied by solid-state NMR and the following conclusions could be drawn:

- The number of carbon nuclei involved in the fold is ≈ 7 at room temperature and ≈ 9 at 60°C and this findings strongly support the adjacent re-entry model for this kind of semi-crystalline materials, where the folds are regular and tight;
- The recovery of the magnetization, that is the relaxation process, is due, in this case as in UHMWPE, to two different factors: chain diffusion, that is mainly responsible for the recovery of the magnetization at longer times; a rapid relaxation process for the carbon nuclei that are in the "interphase", relaxing with a T_1 of about 6-7 s as

in UHMWPE (T_1 for the crystalline part was estimated to be >1500 s, the longest t_D value used in our experiments);

- The interphase is about 10% of the crystalline part as in UHMWPE;
- Chain diffusion is increased with temperature and has exactly the same rate as in UHMWPE that is ≅100 jumps/s at 60°C and ≅10 jumps/s at 20°C;
- The values of the diffusion rate at different temperatures found in our simulations allowed us to estimate the activation energy for the diffusion process, E_a = 105 ± 10 kJ/mol. This result is consistent with the value of 104-116 kJ/mol for the ***a*** process found in the literature for PE.

Furthermore, new insights on the nature of the fold for both PE and OF were given so that it was possible to distinguish between a tight and loose fold by NMR technique only.

Analogously, we have been able to characterize another form of $C_{246}H_{494}$, the so-called E form, where the chain are not folded anymore due to the fact that the sample is prepared by very slow cooling rate (see section 3.2.1 for details). Again our NMR data allowed us to draw some important conclusions:

- In E the amorphous part is very small (the methyl, the last methylene bonded to the methyl and 1-2 more carbon nuclei).
- For E the recovery of relaxation is much slower than for OF, due to the fact that the chain diffusion is much more limited for E as only the displacement of very few carbons is allowed in this case.

Furthermore, both in OF and E, the amorphous part relaxes very quickly (T_{1a} ≅ 1-2 s) and this means that although there is not a large amorphous layer, there

is still a large free volume in the vicinity of the chain ends where wide movements are allowed.

It seemed quite clear at this stage that the structure of the *n*-alkanes is an alternation of crystalline and amorphous (i.e. more mobile) lamellae as it was proposed by X. Zeng and G. Ungar[91]. We also found that between the amorphous and the crystalline part there is an "interphase", that shows up as a crystalline peak in the ^{13}C NMR spectrum, but it can also relax with a rapid T_1 process, having a T_1 of the order of 6-7 s.

Nevertheless, the partially deuterated sample ($C_{216}H_{434}$-d_{24}) helped us to refine this model, confirming some of our previous findings, but also adding new information to this picture. Our ^2H NMR studies showed that it is possible to obtain partially deuterated samples such as $C_{216}H_{434}$-d_{24} (a) and from the analysis of the data it was possible to confirm that in the E form of this *n*-alkanes only the chain ends (methyl, last methylene bonded to the methyl and about 1-2 more carbon nucleus each end) are in the amorphous part, confirming the previous result obtained on a slightly different sample with an independent method (216 instead of 246 carbon units in this case). We fitted all the experimental line shape for sample (a) at different temperatures, giving an insight on the motion of such a long *n*-alkane. Being only the chain ends deuterated we have been able to observe the motion of part of the molecules normally neglected in the NMR studies of polymers, such as the methyl and the last methylene groups of the chain. We found out that the ends of the chains move much faster than the bulk and that their vicinity can shorten the relaxation time for nearby parts of the chain by several orders of magnitude.

The deuterium NMR results for the mixture of *n*-alkanes of different lengths have been compared with the data previously obtained for the partially deuterated sample (a). The results can be explained by assuming that the mixture has a super-lattice structure as proposed by Ungar and Zeng. Nevertheless our data seem to show that the middle layer is not perfectly crystalline even at low temperatures, contradicting the fact that all the layers are crystalline in the super-lattice structure. Furthermore, our NMR investigations show the transition between the two different phases (low temperature and high temperature), but this does not appear as sharp as Ungar and Zeng have stated. We think that because of the polymeric structure of these long *n*-alkanes it is not possible to have a very precise value of temperature for the phase transition, but this is likely to happen in a window of values between 90^{o}C and 100^{o}C. Nevertheless we do not exclude that this is an intrinsic limit of the NMR technique.

Finally, it is worth noting that in order to have a complete understanding of how it is possible to alter the crystallinity and therefore the properties of long-chain *n*-alkanes and polyethylene, an accurate study of the correlation between the crystallinity of the sample and the chain length is desirable. For this reason, the investigation of other different deuterated samples and mixtures is highly recommended for future studies of these materials.

Acknowledgements

I would like to thank all the people who helped me during the course of my research in Nottingham, and in particular:

My supervisor **Dr. Jeremy J. Titman** who led and encouraged me throughout the whole period of my PhD. He represents a scientific guide to me, having taught me not only a portion of his NMR knowledge but, most important, a general valid approach towards the scientific research that is applicable in every field of science.

Dr. John Godward for his helpful support during his short permanence in Nottingham, his advices about computer and programming issues were always precious to me.

All my friends from the rowing club, particularly **Dr. Mark Gillott** who I spent so much good time with and **Colin Troy** who was always very helpful and supportive even when my English was poor during my first year in England!

Last but not least I thank my family and my girlfriend **Annalisa** who provided me lots of love to help me survive rainy England.

References

[1] J. W. Hennel and J. Klinowski, (1993) *"Fundamentals of Nuclear Magnetic Resonance"*, Harlow: Longman Scientific and Technical Press.

[2] A. Carrington and A. D. McLachlan, (1979) *"Introduction to Magnetic Resonance"*, London: Chapman and Hall Press.

[3] A. E. Derome, (1987) "*Modern NMR Techniques for Chemistry Research"*, Oxford: Pergamon Press.

[4] M. Goldman, (1988) "*Quantum Description of High-Resolution NMR in Liquids*", Oxford: Clarendon Press.

[5] R. R. Ernst, G. Bodenhausen and A. Wokaun, (1987) "*Principles of Nuclear Magnetic Resonance in One and Two Dimensions*", Oxford: Clarendon Press.

[6] E. O. Stejskal and J. D. Memory, (1994) "*High Resolution NMR in the Solid State*", New York: Oxford University Press.

[7] J. Korringa, (1950) *Physica, 16*, 601.

[8] M. Mehring, (1983) *"Principles of High Resolution NMR in Solids"*, Berlin: Springer-Verlag Berlin Heidelberg New York Press.

[9] R. K Harris, (1986) *"Nuclear Magnetic Resonance Spectroscopy"*, Harlow: Longman Scientific and Technical Press.

[10] O. N. Antzutkin, Z. Song, X. Feng, and M. H. Levitt, (1994) *J. Chem. Phys., 100*, 130-140.

[11] O. N. Antzutkin, S. C. Shekar, and M. H. Levitt, (1995) *J. Magn. Reson. Series A*, *115*, 7-19.

[12] S. F. De Lacroix, J. J. Titman, A. Hagemeyer, and H. W. Spiess, (1992) *J. Magn. Reson., 97*, 435-443.

[13] W. T. Dixon, (1982) *J. Chem. Phys., 77*, 1800-1809.

[14] J. Herzfeld and A. E. Berger, (1980) *J. Chem. Phys*. *73*, 6021-6030.

[15] C. P. Slichter, (1978) "*Principles of Magnetic Resonance*", 2nd edn., Berlin: Springer-Verlag Berlin Heidelberg New York Press.

[16] A. Abragam, (1961) "*The Principles of Nuclear Magnetism*", Oxford: Clarendon Press.

[17] U. Haeberlen, (1976) "*High Resolution NMR in Solids Selective Averaging*", New York: Academic Press.

[18] M. Edén and M. H. Levitt, (1998) *J. Magn. Reson.*, *132*, 220-239.

[19] H. W. Spiess, (1983) *Colloid & Polymer Sci.*, *261*, 193-209.

[20] R. J. Abraham, J. Fisher and P. Loftus, (1988) *"Introduction to NMR Spectroscopy"*, Chichester: Wiley.

[21] M. H. Levitt, (2001) "*Spin Dynamics*", Chichester: Wiley.

[22] J. Keeler and D. Neuhaus, (1985) *J. Magn. Reson., 63*, 454-472.

[23] A. G. Redfield and S. D. Kunz, (1975) *J. Magn. Reson. 19*, 250.

[24] A. R. Kortan, N. Kopylov, S. H. Glarum, E. M. Gyorgy, A. P. Ramirez, R. M. Fleming, F. A. Thiel and R. C. Haddon, (1992) *Nature*, *355*, 529.

[25] P. A. Winsor, (1974) "*Liquid Crystals and Plastic Crystals" vol 1*, New York: Wiley, p 48.

[26] P. W. Stephens, L. Mihály, P. A. Lee, R. L. Whetten, S. M. Huang, R. Kaner, F. Diederich and K. Holczer, (1991) *Nature*, *351*, 632.

[27] P. Auban-Senzier, D. Jérome, F. Rachdi, G. Baumgartner, and L. Forró, (1996) *J. Phys. I France*, *6*, 2181-2190.

[28] J. Winter and H. Kuzmany, (1992) *Solid State Commun.*, *84*, 935.

[29] A. Jánossy, O. Chauvet, S. Pekker, J. R. Cooper and L. Forró, (1993) *Phys. Rev. Lett.*, *71*, 1091.

[30] S. Chakravarty, M. P. Gelfand, and S. Kivelson, (1992) *Science*, *254*, 970.

[31] Q. Zhu, O. Zhou, J. E. Fischer, A. R. McGhie, W. J. Romanov, R. M. Strongin, M. A. Cichy and A. B. Smith III, (1993) *Phys. Rev. Lett.*, *47*, 13948.

[32] P. W. Stephens, M. Laszlo, J. B Wiley, H. S. Mei, R. B. Kaner, F. Diederich., , R. L Whetten and K. Holczer, (1992) *Phys. Rev. B, 45*, 543.

[33] R. Tycko, G. Dabbagh, D. W. Murphy, Q. Zhu and J. E. Fischer, (1993) *Phys. Rev. B*, *48*, 9097.

[34] D. M. Poirier and J. H. Weaver, (1993) *Phys. Rev. B, 47*, 10959-62.

[35] O. Chauvet, G. Oszlànyi, L Forró, P. W. Stephens, M. Tegze, G. Faigel and A. Jánossy, (1994) *Phys. Rev. Lett.*, *72*, 2721.

[36] S. Pekker, L. Forró, L. Mihály and A. Jánossy, (1994) *Solid State Commun.*, *90*, 349.

[37] P. W. Stephens, G. Bortel, G. Faigel, M. Tegze, A. Jánossy, S. Pekker, G. Oszlànyi and L. Forró, (1994) *Nature, 370*, 636.

[38] J. R. Fox, G. P. Lopinski, J. S. Lannin, G. B. Adams, J. B. Page and J. E. Fischer, (1996) *Chem. Phys. Lett.*, *249*, 195-200.

[39] D. Bormann, J. L. Sauvajol, C. Goze, F. Rachdi, A. Moreac, A. Girard, L. Forro and O. Chauvet, (1996) *Phys. Rev. B*, *54* (19), 14139-14145.

[40] H. Schober, A. Toelle, B. Renker, R. Heid and F. Gompf, (1997) *Phys. Rev. B*, *56*, 5937-5950.

[41] C. H. Choi and M. Kertesz, (1998) *Chem. Phys. Lett.*, *282*, 318.

[42] S. Pekker, G. Oszlanyi and G. Faigel, (1998) *Chem. Phys. Lett.*, *282*, 435.

[43] F. Bommeli, L. Degiorgi, P. Wachter, Ö. Legaze, A. Jánossy, G. Oszlànyi, O. Chauvet and L. Forró, (1995) *Phys. Rev. B*, *51*, 14794.

[44] R. Tycko, G. Dabbagh, M. J. Rosseinsky, D. W. Murphy, A. P. Ramirez and R. M. Fleming, (1992) *Phys. Rev. Lett*., *68*, 1912-15.

[45] K.-F. Their, G,. Zimmer, M. Mehring and F. Rachdi, (1996) *Phys. Rev. B*, *53*, R496.

[46] H. Alloul, V. Brouet, E. Lafontaine, L. Malier and L. Forrò, (1996) *Phys. Rev. Lett.*, *76*, 2922.

[47] S. C. Erwin, G. V. Krishna and E. J. Mele, (1995) *Phys. Rev. B*, *51*, 7345.

[48] T. M. de Swiet, J. L. Yarger, T. Wagberg, J. Hone, B. J. Gross, M. Tomaselli, J. J. Titman, A. Zettl and M. Mehring, (2000) *Phys. Rev. Lett.*, *84*, 717.

[49] See, e. g., H. Geen, J. Gottwald, R. Graf, I. Schnell, H. W. Spiess and J. J. Titman, (1997) *J. Magn. Reson., 125*, 224-227.

[50] M. Hohwy, H. J. Jakobsen, M. Eden, M. H. Levitt and N. C. Nielsen, (1998) *J. Chem. Phys.*, *108*, 2686-2694.

[51] A. S. D. Heindrichs, H. Geen and J. J. Titman, (2000) *J. Magn. Reson.*, *147*, 68.

[52] K. Tanaka, T. Saito, Y. Oshima, T. Yamabe and H. Kobayashi, (1997) *Chem. Phys. Lett.*, *272*, 189.

[53] A. Lesage, C. Auger, S. Caldarelli and L. Emsley, (1997) *J. Am. Chem. Soc.*, *119*, 7867-7868.

[54] A. Bax , R. Freeman and T. A. Frenkiel, (1981) *J. Am. Chem. Soc., 103*, 2102-2104.

[55] A. Lesage, M. Bardet and L. Emsley, (1999) *J. Am. Chem. Soc.*, *121*, 10987.

[56] A. Bax, R. Freeman and T. A. Frenkiel, (1981) *J. Am. Chem. Soc.*, *103*, 2102.

[57] E. H. Hardy, R. Verel and B. H. Meier, (2001) *J. Magn. Reson.*, *148*, 459.

[58] A. S. D. Heindrichs, H. Geen and J. J. Titman, (2001) *Chem. Phys. Lett.*, *335*, 89-96.

[59] V. J. McBrierty and K. J. Packer, (1993) "*Nuclear Magnetic Resonance in Solid Polymers*", Cambridge: Cambridge University Press.

[60] M. J. Duer, (2001) *Annual Reports on NMR Spectroscopy*, *43*, 1-58.

[61] D. Hentschel, H. Sillescu and H. W. Spiess, (1984) *Polymer*, *25*, 1078-1086.

[62] G. Ungar, J. Stejny, A. Keller, I. Bidd and M. C. Whiting, (1985) *Science, 229*, 386.

[63] G. Ungar and X. B. Zeng, (2001) *Chem. Rev.*, *101*, 4157-4188.

[64] R. G. Snyder, M. Maroncelli, S. Ping Qi and H. L. Strauss, (1981) *Science*, *214*, 188-190.

[65] M. Moller, H. Cantow, H. Drotloff, D. Emeis, K. Lee and G. Wegner, (1986) *Makromol. Chem., 187*, 1237-1252.

[66] M. A. N. Driver and P. G. Klein, (1999) *Macromol. Symp., 141*, 263-281.

[67] A. Jonas, R. Legras, R. Scherrenberg and H. Reynaers, (1993) *Macromolecules*, *26*, 526.

[68] D. R. Rueda, M. G. Zolutukhin, G. Nequlqueo, C. Garcia, J. G. De La Campa and J. De Abajo, (2000) *Macromol. Chem. Phys.*, *201*, 427.

[69] L. H. Sperling, (1992) "*Introduction to Physical Polymer Science*", New York: Wiley.

[70] R. Hentschel, H. Sillescu and H. W. Spiess, (1979) *Makromol. Chem., 180*, 241-249.

[71] R. Hentschel, H. Sillescu and H. W. Spiess, (1981) *Polymer*, *22*, 1516-1521.

[72] F. C. Schilling, F. A. Bovey, S. Tseng, and A. E. Woodward, (1983) *Macromolecules*, *16*, 808.

[73] I. M. Ward and D. W. Hadley, (1993) *"An Introduction to the Mechanical Properties of Solid Polymers"*, 2nd ed., London: John Wiley and Sons.

[74] M. Takayanagi, (1963) *Mem. Fac. Eng., Kyushu Univ.*, *23*, 1-17.

[75] P. G. de Gennes, (1979) "*Scaling Concepts in Polymer Physics"*, London: Cornell University Press.

[76] D. L. VanderHart, (1979) *Macromolecules*, *12*, 1232-1235.

[77] B. Scröter and A. Posern, (1981) *A. Makromol. Chem*, *182*, 675-680.

[78] B. Scröter and A. Posern, (1982) *A. Makromol. Chem*, *Rapid Commun*., *3*, 623-628.

[79] A. Kaji, A. Yamanaka and M. Murano, (1990) *Polym. J.*, *22*, 893-900.

[80] D. E. Axelson, (1982) *J. Polym. Sci., Polym. Phys.*, *20*, 1427-1435.

[81] K. Schimidt-Rohr and H. W. Spiess, (1991) *Macromolecules*, *24*, 5288-5293.

[82] M. B. Robertson, I. M. Ward, P. G. Klein and K. J. Packer, (1997) *Macromolecules*, *30*, 6893-6898.

[83] D. L. VanderHart, (1987) *J. Magn. Reson*., *72*, 13.

[84] H. Fröhlich, (1942) *Proc. Phys. Soc*., *54*, 442.

[85] D. E. Axelson, (1981) *J. Polym. Sci., Polym. Phys*., *20*, 1477.

[86] J. D. Hoffmann, G. Williams and E. Passaglia, (1966) *J. Polm. Sci.*, *C14*, 173.

[87] J. L. Syi and M. L. Mansfield, (1988) *Polymer*, *29*, 987.

[88] D. Schaefer, H. W. Spiess, U. W. Suter and W. W. Fleming, (1990) *Macromolecules*, *23*, 3431.

[89] C. G. Vonk and G. Kortleve, (1967) *Kolloid Z. Z. Polym*., *220*, 19.

[90] W. Ruland, (1977) *Colloid Polym. Sci*., *255*, 417.

[91] X. Zeng and G. Ungar, (2002) *Polymer*, *43*, 1657-1666.

[92] G. M. Brooke, S. Burnett, S. Mohammed, D. Proctor and M. C. Whiting, (1996) *J. Chem. Soc*., *Perkin Trans 1*, 1635.

[93] A. Keller, S. J. Organ and G. Ungar, (1991) *Makromol. Chem., Macromol. Symp., 48/49*, 93-102.

[94] G. Ungar and A. Keller, (1986) *Polymer*, *27*, 1835-1844.

[95] G. Ungar and A. Keller, (1987) *Polymer*, *28*, 1899.

[96] S. J. Organ, G. Ungar and A. Keller, (1989) *Macromolecules*, *22*, 1995.

[97] X. B. Zeng, G. Ungar, S. J. Spells, G. M. Brooke, C. Farren and A. Harden, (2003) *Phys. Rev. Lett.*, *90*, 155508/1-155508/4.

[98] W. Pechhold, S. Blasenbrey and S. Woerner, (1963) *Kolloid Z. u. Z. Polym*., *189*, 14.

[99] L. Monnerie and F. Gény, (1969) *J. Chim. Phys. Physiochim. Biol*., *66*, 1691.

[100] T. F. Schatzki, (1965) *Polym. Prepr. Am. Chem. Soc., Div. Polym. Chem*., *6*, 646.

[101] N. J. Heaton, (1997) *Molecular Physics*, *92*, 251-263.

[102] N. G. Van Kampen, (1981) "*Stochastic Processes in Physics and Chemistry"*, Amsterdam: Elsevier.

[103] K. Müller, P. Meier and G. Kothe, (1985) *Progr. NMR Spectrosc*., *17*, 211.

[104] J. R. Norris, and S. I. Weissman, (1969) *J. Phys. Chem*., *73*, 3119.

[105] R. Hentschel and H. W. Spiess, (1979) *J. Magn. Reson*., *35*, 157.

[106] J. G. Powles and J. H. Strange, (1963) *Proc. Phys. Soc*. *82*, 6.

[107] J. H. Davis, K. R. Jeffrey, M. Bloom, M. I. Valic and T. P. Higgs, (1976) *Chem. Phys. Letters, 42*, 390.

[108] R. Blinc, V. Rutar, J. Seliger, J. Slak and V. Smolej, (1977) *Chem. Phys. Letters, 48*, 576.

[109] H. W. Spiess and H. Sillescu, (1981) *J. Magn. Resonance*, *42*, 381-389.

[110] N. Boden, S. M. Hanlon, Y. K. Levine and K. Mortimer, (1978) *Mol. Phys*., *36*, 519.

[111] M. Moller, (1985) *Adv. Polym. Sci*., *66*, 59.

[112] J. Cheng, M. Fone, V. N. Reddy, K. B. Schwartz, H. P. Fischer and B. Wunderlich, (1994) *J. Polym. Sci., Polym. Phys*., *32*, 2683-2693.

[113] R. Kitamaru, F. Horii and K. Murayama, (1986) *Macromolecules*, *19*, 636-643.

[114] K. Bergmann and K. Nawotky, (1967) *Koloid-Z Z Polym*, *219*, 132.

[115] K. Bergmann, (1973) *Koloid-Z Z Polym*, *251*, 962.

[116] R. Kitamaru, F. Horii and S. Hyon, (1977) *J. Polym. Sci. Polym. Phys. Ed., 15*, 821.

[117] R. Kitamaru and F. Horii, (1978) *Adv. Polym. Sci*., *26*, 137.

[118] R. Kitamaru, T. Nakaoki, RG Alamo and L. Mandelkern, (1996) *Macromolecules*, *29*, 6847.

[119] J. Cheng, M. Fone, V. N. Reddy, K. B. Schwartz, H. P. Fisher and B. Wunderlich, (1994) *J. Polym. Science: PartB: Polymer Physics*, *32*, 2683-2693.

[120] C. Shen, A, J. Peacock, R. G. Alamo, T. J. Vickers, L. Mandelkern and C. K. Mann, (1992) *Applied Spectroscopy*, *46*, 8.

[121] R. Mutter, W. Stille and G. Strobl, (1993) *J. Polym. Science: Part B: Polymer Physics*, *31*, 99-105.

[122] N. Stribeck, R. G. Alamo, L. Mandelkern and H. G. Zachmann, (1995) *Macromolecules*, *28*, 5029-5036.

[123] N. G. McCrum, B. E. Read and G. Williams, (1967) "*Anelastic and Dielectric Effects in Polymeric Solids"*, Wiley: New York.

[124] P.G. Klein and M. A. N. Driver, (2002) *Macromolecules*, *35*, 6598-6612.

[125] R. J. Young and P. A. Lovell, (2000) "*Introduction to Polymers*", 2nd ed., Cheltenham : Stanley Thornes, section 4.1.5 p 258.

[126] R. Born and H. W. Spiess, (1995) *Macromolecules*, *28*, 7785-7795.

[127] S. P. Chum, G. W. Knight, J. M. Ruiz, and P. J. Phillips, (1994) *Macromolecules*, *27*, 656-659.